

THE ROLE OF CRUSTAL FLUIDS IN TECTONICS OF NORTH-CENTRAL
TURKEY INFERRED FROM THREE-DIMENSIONAL MAGNETOTELLURICS

by

Sinan Özaydın

B.S., Geophysical Engineering, İstanbul Technical University, 2015

Submitted to the Kandilli Observatory and Earthquake
Research Institute in partial fulfillment of
the requirements for the degree of
Master of Science

Graduate Program in Geophysics
Boğaziçi University

2017

ACKNOWLEDGEMENTS

Firstly, I would like to thank my thesis supervisor Assoc. Prof. Dr. S. Bülent Tank. His door was always open for me during my master's education. His supportive and fruitful comments on my work and career remarkably affected my skills on many subjects and my approach on scientific methodology.

I would like to thank my friends at the institution for their friendly support and joyful environment that they have been providing. In particular, I would like to thank Mustafa Karas for his invaluable support on my work and thesis.

Without my mother, Filiz Sınıksaran's and my uncle Enis Sınıksaran's emotional and financial support on my career, I would not even be able to apply to a master's program. For this reason, I would like to thank them wholeheartedly.

I would like to thank Prof. Dr. Gary Egbert for providing 3-D magnetotelluric inversion code, ModEM. This research was funded by National Science Foundation (of the USA). I also would like to thank Prof. Dr. Semih Ergintav for providing relocated earthquakes of ISC catalogue. Preliminary results of this thesis were presented in the EGU 2017 General Assembly in Vienna.

The data used in this study were previously subject to another M.Sc. thesis of Bekin (2016), which was based on developing a phase tensor visualizing algorithm. The main goal of that thesis was to test the algorithm and justify its results with synthetic data. In order to see whether the algorithm was performing accurately, the phase tensor ellipses were plotted for the data of the current study with limited details where comprehensive tectonic interpretations were not involved. The figures and the interpretations used in the current study on phase tensors were reproduced and extended independently for the same data-set. Additionally, this thesis mostly focuses on three-dimensional modeling of the magnetotelluric (MT) data and relative geological and tectonic interpretations. The phase tensor analyses, which is an essential prior step

to MT modeling, reproduced with different algorithms. Accordingly, throughout the phase tensor part of this current study, Bekin (2016) was respectfully acknowledged.

ABSTRACT

THE ROLE OF CRUSTAL FLUIDS IN TECTONICS OF NORTH-CENTRAL TURKEY INFERRED FROM THREE-DIMENSIONAL MAGNETOTELLURICS

Central Pontides have been an active margin to Laurasia since the Paleozoic times. They consists of geological footprints of several episodes of subduction-accretion events and collisional tectonics. For these reasons, they have been a great laboratory for examining the evolution of Anatolia and the Tethyan oceans for decades. Many geological studies have been made with different methodologies, however there is still a lack of geophysical results in the region. In search of this potential, 26 wide-band (320 - 0.00055 Hz) magnetotelluric measurements were deployed to depict the geo-electric properties in a crustal range. The data were collected to form a 190-km-long profile, passing through Çankırı Basin, İzmir-Ankara-Erzincan Suture Zone (İAES), Tosya Basin, North Anatolian Fault Zone, Central Pontides Super-complex, Küre Complex and the Pontide Arc. Phase tensor analyses and 3-D inversions were applied to this data to develop a model that accurately display the geo-electrical characteristics of the region.

Phase tensor analyses point out that the regional geo-electric strike angles fit within the $N80^{\circ}E - N90^{\circ}E$ range with the exception of $N75^{\circ}E$ for the data near Çankırı Basin and Kızılırmak Fault. Lack of oblique conductors in the data reduces the dimensional complexity and helps the 3-D inversion schemes to be more accurate for a profile based measurement. Two distinct 3-D models were developed: (1) A model that covers whole frequency range and stations, (2) another model that aims to picture the area in the vicinity of North Anatolian Fault (NAF). For the second model, data from only ten stations (stations from 9 to 19) were used down to a frequency of 0.035 Hz.

The final models attained from the 3-D inversions were compatible with the rheological environment around the NAF that lacks moderate seismicity and ensures a deeper brittle to ductile transition by two resistive features appearing on both sides of the fault. This characteristic is present at the southern side of the fault via obducted ophiolites and intra-oceanic arc units, while the other side is made up of metamorphic rocks of Central Pontide Supercomplex. Both of the bodies are geological units, which are devoid of effective porosity that can enhance mechanical strength along the fault and inhibit fluid flow towards the fault zone. The NAF model demonstrate that the Tosya Basin appears as a conductive syncline where its basement is placed between 3.6 and 4.3 km. Fault zone conductors were found within this model matches well with the spatial positions of the NAF and related subsidiary faults.

South of the suture zone, a buried thrust belt is visible with several norward-dipping conductive-resistive interfaces. Çankırı Basin appears as a conductive zone with several resistive interruptions. Projected earthquakes correlate well with the resistivity variations indicating fault-like structures.

Beneath the northernmost features in the model, the resistive characteristics appear in deeper structure confirming the crustal thickening in the region. North of the fault, CPS shows itself as a downward convex shaped resistive body that demonstrates heterogeneous conductive features near the surface. Çangaldağ Complex, placed at the tip of the CPS, exhibits highly resistive values beneath the Kastamonu Basin. A large conductive anomaly, which appears to have an upwelling feature was found beneath this region. Although the source of this fluid-rich zone is not resolved or clear, existence of this conductive region might have important implications on the seismic nature, rheological attributes and geological evolution of the area.

ÖZET

KITASAL SIVILARIN ORTA-KUZEY TÜRKİYE’NİN TEKTONİĞİ ÜZERİNE ETKİSİNİN ÜÇ-BOYUTLU MANYETOTELLÜRİK YÖNTEM İLE ARAŞTIRILMASI

Orta Pontidler, Paleozoyik zamanlardan beri Lavrasya’nın aktif kıta kenarı olarak konumlanmıştır. Bölge, pek çok dalma-batma-eklenme ve çarpışma tektoniği olaylarının ayak izlerini bünyesinde barındırmakta ve bu sebepten ötürü Anadolu Plakası’nın ve Tetis Okyasunlarının evrimini araştırmak adına uzun yıllardır iyi bir laboratuvar görevi görmektedir. Çeşitli metodolojiler ile yapılmış pek çok jeolojik yaklaşıma karşın, bölgeye odaklanan jeofizik çalışmalar yetersizdir. Bölgedeki mevcut potansiyeli açığa çıkarmak ve yer-kabuğunun elektrik yapısını ortaya koymak adına, araştırma alanında 26 geniş-bant manyetotellürik ölçüm gerçekleştirilmiştir. Ölçümler; Çankırı Havzası, İzmir-Ankara-Erzincan Sütur Zonu, Tosya Havzası, Kuzey Anadolu Fay Hattı, Orta Pontidler Süperkompleksi (OPS), Küre Kompleksi ve Pontid Magmatik Yayı’nı kesecek şekilde, yaklaşık olarak 190 km uzunluğunda bir profil doğrultusunda alınmıştır. Faz tensörü analizleri ve 3-B ters çözüm teknikleri, bölgenin gerçek yer-elektrik yapısını yansıtmak amacıyla veriye uygulanmıştır.

Faz tensör analizleri bölgedeki rejyonel yer-elektrik yönelimlerinin çoğunluğunun $K80^{\circ}D - K90^{\circ}D$ arasında seyrettiğini göstermektedir. Bu konudaki tek istisna Çankırı Havzası ve Kızılırmak Fayı’nın etkin olduğu verilerde $K75^{\circ}D$ olarak gözlemlenmiştir. Verideki oblik iletkenliklerin azlığı, boyutluluk karmaşasını azaltmakta ve profil bazında yapılan 3-B rejyonel modellemelerin doğruluk oranının artırmaktadır. İki ayrı 3-B model bölgeyi araştırma amacıyla tasarlanmıştır: (1) Tüm istasyonlardaki verilerin ve frekans aralığının kapsandığı bir model ile (2) sadece Kuzey Anadolu Fayı (KAF) etrafındaki 9 ve 19. istasyonlar arasında, 0.035 Hz frekans değerine kadar olan verilerinin kullanıldığı ikinci bir model oluşturulmuştur.

3-B ters çözümlerinin ardından elde edilen modellerde KAF'ın etrafında gözlemlenen iki yüksek özdirençli yapı, bölgedeki deprem seyrekliğini ve daha derin gözlemlenen kırılğan-sünek ortam geçişini destekleyen reolojik birimlere işaret etmektedir. Fay'ın güneyindeki bu niteliklerin oluşması, ofiyolitik birimlerin yerleşmesi ve okyanus içi magmatik yay ile çarpışmasıyla sağlanıldığı düşünülmektedir. Fay'ın kuzeyinde bulunan yüksek özdirençli metamorfik kayalarla birlikte, fayın etrafındaki iki jeolojik ortam da mekanik zayıflığa sebep olacak efektif poroziteden yoksun durumda olduğu saptanmıştır. Tasarlanan KAF modelinde, Tosya Havzası'nın iletken elemanlar tarafından oluşmuş bir senklinal niteliğinde olduğu saptanmış ve havzanın temelini 3.6 ve 4.3 km arasındaki bir değerde olabileceği belirlenmiştir. Bölgede saptanmış fay zonu iletkenleri, KAF ve etrafındaki ikincil faylanmalar ile özdeşleştirilebildiği gözlemlenmiştir.

Kenet zonunun güneyinde, gömülü halde bulunan bir kuzeye dalan ters-faylanma mekanizması iletken-özdirençli sınırlarıyla belirgin bir şekilde saptanmıştır. Çankırı Havzası, özdirençli materyal girişimlerin de yer yer görüldüğü iletken özelliklere sahip bir yapı olarak resmedilmiştir. Söz konusu özdirençli girişimlerin oluşturduğu özdirenç varyasyonları deprem izdüşümleriyle iyi özdeşleşmekte oluşu fay tipi yapıların göstergesi olduğu düşünülmektedir.

Modelin en kuzey ucundaki birimlerin altı, oldukça derin bölgelerde yalıtkan olarak gözlemlenmesi, bölgedeki kabuk kalınlaşmasına işaret etmektedir. KAF'ın kuzey ucunda bulunan OPS, yüzeye yakın derinliklerde heterojen iletken özellikler gösteren geniş bir yüksek özdirençli yapı olarak resmedilmektedir. OPS'nin ucunda konuşlanmış olan Çangaldağ Karmaşığı (ÇGK), Kastamonu Havzası'nın altında özdirençli bir şekilde kendini göstermektedir. Bu bölgenin altında, yukarı doğru yükselen bir şekilde resmedilmiş büyük bir iletken anomaliye rastlanmıştır. Sıvı muhteviyatı açısından zengin olan bu anomaliye kaynak teşkil edecek derinlerdeki jeolojik yapı çözümlenememiştir. Fakat, bölgedeki bu iletken yapının varlığı, Orta Pontidlerin sismik niteliklerine, reolojik özelliklerine ve jeolojik evrimine dair önemli çıkarımlara konu olabilecek kapasitedir.

TABLE OF CONTENTS

ACKNOWLEDGEMENTS	iii
ABSTRACT	v
ÖZET	vii
LIST OF FIGURES	xi
LIST OF SYMBOLS	xx
LIST OF ACRONYMS/ABBREVIATIONS	xxii
1. INTRODUCTION	1
2. THEORY OF MAGNETOTELLURICS	6
2.1. Introduction	6
2.2. Maxwell's Equations	7
2.3. Skin Depth, Impedance, Apparent Resistivity and Phase	10
2.4. Impedance Tensor	17
2.5. Vertical Transfer Function and Induction Vectors	18
2.6. Dimensionality of MT Data	19
2.6.1. Galvanic Distortion and Distortion Tensor	20
2.6.2. Phase Tensor	22
2.7. MT Modeling	25
3. GEOLOGY AND TECTONICS	29
3.1. Evolutionary Tectonics of Anatolia and Tethyan Oceans	29
3.2. Active Tectonics of Anatolia and North Anatolian Fault	31
3.3. Neotectonics of Anatolia	33
3.4. Geology and Tectonics of Central Pontides	35
3.5. Seismicity on Central Pontides	41
4. DATA ACQUISITION AND PROCESSING	44
4.1. Introduction	44
4.2. Instrumentation and Field Procedure	44
4.3. MT Data	46
4.4. Time Series Analysis	47
4.5. Apparent Resistivity and Phase Curves	49

4.6. Tipper Data and Induction Arrows	53
4.7. Dimensionality	54
4.7.1. Phase Tensor	54
4.7.2. Ellipticity of the Phase Tensor	55
4.7.3. Beta Invariant and Three-Dimensionality of the Data	58
4.7.4. Azimuth Variations within the Region	58
5. INVERSION OF MAGNETOTELLURIC DATA	62
5.1. Regional Model	63
5.1.1. Interpretation of Preceding Modeling Attempts	65
5.1.2. Final Inversion Scheme for the Regional Resistivity Model	67
5.2. The NAF Model	70
5.3. Sensitivity Tests	73
5.3.1. Sensitivity Test for the Conductive Anomaly C	73
5.3.2. Sensitivity Tests for the Base of the Tosya Basin	74
6. RESULTS AND DISCUSSION	76
6.1. Resistivity Structure in the vicinity of the NAF and Relative Tectonic Implications	76
6.2. Resistivity Structure of Çankırı Region	83
6.3. Resistivity Structure of the Pontic Terrane	84
7. CONCLUSION	89
REFERENCES	91
APPENDIX A : RESIDUAL MAPS OF MODELING ATTEMPTS	108
APPENDIX B: FITTING CURVES OF FINAL REGIONAL MODEL	112
APPENDIX C: FITTING CURVES OF LOCAL MODEL	125

LIST OF FIGURES

Figure 2.1.	Horizontally layered medium with varying conductivity and thickness.	10
Figure 2.2.	Variation of skin depth with respect to period and resistivity. . . .	12
Figure 2.3.	(a),(b) Synthetic 1-D forward model responses based on earth model (c): A simple imitation of a migmatitic massif dome.	16
Figure 2.4.	Behavior of real induction arrows in a 2-D earth environment. . .	19
Figure 2.5.	Schematic representation of a phase tensor ellipse and its invariants β , α , Φ_{min} and Φ_{max} , where x_1 and x_2 are the coordinate reference frame.	24
Figure 3.1.	Paleogeographic sketch map at ca. 248 Ma (Triassic) showing the state of the Tethyan Oceans. Modified after Stampfli (2000). Ap: Apulia, HT: Hellenides-western Taurides externides, Me: Menderes- Taurus Block, Ss: Sanandaj-Sirjan Block, Al: Albortz.	30
Figure 3.2.	Tectonic units of Turkey are plotted alongside with the Neo-Tethyan Ophiolitic Melanges, modified after Okay et al. (1999), Advokaat et al. (2014). CACC: Central Anatolian Crystalline Complex, EAF: East Anatolian Fault, İAES: İzmir-Ankara-Erzincan Suture Zone, İZ: İstanbul Zone, KJ: Karlıova Junction, NAF: North Anatolian Fault.	32
Figure 3.3.	(a) Map representing the earthquake succession at NAF occurred in the last century. (b) Distribution of Tethyside accretionary com- plexes around Anatolia. Taken from (Şengör et al., 2005).	34

Figure 3.4.	Geological map of the study area with the MT stations. Geological map was modified after Okay et al. (2013), Aygül et al. (2015), Kaymakçı et al. (2009). K-B: Kastamonu Boyabat, KF: Kızılırmak Fault	36
Figure 3.5.	Schematic representation of the Cretaceous evolution of the Eurasian margin in Central Pontides; taken from Okay et al. (2013).	39
Figure 3.6.	Schematic diagram of the evolution of supra-subduction zone developed prior to Neo-Tethyan Collision, modified from Aygül et al. (2015).	40
Figure 3.7.	(a) Map showing the MT stations, tectonic features, and earthquake hypocenter locations in the area. Yellow pentagons represent the wide-band MT stations, earthquake hypocenters are taken from the ISC catalogue. They are plotted according to their magnitude. (b) A graph representing the earthquakes occurring near the NAF with a proximate distance of 10 km. NAF: North Anatolian Fault, EkT: Ekinveren Thrust, KF: Kızılırmak Fault, IAES: İzmir-Ankara-Erzincan Suture.	43
Figure 4.1.	Sketch diagram of a MT installation site. Red cylinders are electrodes, yellow cylinders are magnetic coils.	45
Figure 4.2.	MT equipments, Phoenix Geophysics MTU-5A	46
Figure 4.3.	Observed apparent resistivity and phase curves for xy - and yx -components of stations 1 to 9.	50
Figure 4.4.	Observed apparent resistivity and phase curves for xy - and yx -components of stations 10 to 17.	51

Figure 4.5.	Observed apparent resistivity and phase curves for xy - and yx -components of stations 18 to 25.	52
Figure 4.6.	Observed apparent resistivity and phase curves for xy - and yx -components of station 26.	53
Figure 4.7.	Observed apparent resistivity and phase pseudo-sections for xy - and yx -components.	53
Figure 4.8.	Pseudo-section of the real induction arrows for all stations.	54
Figure 4.9.	Phase tensor ellipticity variations at several frequencies of every recorded station for (a) Çankırı Region, (b) NAF Zone, (c) Pontic Terrane. (d) Pseudo-section of phase tensor ellipses filled with ellipticity values at every station. Fault-like features are shown with dashed lines. Phase tensor ellipses were reproduced after Bekin (2016).	56
Figure 4.10.	Phase tensor β variations of several frequencies at every recorded station for (a) Çankırı Region, (b) NAF Zone and (c) Pontic Terrane. (d) Pseudo-section of phase tensor ellipses filled with β angles at every station, both β° values and shapes of these ellipses reproduced after Bekin (2016).	57
Figure 4.11.	Rose diagrams for geo-electric strike variations within different bands of frequencies in three different regions of (a) Çankırı Region, (b) NAF Zone and (c) Pontic Terrane. Data separated with dashed lines indicates the frequency bands corresponds to regional strike direction.	59

- Figure 4.12. Rose diagrams for geo-electric strike directions in three different regions of (a) Çankırı Region, (b) NAF Zone and (c) Pontic Terrane. The frequencies between the range 1 Hz - 10^{-3} Hz are used. 60
- Figure 4.13. Rose diagram representation for geo-electric strike directions for all stations. The frequencies between the range 1 Hz- 10^{-3} Hz are used. 60
- Figure 5.1. Illustration of the initial model of the 3-D modeling scheme (a) from top, (b) as a cross-section. The close up version of (b) was given in the figure (c) to illustrate the mesh nodes assigned for the sea effect. Logarithmic scale was used for the colorbar. 64
- Figure 5.2. Seven 3-D modeling attempts with ModEM using different parameters as shown on the table. Dashed lines indicate the inconsistent regions on the models. Logarithmic scale was used for the colorbar. 65
- Figure 5.3. Final regional resistivity model. White dots represent the earthquake hypocenters taken from the ISC catalogue. 69
- Figure 5.4. Apparent resistivity residuals for the four components of the impedances, acquired after the 102th iteration of the final resistivity model. . . 70
- Figure 5.5. Initial model of the 3-D modeling scheme for the NAF model. Black triangles indicate the stations. Logarithmic scale was used for the colorbar. 71
- Figure 5.6. Resistivity section for the NAF model passing through model center. White dots represent the earthquake hypocenters taken from the ISC catalogue. 72

- Figure 5.7. Apparent resistivity residuals for the four components of the impedances, acquired after the 82th iteration of the NAF model. 72
- Figure 5.8. Sensitivity tests for conductive anomaly placed between the stations 4 and 5. Maps indicate the injection methodology and the graphs represents the responses of xy - and yx -components for the three sensitivity experiments. 74
- Figure 5.9. RMS values of the forward responses produced with sensitivity tests made to determine the validity of the conductive anomalies around Tosya Basin. Graph demonstrates the upper position of the injected anomaly versus RMS rates that were observed. 75
- Figure 6.1. (a) Free Bouguer anomaly values along the selected profile taken from Ateş et al. 1999. (b) Cross-section from the regional resistivity model with interpretation. ÇB: Çankırı Basin, ÇGC: Çangaldağ Complex, DC: Domuzdağ Complex, İF: İncik Formation, KA: Köşdağ Arc, KU: Kunduz Unit, KBF: Kirazbaşı Formation, KC: Küre Complex, KF-1: Kızılırmak Fault 1, KF-2: Kızılırmak Fault 2, KF-3: Kızılırmak Fault 3, NTO: Neo-Tethyan Ophiolites, NTOM: Neo-Tethyan Ophiolitic Melange, PA: Pontide Arc, TB: Tosya Basin, YF: Yaylaçayı Formation. Logarithmic scale was used for the colorbar. White dots represent the earthquake hypocenters taken from the ISC catalogue. 77
- Figure 6.2. Map view of regional resistivity model for depth slices (a) 2.5 km, (b) 6 km, (c) 10 km, (d) 15 km, (e) 20 km. CPS: Central Pontides Supercomplex, ÇGC: Çangaldağ Complex, KA: Köşdağ Arc, KBF: Kirazbaşı Formation, NTO: Neo-Tethyan Ophiolites, PA: Pontide Arc. Logarithmic scale was used for the colorbar. White dots represent the earthquake hypocenters taken from the ISC catalogue. 78

- Figure 6.3. Cross-sections of the NAF model passing through model center. FZC: Fault Zone Conductor, KA: Köşdağ Arc, KU: Kunduz Unit, TB: Tosya Basin, NTOM: Neo-Tethyan Ophiolitic Melange. Logarithmic scale was used for the colorbar. White dots represent the earthquake hypocenters taken from the ISC catalogue. 81
- Figure 6.4. Map view of regional resistivity model for depth slices (a) 0.6 km, (b) 1 km, (c) 2 km, (d) 3 km. FZC: Fault Zone Conductor, KA: Köşdağ Arc, KU: Kunduz Unit, NTO: Neo-Tethyan Ophiolites, NTOM: Neo-Tethyan Ophiolitic Melange. Logarithmic scale was used for the colorbar. White dots represent the earthquake hypocenters taken from the ISC catalogue. 82
- Figure 6.5. Simplified geological sketch of the area interpreted from MT resistivity models. Dashed lines indicate the borders solely based on qualitative interpretation of the MT results. CPS: Central Pontide Supercomplex, ÇGC: Çangaldağ Complex, KU: Kunduz Unit, KB: Kastamonu Basin, KBF: Kirazbaşı Formation, NAF: North Anatolian Fault, NTOM: Neo-Tethyan Ophiolitic Melange, YF: Yapraklı Formation 88
- Figure 7.1. Apparent resistivity residuals of trials 1 and 2 for the four components of the impedances. 108
- Figure 7.2. Apparent resistivity residuals of trials 1 and 2 for the four components of the impedances. 109
- Figure 7.3. Apparent resistivity residuals of trials 1 and 2 for the four components of the impedances. 110

Figure 7.4.	Apparent resistivity residuals of Trial 7 for the four components of the impedances.	111
Figure 7.5.	Fitting curves of station 1 for the final resistivity model.	112
Figure 7.6.	Fitting curves of station 3 for the final resistivity model.	112
Figure 7.7.	Fitting curves of station 4 for the final resistivity model.	113
Figure 7.8.	Fitting curves of station 5 for the final resistivity model.	113
Figure 7.9.	Fitting curves of station 6 for the final resistivity model.	114
Figure 7.10.	Fitting curves of station 7 for the final resistivity model.	114
Figure 7.11.	Fitting curves of station 8 for the final resistivity model.	115
Figure 7.12.	Fitting curves of station 9 for the final resistivity model.	115
Figure 7.13.	Fitting curves of station 10 for the final resistivity model.	116
Figure 7.14.	Fitting curves of station 11 for the final resistivity model.	116
Figure 7.15.	Fitting curves of station 12 for the final resistivity model.	117
Figure 7.16.	Fitting curves of station 13 for the final resistivity model.	117
Figure 7.17.	Fitting curves of station 14 for the final resistivity model.	118
Figure 7.18.	Fitting curves of station 15 for the final resistivity model.	118

Figure 7.19. Fitting curves of station 16 for the final resistivity model.	119
Figure 7.20. Fitting curves of station 17 for the final resistivity model.	119
Figure 7.21. Fitting curves of station 18 for the final resistivity model.	120
Figure 7.22. Fitting curves of station 19 for the final resistivity model.	120
Figure 7.23. Fitting curves of station 20 for the final resistivity model.	121
Figure 7.24. Fitting curves of station 21 for the final resistivity model.	121
Figure 7.25. Fitting curves of station 22 for the final resistivity model.	122
Figure 7.26. Fitting curves of station 23 for the final resistivity model.	122
Figure 7.27. Fitting curves of station 24 for the final resistivity model.	123
Figure 7.28. Fitting curves of station 25 for the final resistivity model.	123
Figure 7.29. Fitting curves of station 26 for the final resistivity model.	124
Figure 7.30. Fitting curves of station 9 for the NAF model.	125
Figure 7.31. Fitting curves of station 10 for the NAF model.	125
Figure 7.32. Fitting curves of station 11 for the NAF model.	126
Figure 7.33. Fitting curves of station 12 for the NAF model.	126
Figure 7.34. Fitting curves of station 13 for the NAF model.	127

Figure 7.35. Fitting curves of station 14 for the NAF model. 127

Figure 7.36. Fitting curves of station 15 for the NAF model. 128

Figure 7.37. Fitting curves of station 16 for the NAF model. 128

Figure 7.38. Fitting curves of station 17 for the NAF model. 129

Figure 7.39. Fitting curves of station 18 for the NAF model. 129

Figure 7.40. Fitting curves of station 19 for the NAF model. 130

LIST OF SYMBOLS

A	Anisotropy
B	Magnetic induction
C	Distortion tensor
C_d	Data covariance matrix
C_m	Model covariance matrix
d	Data space
D	Displacement current
D_p	Data response function
E	Electric field
<i>f</i>	Frequency
F	Forward solution
<i>g</i>	Gain
H	Magnetic field
H_m	Hessian matrix
I	Identity matrix
J	Current density
J_m	Jacobian matrix
<i>k</i>	Wave number
m	Model space
<i>m_c</i>	Cementation factor
R	Rotation matrix
<i>R_n</i>	Recurrence relationship
<i>S</i>	Shear
<i>t</i>	Time
<i>T</i>	Tipper
<i>T_w</i>	Twist
<i>Q_{encl}</i>	Volume charge density
X	Real part of the impedance tensor

Y	Imaginary part of the impedance tensor
Z	Impedance tensor
Z_{reg}	Regional impedance tensor
α	Non-invariant angle
β	Skew angle
δ	Skin depth
ϵ	Electric permittivity
κ	Porosity
μ	Magnetic permeability
ω	Angular frequency
σ	Conductivity
ρ	Resistivity
ρ_a	Apparent resistivity
ρ_f	Resistivity of the pore-fluid
ρ_r	Resistivity of the anomaly
ϕ	Phase
φ	Azimuth
Φ	Phase tensor
ν	Regularization parameter
Υ	Tikhonov matrix
τ	Penalty functional
ψ	Regional strike angle

LIST OF ACRONYMS/ABBREVIATIONS

1-D	One-dimensional
2-D	Two-dimensional
3-D	Three-dimensional
ATB	Anatolide-Tauride Block
CP	Central Pontides
CPS	Central Pontides Supercomplex
CD-CAT	Continental Dynamics-Central Anatolian Tectonics
ÇGC	Çangaldağ Complex
EAF	East Anatolian Fault
EM	Electromagnetic
GPS	Global Positioning System
HSZ	Hellenic Subduction Zone
İAESZ	İzmir-Ankara-Erzincan Suture Zone
KBF	Kirazbaşı Formation
KOERI	Kandilli Observatory and Earthquake Research Center
KB	Kastamonu Basin
KBF	Kirabaşı Formation
KC	Küre Complex
KU	Kunduz Unit
MT	Magnetotellurics
NAF	North Anatolian Fault
NAK	North Anatolian Keirogen
NASZ	North Anatolian Shear Zone
NLCG	Non-linear conjugate gradients
NSF	National Science Foundation
NTO	Neo-Tethyan Ophiolites
NTOM	Neo-Tethyan Ophiolitic Melange
PA	Pontide Arc

RMS	Root mean square
TE	Transverse electric
TM	Transverse magnetic
TB	Tosya Basin
USGS	United States Geological Survey
VTF	Vertical transfer function

1. INTRODUCTION

Studying the Earth has been a subject to human curiosity ever since the antiquity. The ones who provided better insight on the rock we live on, not only encouraged societies to adapt to their surroundings, but also propose a vision on the whereabouts of humanity in space and geological time. From the early works of Eratosthenes to modern geological paradigm, the structure of the Earth was revealed as a very complex, dynamic and ever-evolving mechanism. Even with today's technological advancements, a vast portion of this large mechanism still remains unknown. For the last century, physical applications that were developed under the name of geophysical methods, had become a common practice among geoscientists, especially after the advancements in computer technology. Geophysical methods are tools that are used to investigate the Earth's physical properties. In this thesis, magnetotelluric (MT) method is applied to reveal the Earth's electrical characteristics by using natural electromagnetic field variations occurring within the Earth and its magnetosphere.

The theory of MT method was developed independently by three authors: Rikitake (1948), Tikhonov (1950) and Cagniard (1953). Since the early 1960's, it has been extensively used to depict the electrical conductivity (reciprocal of electrical resistivity) variations within the Earth. What makes magnetotelluric method utterly different from other electromagnetic methods is passive nature of the field source and wide range of frequency that the source signals provide. Propagation of naturally occurring electromagnetic waves depend on frequencies and the conductivity of the subsurface medium. Researchers are able to select different sampling rates to reach different skin depths. This means that the method can be used for wide variety of subjects such as engineering purposes (investigation of geothermal systems, mineral exploration, etc.) and examination of deep tectonic structures in the lithosphere.

Rheology is the key factor that defines the behavior of Earth materials and it is related to many parameters such as temperature, fluid content, pore geometry, pore-fluid interconnectivity, mineralogical and chemical compositions of the rock (Bürgmann

and Dresen, 2008). Presence of fluids in rocks can change its mechanical strength by microcracking, hydrofracturing, inducing the pore connectivity and reducing the effective normal stress (Jiracek et al., 2007). As a consequence of these, presence of fluids at crustal and mantle depths are found to influence the tectonic processes and earthquake generation (Zhao et al., 2004). Great amounts of fluid are displaced via convection during tectonic processes. This is why it is important to consider mechanical properties of a region, while interpreting its tectonic state.

A rock completely deprived of conductive phases should demonstrate high resistivity values. Aqueous saline fluids and partial melts within the rock matrix of geological formations could enhance the bulk conductivity of rocks by several orders of magnitude via ionic conduction (Unsworth, 2010). However, the assesment of such conductive anomalies should be handled precisely, because these features might not always have a direct link with the rheology of the medium. Additional geological and geophysical data can help to constrain such information while depending on the rocks thermodynamic state. For instance, a porous and fluid-filled sedimentary media near the surface could easily be related to high conductivity values, whereas existence of a metamorphic unit devoid of effective porosity can be assigned to high resistivity anomalies. For this reason, it may appear useful to exploit fluid-sensitive techniques when the formation history and future dynamic movements of certain geological areas are investigated.

So far, MT method has proven to be capable in designing hypotheses for fluid-induced tectonic mechanisms and this aspect of MT was discussed in many review articles (Unsworth and Bedrosian, 2004; Ritter et al., 2005; Unsworth et al., 2005; Jiracek et al., 2007; Gürer and Bayrak, 2007; Unsworth, 2010; Becken and Ritter, 2012). In MT literature, earthquakes occurrences are mostly observed on resistive sides of the conductive-resistive interfaces (Gürer and Bayrak, 2007). This situation may be explained by the fluid migration from a conductive environment to a resistive side by changing the stress environment and thermodynamic state in the area. However, fluid-induced seismicity have been depicted and interpreted in many forms. San Andreas Fault (SAF), in California has been center of scientific studies for detecting the effects

of fluid intrusion into the fault zones. Bedrosian et al. (2004) imaged the anomalously extending fault damage zone at the creeping segment of SAF. This spatial span of the imaged fault zone coincides with the velocity strengthening concept caused by highly porous weakened material at shallow depths of the faults (Scholz, 1998). Later, the source of this fluid was found to be derived from a deeper trapped fluid chamber (Becken et al., 2011). Moving to the south along the San Andreas Fault, same entrapped fluid source is associated with non-volcanic tremor events caused by over-pressurization within the environment when there is no porous-conductive pathway exists towards the fault zone. In contrast to seismic induction of fluids, the fault segments representing seismic gaps depicted as highly resistive bodies appearing on both sides of the fault. This situation infers to presence of strong mechanical base units devoid of an fluid filled interconnected pore structure along the fault, in other words, asperities (Unsworth et al., 1999, Goto et al., 2005; Karas et al., 2017). This type of zones do not release their stresses by small- to mid-scale magnitude earthquakes and have the tendency to produce large earthquakes due to long stress build up during the interseismic period (Scholz, 1998).

For deeper fluid inclusions, researchers may have to address pressure, temperature and mechanical properties of the area in addition to the conductivity anomalies observed (Jiracek et al., 2007). Along the San Andreas Fault, Becken et al. (2011) related the seismic behavior near Parkfield and Cholame regions with fluid inclusion to the fault zone from a trapped metamorphic fluid cap that originate as a result of dehydration of the mantle material via prograde metamorphism (Fulton and Saffer, 2009). Similarly, a collection of MT studies took place along the Himalayas within the INDEPTH project (Unsworth et al., 2005). They found an extensive conductive structure lying flat beneath the thick brittle crust. The source of this conductive region is interpreted as partially molten layer mixed with aqueous fluids, which were created due to thermal conditions induced by the thickened lithosphere and possible fluid intrusion from subducting Indian lithosphere.

Through MT investigations, similar implications have been subject to Anatolian tectonics and especially NAF. Tank et al. (2005) investigated the resistivity structure

along İzmit segment of the NAF and detected a deep conductor below the seismogenic zone. This conductor is interpreted to be related to the seismic activity in the segment and post-seismic slip observed after the 1999, İzmit Earthquake. Similar type of mechanism was observed in the Marmara Sea where the resistivity variations were found to be related to microseismic activity in the region (Kaya et al., 2013). Karaş et al. (2017) showed that even in small distances within the same segment of the NAF, structures of faults might show drastically different characteristics, thus leading to heterogeneous rheological environments, which might have considerable effects on some investigation methodologies. Türkoğlu et al. (2015) compared the resistivity structures of the NAF and the East Anatolian Fault (EAF) in the Eastern Anatolia. According to the findings of this study, lower crustal conductor depicted in the NAF appear much less conductive compared to the one in the EAF. This difference between two sections was interpreted to stem from relative maturity difference between the faults, which might infer to transfer of strain localization to the upper crust with increasing age. Another theory is that the fluid source might be another factor that controls the conductivity of these lower-crustal conductors, which might be related to the paleo-tectonic events (e.g. subduction, delamination) took place near the area of investigation.

Studies aiming to understand the historical development of major suture zones may provide invaluable information due to the basic fact that these zones comprise evidence on the subduction that took place and the collision when the two blocks converge each other. The case of the Pontides in Northern Anatolia and the sutures that are associated with it, provide an ideal laboratory for understanding the dynamic processes. These sutures are İzmir – Ankara – Erzincan Suture (İAES) and Intra-Pontide Suture. In particular, the materials that can be found in the vicinity of İAES deliver information about two oceanic lithospheres; (i) Paleozoic-Mesozoic aged Paleo-Tethys and (ii) Mesozoic aged Neo-Tethys. The aim of this thesis is to determine the crustal electrical resistivity structure at a zone that includes the Central Pontides Metamorphic Supercomplex, North Anatolian Fault (NAF) and İzmir-Ankara-Erzincan Suture Zone. In terms of the conductivity structure, this thesis intend to point out the behavior of the area, which experienced closure of Paleo- and Neo-Tethys oceans, subduction, collision, extension, uplift and finally strike-slip faulting during its development (Okay

et al., 2017; 2013; Kaymakçı et al., 2009, Hippolyte et al., 2016). For these purposes, 26 MT observations were carried out at two field campaigns in 2012 as part of a multidisciplinary project entitled; Continental Dynamics/Central Anatolian Tectonics (CD/CAT) funded by the U.S. NSF.

In the following chapter, theoretical concepts of the MT method will be reported. Chapter 3 gives the necessary information on the geology and tectonics of the study region. Data acquisition and processing steps will be explained in Chapter 4. Inversion steps and methodology that is used in this thesis are described in Chapter 5. Finally, the results of the 3-D inversions and data analyses will be discussed in Chapter 6 to provide new information on the area. In the conclusion, Chapter 7, the results will be summarized.

2. THEORY OF MAGNETOTELLURICS

2.1. Introduction

The MT method is an electromagnetic (EM) geophysical exploration tool that uses the naturally occurring EM fields to investigate the Earth's electrical characteristics. The natural EM fields take their sources by two distinct perpetual phenomena. At frequencies greater than 1 Hz, fields are generated by global lightning activity; while the interaction between the Earth's magnetosphere and solar wind gives rise to the fields propagating with frequencies below 1 Hz. Both sources tend to decrease in amplitude at the frequency range around 1 Hz known as dead-band. Because of the passive nature of the sources, quality of the measured data is directly related to the Sun's activity.

Penetration depth of the fields is inversely related to the frequency, where the amount of measurement time is the key parameter for determining the target depth of a survey (Cagniard, 1953). Because the natural fields have this wide spectral range, MT method can be used to investigate the Earth's subsurface in many aspects.

MT theory was independently developed by three different authors: Rikitake (1948), Tikhonov (1950) and Cagniard (1953). They all assumed a planar EM wave propagating in an isotropic medium and linked this wave with the Earth's subsurface conductivity structure with complex impedance ratio (\mathbf{Z}) of measured horizontal electric and magnetic fields. MT method has been improving ever since and proven its validity numerous times as a proper sub-surface exploration tool. An introduction to the theory will be presented in the following parts. Readers who are interested in a more detailed description can check the reputable textbooks that focus on the MT method (Kaufman and Keller, 1981; Simpson and Bahr, 2005; Chave and Jones, 2012).

2.2. Maxwell's Equations

The physics of EM waves that propagates the Earth are governed by well-known Maxwell's equations (2.1-4):

$$\nabla \cdot \mathbf{D} = Q_{encl} \quad (2.1)$$

$$\nabla \cdot \mathbf{B} = 0 \quad (2.2)$$

$$\nabla \times \mathbf{E} = -\frac{\partial \mathbf{B}}{\partial t} \quad (2.3)$$

$$\nabla \times \mathbf{H} = \mathbf{J} + \frac{\partial \mathbf{D}}{\partial t} \quad (2.4)$$

where \mathbf{E} is the electric field (in *Volt/meter*), \mathbf{H} is the magnetic field (in *Ampere/meter*), \mathbf{B} is the magnetic induction (in *Tesla*), \mathbf{D} is electric displacement (in *Coulomb/meter²*), Q_{encl} is the volume charge density (in *Coulomb/meter³*) and \mathbf{J} is the electric current density (in *Ampere/meter²*) (Kaufman and Keller, 1981). Here, equations 2.1 and 2.2 describe the nature of electric and magnetic flux. While the first one describes the origin of electric flux as the charge density of the material, the latter describes the necessary dipole nature of magnetic fields. Equation 2.3 is called the Faraday's law and states that, through any closed loop, rate of change in the magnetic field induces electric field. Similarly, Ampere's law (2.4) describes this relation in reverse. Any conducting medium that holds electric current \mathbf{J} , induces magnetic field. Second term on the right in equation 2.4 is the Maxwell's addition to the original Ampere's formula, which describes the second source of magnetic induction as the time rate of change of displacement currents related to the of individual molecules in an dielectric medium. In classical MT applications, Maxwell's term can be neglected due to the very small contribution to the measured electrical field compared to the \mathbf{J} . Application of the laws on any medium defined with ϵ , μ and σ ; following constitutive relations are required (Chave and Jones, 2012).

$$\mathbf{B} = \mu\mathbf{H} \quad (2.5)$$

$$\mathbf{D} = \epsilon\mathbf{E} \quad (2.6)$$

$$\mathbf{J} = \sigma\mathbf{E} \quad (2.7)$$

where ϵ is the electrical permittivity (in *Farad/meter*), μ is magnetic permeability (in *Henry/meter*) and σ is the conductivity (in *Siemens/meter*) of the medium. Substituting the 2.5, 2.6 and Ohm's Law (2.7) into 2.4, and assuming ϵ does not vary with time.

$$\nabla \times \mathbf{H} = \mathbf{J} + \epsilon \frac{\partial \mathbf{E}}{\partial t} \quad (2.8)$$

By taking the curl of 2.3 then using the vector identity $\nabla \times (\nabla \times \mathbf{F}) = \nabla \cdot (\nabla \mathbf{F}) - \nabla^2 \mathbf{E}$, in accordance with assuming that there are no free charges in the Earth (i.e. $\nabla \cdot \mathbf{E} = 0$):

$$\nabla^2 \mathbf{E} = \mu_0 \sigma \frac{\partial \mathbf{E}}{\partial t} + \mu_0 \epsilon \frac{\partial^2 \mathbf{E}}{\partial t^2} \quad (2.9)$$

In air, σ is zero, meaning the part related with conduction currents becomes zero; thus 2.9 can be simplified into a wave equation ($\nabla^2 \mathbf{E} - \mu\epsilon \partial_t^2 \mathbf{E} = 0$). However, the Earth is relatively conductive compared to air, but contribution of the displacement currents is too small compared to conduction currents. Then, the behavior of EM motion can be described with a diffusion equation:

$$\nabla^2 \mathbf{E} - \mu\sigma \frac{\partial \mathbf{E}}{\partial t} = 0 \quad (2.10)$$

Assuming sinusoidal time variation for EM waves, \mathbf{E} can be written as $E = E_0 e^{-i\omega t}$. Then, 2.10 takes the following form:

$$\nabla^2 \mathbf{E} = i\omega\mu_0\sigma \mathbf{E} \quad (2.11)$$

By following similar processes, same diffusion equation can be achieved for the magnetic fields:

$$\nabla^2 \mathbf{B} = i\omega\mu_0\sigma \mathbf{B} \quad (2.12)$$

Then, the state of EM waves propagating in the Earth, that are used essentially in MT method, are named as quasi-stationary fields, whose behavior is described by the following set of Maxwell's equations.

$$\nabla \cdot \mathbf{E} = 0 \quad (2.13)$$

$$\nabla \cdot \mathbf{B} = 0 \quad (2.14)$$

$$\nabla \times \mathbf{E} = i\omega\mu \mathbf{H} \quad (2.15)$$

$$\nabla \times \mathbf{H} = \sigma \mathbf{E} \quad (2.16)$$

2.3. Skin Depth, Impedance, Apparent Resistivity and Phase

By applying Maxwell's equations over a N horizontally layered medium (Figure 2.1), EM fields are defined as plane waves propagating with diffusion motion rather than a wave motion. This is not the real behavior of EM waves penetrating into the Earth, however the approximation is proven to be reliable within the periods less than 10^5 seconds and one should consider spherical motion after this threshold (Madden and Nelson, 1964). More complex scenarios has to be applied when an extrinsic motional induction source (ocean and seas) is affecting the primary geomagnetic field (Chave and Jones, 2012). In classical sense, primary magnetic field H_0 is generated by the current in the source plane.

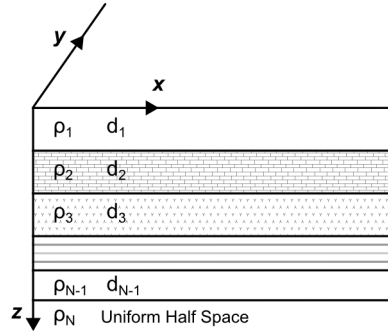


Figure 2.1. Horizontally layered medium with varying conductivity and thickness.

Variation of magnetic field gives rise to primary electric field E_0 . While primary magnetic field does not vary in the z direction, E_0 does and causes currents to serve as a source for secondary fields. Considering the primary fields do not vary with horizontal dimensions (Kaufman and Keller, 1981):

$$\frac{\partial H_{0y}}{\partial x} = \frac{\partial H_{0y}}{\partial y} = \frac{\partial E_{0x}}{\partial x} = \frac{\partial E_{0x}}{\partial y} \equiv 0 \quad (2.17)$$

Secondary fields (E_x and H_y) are the only ones that vary in the z direction, thus equal to the total EM fields (Kaufman and Keller, 1981):

$$E = (E_x, 0, 0) \quad H = (0, H_y, 0) \quad (2.18)$$

Using the Faraday's (2.15) and Ampere's (2.16) laws by considering 2.18:

$$\frac{\partial E_x}{\partial z} = i\omega\mu H_y \quad (2.19)$$

$$\frac{\partial H_y}{\partial z} = -\sigma E_x \quad (2.20)$$

Taking the derivatives with respect to z ,

$$\frac{d^2 E_x}{dz^2} = -i\omega\mu\sigma E_x = k^2 E_x \quad (2.21)$$

$$\frac{d^2 H_y}{dz^2} = -i\omega\mu\sigma H_y = k^2 H_y \quad (2.22)$$

where $k^2 = i\omega\mu\sigma$ is the square of the wavenumber. Taking the liberty of using $\mu = \mu_0 = 4\pi \times 10^{-7} H/m$, the wave number k becomes related to skin depth δ as follows

$$\delta = \sqrt{\frac{2}{\sigma\mu_0\omega}} \cong \sqrt{\frac{1}{\sigma\mu_0\omega}} \cong 503.2 \sqrt{\frac{1}{\sigma f}} \quad (2.23)$$

where f is the frequency of the signal. From 2.23, it can be easily seen that the frequency is inversely related with skin depth, while resistivity of the medium is directly proportional. This means that EM waves propagating with higher periods are capable of penetrating into deeper structure before they dissipate their energy. The energy dissipation becomes more apparent in conductive environments (Chave and Jones, 2013). This relation between the frequency and the signal can be seen in Figure 2.2.

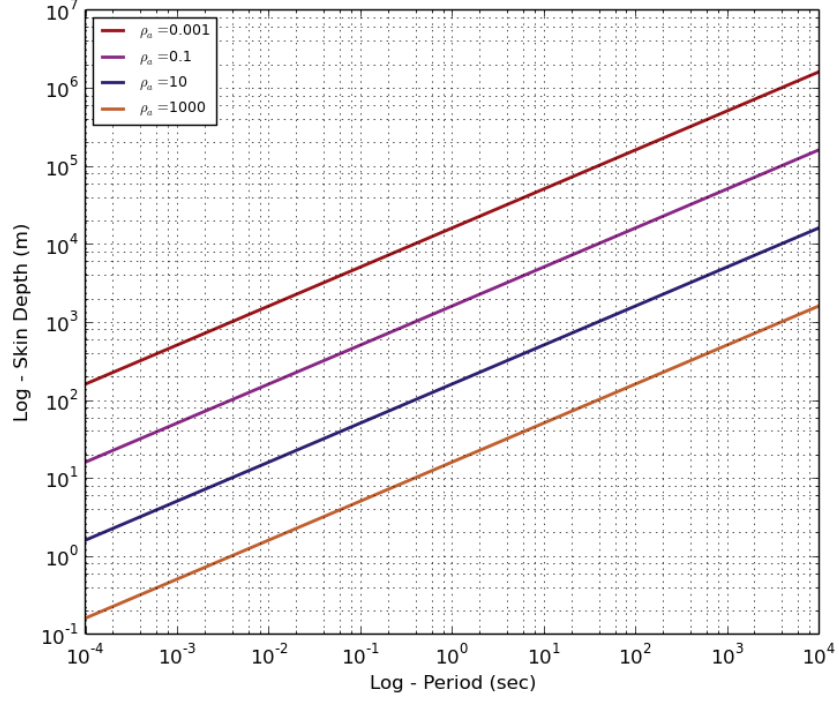


Figure 2.2. Variation of skin depth with respect to period and resistivity.

Equations 2.21 and 2.22 are valid except for the boundaries between the layers due to the discontinuity of second derivative expressions. Assuming that the tangential components of the fields are continuous through the interfaces, boundary conditions become;

$$E_x^{(n)} = E_x^{n+1} \quad (2.24)$$

$$H_y^{(n)} = H_y^{n+1} \quad (2.25)$$

For the electric field, solutions to 2.21, 2.22, 2.24 and 2.25 are:

$$E_x^{(n)} = A_n e^{ik_n z} + B_n e^{-ik_n z} \quad (2.26)$$

where k_n is the wavenumber for the n^{th} layer. After inserting this solution 2.26 into 2.19,

$$H_y = (i\omega\mu)^{-1} \frac{\partial E_x}{\partial z} \quad (2.27)$$

$$H_y^{(n)} = \frac{k_n}{\omega\mu} (A_n e^{ik_n z} - B_n e^{-ik_n z}) \quad (2.28)$$

The solution applies to every boundary layer within N-layered medium. A_n represents the field amplitude that is directly related with depth, while the other way around is valid for the term B_n . Because there is no boundary present in a homogeneous model, analytical solutions can be easily derived as follows:

$$E_x = A e^{ikz} \quad (2.29)$$

$$H_y = \frac{k}{\omega\mu} A e^{ikz} \quad (2.30)$$

then at the surface of the Earth,

$$E_x(0) = A \quad (2.31)$$

$$H_y = \frac{k}{\omega\mu} E_x(0) \quad (2.32)$$

The amplitudes of the fields contain information on both primary and secondary fields. Because, only the information on secondary variations are needed, the effects of primary fields has to be eliminated. The way of doing this is to define the *electromagnetic impedance of uniform medium* (Z_{ij}) (Cagniard, 1953; Kaufman and Keller, 1981).

$$Z_{xy} = \frac{E_x}{H_y} = \frac{\omega\mu}{k} = \frac{\omega\mu}{(i\sigma\mu\omega)^{0.5}} \quad (2.33)$$

In order to generalize this solution, one should consider a more realistic N-layered medium earth model. The analytical solutions to this problem can be achieved by similar manner. Firstly, inserting the solutions for the field 2.26 and 2.28 into 2.33,

$$Z_{xy}^{(j)} = \frac{E_x^{(j)}}{H_y^{(j)}} = \frac{\omega\mu_0}{k_j} \frac{(A_j e^{ik_j z} + B_j e^{-ik_j z})}{(A_j e^{ik_j z} - B_j e^{-ik_j z})} \quad (2.34)$$

where j is the layer number. Dividing this by $(A_j B_j)^{0.5}$,

$$Z_{xy}^{(j)} = \frac{\omega\mu_0}{k_j} \frac{((A_j/B_j)^{0.5} e^{ik_j z}) + ((B_j/A_j)^{0.5} e^{-ik_j z})}{((A_j/B_j)^{0.5} e^{ik_j z}) - ((B_j/A_j)^{0.5} e^{-ik_j z})} \quad (2.35)$$

Using the expression $q_j = -\ln((A_j/B_j)^{0.5})$, we get:

$$Z_{xy}^{(j)} = \frac{\omega\mu_0}{k_j} \frac{e^{ik_j z - q_j} + e^{ik_j z + q_j}}{e^{ik_j z - q_j} - e^{ik_j z + q_j}} \quad (2.36)$$

Second expressions is definition of cotangent hyperbolic function:

$$Z_{xy}^{(j)} = \frac{\omega\mu_0}{k_j} = \coth(ik_j z_j - q_j) \quad (2.37)$$

Using the boundary condition $Z_{xy}^{(j)}(z_j + 0) = Z_{xy}^{(j)}(z_j - 0)$,

$$\begin{aligned}
Z_{xy}^{(j)}(z_j + 0) &= \frac{\omega\mu_0}{k_j} \coth(ik_j z_j - q_j) \\
q_j &= ik_j z_j - \coth^{-1}\left(\frac{k_j}{\omega\mu_0} Z_{xy}^{(j)}(z_j + 0)\right)
\end{aligned} \tag{2.38}$$

Hence,

$$Z_{xy}^{(j-1)}(z_j + 0) = -\frac{\omega\mu_0}{k_j} \coth\{ik_j - 1h_j - 1 - \coth^{-1}\left[\frac{k_j}{\omega\mu_0} Z_{xy}^j(z_j + 0)\right]\} \tag{2.39}$$

This recurrent relationship can be applied to every boundary within the earth model. To express the amplitude loss to heat dissipation with increasing z , the last layer must be taken as a homogeneous half-space. By applying 2.39 from last layer to the surface, one could acquire the recurrence relationship (R_N) (Zhdanov & Keller, 1994)

$$\begin{aligned}
R_N = \coth\{-ik_1 h_1 + \coth^{-1}\left[\frac{k_1}{k_2} \coth(ik_2 h_2 + \coth^{-1}\left[\frac{k_2}{k_3} \coth(ik_3 h_3 \dots \right.\right.\right. \\
\left.\left.\left. \dots + \coth^{-1}\left[\frac{k_{N-1}}{k_N} \dots\right]\right]\right]\right]\} \tag{2.40}
\end{aligned}$$

Frequency dependent impedance measured at the surface is then,

$$Z_{xy}(\omega) = \frac{\omega\mu_0}{k_1} R_N \tag{2.41}$$

and from 2.41,

$$\rho_a(\omega) = \frac{1}{\omega\mu_0} |Z_{ij}(\omega)|^2 \quad (2.42)$$

$$\phi(\omega) = \tan^{-1} \left\{ \frac{\text{Im}(Z_{ij}(\omega))}{\text{Re}(Z_{ij}(\omega))} \right\} \quad (2.43)$$

Here, ρ_a is the apparent resistivity, where Z_{ij} is the complex numbered EM impedance and the argument of it is equal to the phase angle (ϕ) between the electric and magnetic fields. Apparent resistivity is a similar expression to the one that is used in electric methods and it is conventionally the first interpreted parameter during a MT investigation. It is used to depict the subsurface electrical resistivity distribution depending on frequency of the signal. In an isotropic half-space, phase angle must be equal to 45° and angles above 45° correspond to decreasing resistivity, while the opposite analogy is also valid. Because of this property of the phase, it is considered as more sensitive to the changes in real resistivity of the medium. For 1-D earth problem, apparent resistivity and phase can be calculated by the analytical recursive relationships (2.41) described above. Figure 2.3 shows an example of the apparent resistivity and phase responses produced by this methodology.

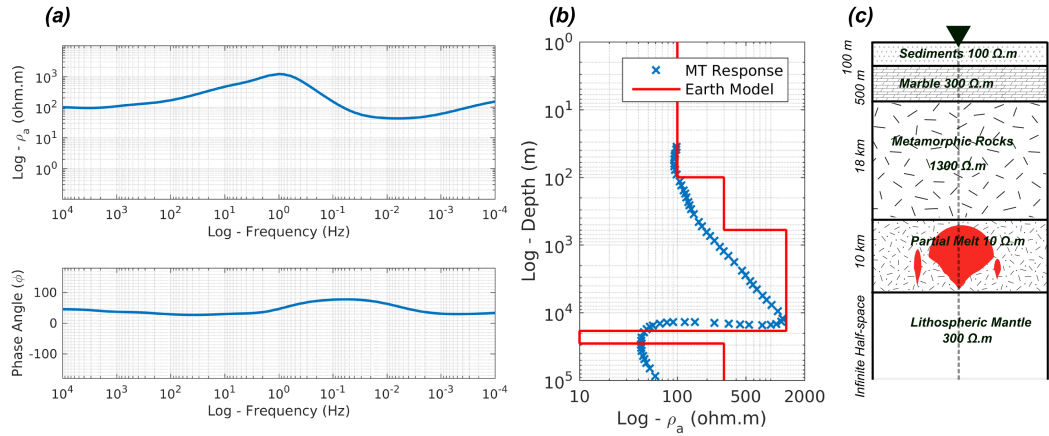


Figure 2.3. (a),(b) Synthetic 1-D forward model responses based on earth model (c):
A simple imitation of a migmatitic massif dome.

2.4. Impedance Tensor

Cagniard's approach to the MT problem is useful for some cases, but mostly impractical for the more elaborative research. For instance, on Figure 2.3., the partial melt layer on the synthetic model is clearly a 3-D structure; metamorphic core might have an anisotropic medium or uppermost sediment layers may include normal faulting systems that hold current density in it. Hence, for dimensionally complex considerations, a more holistic approach to the data analysis has to be applied. In order to achieve this goal, one initially has to define the impedance transfer functions (Z_{ij}) as a tensor relationship.

$$\begin{bmatrix} E_x \\ E_y \end{bmatrix} = \begin{bmatrix} Z_{xx} & Z_{xy} \\ Z_{yx} & Z_{yy} \end{bmatrix} \cdot \begin{bmatrix} H_x \\ H_y \end{bmatrix} \quad (2.44)$$

$$\mathbf{E} = \mathbf{Z} \cdot \mathbf{H} \quad (2.45)$$

\mathbf{Z} here, is called the impedance tensor and it holds the essential information of conductivity and polarizations of subsurface electrical structure. For a 1-D earth case, diagonal components are taken as zero and off-diagonal impedances satisfy the equation $Z_{xy} = -Z_{yx}$. Whereas, in a perfect 2-D earth, one of the off-diagonal elements must be parallel to the geo-electric strike direction ($Z_{xy} \neq Z_{yx}$ & $Z_{xx} = Z_{yy} = 0$). Firstly presented by Swift (1967); the idea of analysing the two-dimensional subsurface resistivity by simply rotating the impedance tensor so that the diagonal elements (Z_{xx} and Z_{yy}) are minimized, have been intensively used in MT analysis. In 2-D MT analysis, two modes of impedances are used after the rotation of the tensor: TE and TM. TE (Transverse Electric) mode represents the polarization of the electric field along the geo-electric strike, while the TM (Transverse Magnetic) mode uses the polarization of magnetic field along the geo-electric strike. However, such 2-D approximations should not be applied for rather complex structures, since it might introduce spurious features into resistivity models (Ledo, 2005). In 3-D case, all of the tensor elements are accepted as different and analysed as a whole to obtain the true resistivity of the medium. Prop-

erties of impedance tensor can be analysed to investigate the dimensional essence of the data, thus distortion analysis and removal. Some of the dimensionality techniques used on MT data will be explained in the following chapters.

2.5. Vertical Transfer Function and Induction Vectors

Elements of the impedance tensor (\mathbf{Z}) are calculated from horizontal electric and magnetic field components. However, in a classical MT investigation, five time-series channels are recorded: E_x, E_y, H_x, H_y and H_z . By recording vertical magnetic field (H_z), another tensor relationship, which is described by the ratio between horizontal and vertical magnetic fields, becomes available for use (Chave and Jones, 2012).

$$\begin{aligned}
 H_z &= \mathbf{T} \cdot \mathbf{H}_h \\
 H_z &= T_x H_x + T_y H_y \\
 T_x &= \frac{H_z}{H_x} \quad T_y = \frac{H_z}{H_y}
 \end{aligned} \tag{2.46}$$

Here, \mathbf{T} is called the vertical transfer function (VTF) or tipper. Tipper data are sensitive to the lateral conduction deviations. This property of tipper can be used as data for 2-D and 3-D resistivity modeling or as an informative tool named as induction arrows. An induction arrow is represented by a vector originated from a datum and points out towards shortest path to the nearby anomalous current concentrations (Parkinson, 1959). In Wiese convention the opposite situation is valid and induction arrows point away from the anomaly (Wiese, 1962). The magnitude (M) and azimuth (φ) of the real and imaginary vectors can be calculated by

$$\begin{aligned}
M_{Re} &= \sqrt{Re(T_x^2) + Re(T_y^2)} \\
M_{Im} &= \sqrt{Im(T_x^2) + Im(T_y^2)} \\
\varphi_{Re} &= \tan^{-1}\left(\frac{Re(T_y)}{Re(T_x)}\right) \\
\varphi_{Im} &= \tan^{-1}\left(\frac{Im(T_y)}{Im(T_x)}\right)
\end{aligned} \tag{2.47}$$

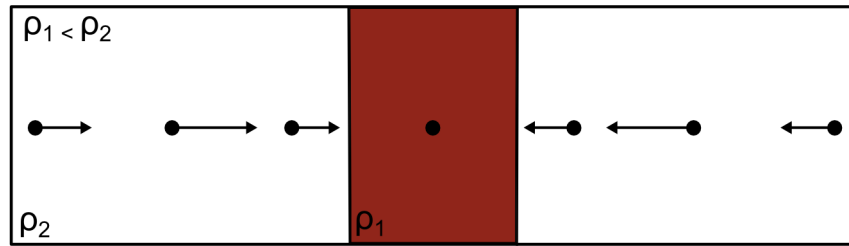


Figure 2.4. Behavior of real induction arrows in a 2-D earth environment.

Because it only depends on magnetic field variations, tipper data are not affected by galvanic distortion caused by near surface heterogeneities. So it can be used to interpret regional strike direction. Figure 2.4 shows the behavior of the induction arrows in the presence of a thin conductor slice lying inside a resistive medium, a sketch of a perfect 2-D Earth geometry. Over the conductor, induction arrows must be as small as possible and the magnitude of the vectors must increase while moving away from the conductor until the electric fields caused by the conductor reach its skin depth threshold.

2.6. Dimensionality of MT Data

Using Swift's method to approximate a 2-D conductive earth, has been proven to be efficient in numerous case studies. The method uses the basic principle of rotating the impedance tensor to regional strike angle by multiplying it with a rotation matrix $R(\psi_{2D})$ (Swift, 1967).

$$\mathbf{Z}_{2D} = \mathbf{R}_{\psi_{2D}} \mathbf{Z} \mathbf{R}_{\psi_{2D}}^T \quad (2.48)$$

Originally, regional strike angle ψ_{2D} was determined by minimizing the diagonal elements and maximizing off-diagonal elements of the impedance tensor. Incidentally following the method of Sims et al. (1971), this is equal to:

$$4\psi_{2D} = \tan^{-1} \left\langle \frac{(Z_{xx} - Z_{yy})(Z_{xy} + Z_{yx})^* + (Z_{xx} - Z_{yy})^*(Z_{xy} + Z_{yx})}{|Z_{xx} - Z_{yy}|^2 - |Z_{xy} + Z_{yx}|^2} \right\rangle \quad (2.49)$$

where * denotes to the complex conjugate of the element. Since this formulation only deals with amplitude variations of \mathbf{Z} , it also contains distortion of the electric field within itself. Hence, true \mathbf{Z}_{2D} and ψ_{2D} can only be obtained by distortion-free data or implementing a method that is unaffected from distortion.

2.6.1. Galvanic Distortion and Distortion Tensor

Observed impedance tensor contains information about galvanic distortion effects caused by near-surface heterogeneities. Thus, a more comprehensive dimensional analysis that deals with the total distortion on impedance tensor must be considered. In this sense, one can describe the true impedance tensor (\mathbf{Z}_{reg}) by multiplying the observed impedance (\mathbf{Z}_{obs}) with a regulation-distortion matrix (\mathbf{C}) (Groom and Bailey, 1988).

$$\mathbf{Z}_{obs} = \mathbf{C} \cdot \mathbf{Z}_{reg} \quad (2.50)$$

This is the general idea behind every distortion removal technique available, where \mathbf{C} is a 2×2 real matrix and corresponds to

$$\mathbf{C} = \begin{bmatrix} a & b \\ c & d \end{bmatrix} \quad (2.51)$$

$$\mathbf{C} = g\mathbf{T}_w\mathbf{S}\mathbf{A} \quad (2.52)$$

Here, a and d are the parameters that represent the amplitude of the distortion effect, while parameters b and c are the ones that govern the rotational input of the total distortion. As described by Groom and Bailey (1989); \mathbf{T}_w here is the twist tensor which rotates the undistorted impedance variants with an angle; \mathbf{S} is the shear tensor, which is self-explanatory; \mathbf{A} is the anisotropy or splitting tensor and g is the site gain, which is a scalar entity describing the total static-shift effect (Figure 2.5).

Theoretically, for impedance based 3-D modeling, it should not be a necessity to remove galvanic distortion, if one can resolve all inhomogeneities with a very fine gridded model space (Chave and Jones, 2012). However, this situation is overtly delimited by the required computational load. All of the stable methods regarding the removal of galvanic distortion are in need of a 2-D approximation of conductivity structure (Groom and Bailey, 1989). Moreover, one can not or should not establish an opinion on dimensionality by using these methods, where the structure is dominated by 3-D features. Fortunately, there are several methods available for making valid assumptions about dimensionality of the data without the removal of galvanic distortion (Caldwell et al., 2004; Bibby et al., 2005). In the following chapters, these methods are going to be described with their implications on MT data and modeling.

2.6.2. Phase Tensor

MT phase tensor (Φ) was introduced as a powerful tool for investigating dimensionality of MT data (Caldwell et al., 2004). Based on Bibby's (1986) ideas, phase tensor was developed on the basis that it is not affected from galvanic distortion.

$$\mathbf{Z} = \mathbf{X} + i\mathbf{Y} \quad (2.53)$$

$$\Phi = \mathbf{X}^{-1}\mathbf{Y} \quad (2.54)$$

where \mathbf{X}^{-1} is the inverse of the real impedance tensor and \mathbf{Y} is the imaginary part of it. Let us assume that there is a tensor \mathbf{C} that describes the distortion effect over true regional impedances. $\mathbf{Z}_{reg} = \mathbf{X}_{reg} + i\mathbf{Y}_{reg}$

$$\begin{aligned} \Phi &= \mathbf{X}^{-1}\mathbf{Y} \\ &= (\mathbf{C}\mathbf{X}_{reg})^{-1}(\mathbf{C}\mathbf{Y}_{reg}) \\ &= \mathbf{X}_{reg}^{-1}\mathbf{C}^{-1}\mathbf{C}\mathbf{Y}_{reg} = \mathbf{X}_{reg}^{-1}\mathbf{Y}_{reg} \\ \Phi &= \Phi_{reg} \end{aligned} \quad (2.55)$$

According to 2.55, the equality of observed and regional phase tensor proves the indifference of galvanic distortion, under the condition \mathbf{C} only contains effects that are purely galvanic and not magnetic (Chave and Jones, 2012). The Φ is

$$\begin{bmatrix} \Phi_{11} & \Phi_{12} \\ \Phi_{21} & \Phi_{22} \end{bmatrix} = \frac{1}{\det(\mathbf{X})} \begin{bmatrix} X_{22}Y_{11} - X_{12}Y_{21} & X_{22}Y_{12} - X_{12}Y_{22} \\ X_{11}Y_{21} - X_{21}Y_{11} & X_{11}Y_{22} - X_{21}Y_{12} \end{bmatrix} \quad (2.56)$$

where $\det(\mathbf{X})$ is the determinant of the \mathbf{X} . Phase tensor can be described by a representative ellipse (Figure 2.6) in which its dimensional properties are determined by

invariants derived from phase tensor components.

$$\Pi_1 = tr(\Phi)/2 \quad (2.57)$$

$$\Pi_2 = [det(\Phi)]^{(1/2)} \quad (2.58)$$

$$\Pi_3 = sk(\Phi/2) \quad (2.59)$$

where $tr(\Phi) = \Phi_{11} + \Phi_{22}$, $sk(\Phi) = \Phi_{12} - \Phi_{21}$ and the determinant $det(\Phi) = \Phi_{11}\Phi_{22} - \Phi_{12}\Phi_{21}$. Then, the main four invariants that defines the ellipse are

$$\Phi_{min} = (\Pi_1^2 + \Pi_3^2)^{1/2} - (\Pi_1^2 + \Pi_3^2 - \Pi_2^2)^{1/2} \quad (2.60)$$

$$\Phi_{max} = (\Pi_1^2 + \Pi_3^2)^{1/2} + (\Pi_1^2 + \Pi_3^2 - \Pi_2^2)^{1/2} \quad (2.61)$$

$$\beta = \frac{1}{2}tan^{-1}\left(\frac{\Phi_{12} - \Phi_{21}}{\Phi_{11} + \Phi_{22}}\right) \quad (2.62)$$

$$\alpha = \frac{1}{2}tan^{-1}\left(\frac{\Phi_{12} + \Phi_{21}}{\Phi_{11} - \Phi_{22}}\right) \quad (2.63)$$

and Φ can be written in the form of a singular value decomposition, using these invariants.

$$\Phi = \mathbf{R}^T(\alpha - \beta) \begin{bmatrix} \Phi_{max} & 0 \\ 0 & \Phi_{min} \end{bmatrix} \mathbf{R}(\alpha + \beta) \quad (2.64)$$

Equation 2.64 basically states that in a case where a rotation of $\alpha - \beta$ is succeeded, phase tensor may take diagonal form and it shows properties of a 2-D environment, thus rotated to the regional strike angle. Singular values Φ_{min} and Φ_{max} are the principle phase angles and their magnitudes define the length of the ellipse's semi-axes. In ideal 1-D and 2-D environments, phase tensors become

$$\begin{aligned} \Phi_{1D} &= \begin{bmatrix} \Phi_{11} & 0 \\ 0 & \Phi_{11} \end{bmatrix} = \Phi_{11}\mathbf{I} = \frac{Y_{11}}{X_{11}} = tan(\phi) \\ \Phi_{2D} &= \begin{bmatrix} \Phi_{11} & 0 \\ 0 & \Phi_{22} \end{bmatrix} \end{aligned} \quad (2.65)$$

It is important to notice that remaining components Φ_{11} and Φ_{22} do not have any contribution from Z_{xx} or Z_{yy} . This is the ideal descriptive 2-D environment for phase tensors and the regional strike angle should be equal only to the α angle, in other words β must be zero. In fact, any deviation from zero-point β is representative of a 3-D conductivity structure. However in practice, variations below 3° can be accepted as a 2-D environment (Caldwell et al, 2004; Booker, 2013). Basic concepts of the phase tensor and its invariants are illustrated in Figure 2.6 with a representative ellipse (Caldwell et al., 2004).

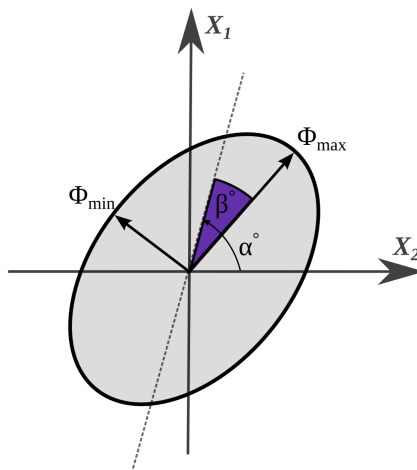


Figure 2.5. Schematic representation of a phase tensor ellipse and its invariants β , α , Φ_{min} and Φ_{max} , where x_1 and x_2 are the coordinate reference frame.

Phase tensor ellipses basically show the strike orientation along the Φ_{max} semi-axes. In an isotropic homogeneous media, these ellipses take form of a circle and β is equal to zero. As the media starts to have 2-D or 3-D conductivity distribution, ellipses start to elongate towards the strike orientation. In cases where $\det(\Phi) < 0$ (i.e. a singular-case phase tensor) and $\Phi_{min} = 0$, ellipse is represented by a single principle axes thus a straight line with a magnitude of $2\Phi_{max}$. An unusual 3-D effect may occur when both $\det(\Phi)$ and Φ_{min} are negative. As this 3-D effect strengthens, a re-expanding ellipse is drawn to portray this case (Caldwell et al., 2004).

2.7. MT Modeling

Geophysical methods are often need a modeling step to approximate the geological structure of the sub-surface depending on some accurate spatial attributes. A model of the sub-surface can be sought by designing forward responses or inversion schemes. A forward problem is defined by selecting model parameters (\mathbf{m}) to approximate the data (\mathbf{d}) with the accurate physical framework.

$$\mathbf{D}_p = \mathbf{F}[\mathbf{m}] \quad (2.66)$$

where \mathbf{D}_p is the calculated response and $\mathbf{F}[\mathbf{m}]$ is the non-linear forward operator. Forward operators are numerical solvers that use methods such as finite-differences, finite-elements or integral equations. It is fairly difficult to mimic the Earth's sub-surface due to complexity of the medium, thus design of an inversion scheme is often required (Zhdanov, 2002). An inversion scheme is basically described as the tool that approximates an earth model by minimizing the difference between response of the data and model parameters (penalty functional, φ).

$$\varphi(\mathbf{d}, \mathbf{m}) = \mathbf{d} - \mathbf{F}[\mathbf{m}] \quad (2.67)$$

$$\mathbf{m} = [m_1, m_2, \dots, m_M]^T \quad (2.68)$$

$$\mathbf{d} = [d_1, d_2, \dots, d_N]^T \quad (2.69)$$

where T denotes to transpose, \mathbf{d} and \mathbf{m} are the N-length data space and M-length model space. The matrix form of this equation is:

$$\varphi(\mathbf{d}, \mathbf{m}) = \begin{bmatrix} d_1 \\ d_2 \\ \vdots \\ d_N \end{bmatrix} - [\mathbf{F}] \begin{bmatrix} m_1 \\ m_2 \\ \vdots \\ m_M \end{bmatrix} \quad (2.70)$$

Hadamard (1902) explained that most physical problems in nature are ill-posed, in other words they do not have a unique solution. Regularized inversion schemes were developed out of the necessity to create solutions for such problems. According to Tikhonov and Arsenin (1977), a non-unique solution for an ill-posed problem may exist in the form:

$$\tau(\mathbf{d}, \mathbf{m}) = \|\mathbf{d} - \mathbf{F}(\mathbf{m})\|^2 + \nu \|\mathbf{\Upsilon} \mathbf{m}\|^2 \quad (2.71)$$

where ν is the regularization parameter that controls the trade-off factor between the data misfit ($\|\mathbf{d} - \mathbf{F}(\mathbf{m})\|^2$) and *a priori* information ($\|\mathbf{\Upsilon} \mathbf{m}\|^2$). $\mathbf{\Upsilon}$ is the Tikhonov matrix that could be replaced with any kind of linear operator. In this study, ModEM algorithm (Kelbert et al., 2014) was implemented to create 3-D models with MT data. For this algorithm, penalty functional (τ) is expressed in form:

$$\begin{aligned} \tau(\mathbf{m}, \mathbf{d}) = & (\mathbf{d} - \mathbf{F}(\mathbf{m}))^T \mathbf{C}_d^{-1} (\mathbf{d} - \mathbf{F}(\mathbf{m})) \\ & + \nu (\mathbf{m} - \mathbf{m}_0)^T \mathbf{C}_m^{-1} (\mathbf{m} - \mathbf{m}_0) \end{aligned} \quad (2.72)$$

where \mathbf{C}_d is the covariance of the data errors, \mathbf{m}_0 is the prior values for the model parameters and \mathbf{C}_m (or more properly $\nu^{-1} \mathbf{C}_m$) is the model covariance or regularization

term.

The most conventional way of minimizing the penalty functional τ is the application of a Newton-type iteration scheme in model space. This type of minimization problems need the calculation of $N \times M$ sensitivity matrix $\mathbf{J}_a = \frac{\partial \mathbf{F}}{\partial \mathbf{m}}$ and $M \times M$ Hessian matrix $\mathbf{H}_m = \frac{\partial^2 \varphi}{\partial m^2}$, which have to be stored in memory throughout all iterations. The classical Gauss-Newton solution for the minimization problem of 2.72 is:

$$(\mathbf{J}_m^T \mathbf{J}_m + \nu \mathbf{I})(\mathbf{m}_{n+1} - \mathbf{m}_n) = \mathbf{J}_m^T \mathbf{r} - \nu \mathbf{m}_n \quad (2.73)$$

where \mathbf{m}_n is the model parameters at the n^{th} iteration and this problem can be solved iteratively for \mathbf{m}_{n+1} . With the current computational capabilities, 1- and 2-D approximations can be easily handled in this manner, however much larger size of 3-D data inhibits the efficiency of such methods both in computing time and required memory (Avdeev, 2005). Siripunvaraporn et al. (2005a) introduced the data-space approach for 3-D MT problem. Their code uses the data-space Occam approach, which seeks the smoothest and most conservative model by minimizing the penalty functional with respect to regularization parameter. By applying the Occam scheme, 2.73 can be written as,

$$(\mathbf{J}^T \mathbf{J} + \nu \mathbf{I})(\mathbf{m}_{n+1} - \mathbf{m}_n) = \mathbf{J}^T \bar{\mathbf{d}} \quad (2.74)$$

where $\bar{\mathbf{d}} = \mathbf{d} - \mathbf{F}(\mathbf{m}_n) + \mathbf{J}\mathbf{m}_n$. Converting the inversion scheme to data space reduces the matrix dimensions from $M \times M$ to $N \times N$ where $N \ll M$ and produces the same results as model-space approach if the same model parameters were used. However, this approach still takes quite a long time for a moderately selected data and model space to completely converge on a single-processor computer.

An efficient alternative to Newton-type methods is the non-linear conjugate gradients (NLCG) method. Rodi and Mackie (2001) have successfully applied the NLCG algorithm for 2-D MT problem, which is extensively preferred due to computational ad-

vantages in solving large-scale inverse problems. Newton-type methods seek solutions for the minimization of penalty functional through linearised least-squares approach. NLCG method does not work in this sense and directly solves the minimization problems that are not quadratic (Rodi and Mackie, 2001). A solution is sought in minimizing the gradient of the penalty functional with respect to model parameters by searching directions with the steepest descent on model space (Egbert and Kelbert, 2012). NLCG algorithm only computes the sensitivity matrix for once at the beginning. This property of NLCG inherently reduces the computational time and required memory load that is necessary for MT inversion (Egbert and Kelbert, 2012).

3. GEOLOGY AND TECTONICS

In order to create a meaningful picture of the geological state of a region, one should handle the existing concepts with a holistic approach which should cover the elaborative story of not only the study area but the whole surrounding region and relative global tectonics. In this thesis, a large array of studies were considered to made comparisons both with each other and with the current MT data analyses and models.

3.1. Evolutionary Tectonics of Anatolia and Tethyan Oceans

Anatolia is a tectonic plate situated at the center of the collision between African, Arabian and Eurasian plates. It is made up of several continental fragments joined together in late Tertiary (Okay, 2008c). Evolution of these continental fragments is directly related with the closure of the ocean called Tethys, which has existed between old continents Laurasia and Gondwana throughout most of the Phanerozoic (Figure 3.1). Its closure is not printed over Anatolia as the subduction of a single continuous oceanic plate, but an intercalation of different type of arc mechanisms and buoyant exotic continental blocks rifted from distant sides of the continents (Şengör, 1987). Evolution of Tethys oceans near Anatolia have invoked debates for the last 50 years. One of the most argued subjects have mainly developed around the Permo-Triassic state of the Tethys oceans. Implications were about the locally metamorphosed unit called Karakaya Complex, which is distributed all around the Sakarya Continent constituting a Hercynian and Kimmeridgian basement for the Mesozoic cover (Okay and Göncüoğlu, 2004). Existence of this unit have been interpreted as an indicator of the Paleozoic-Mesozoic aged ocean called Paleo-Tethys (Figure 3.1).

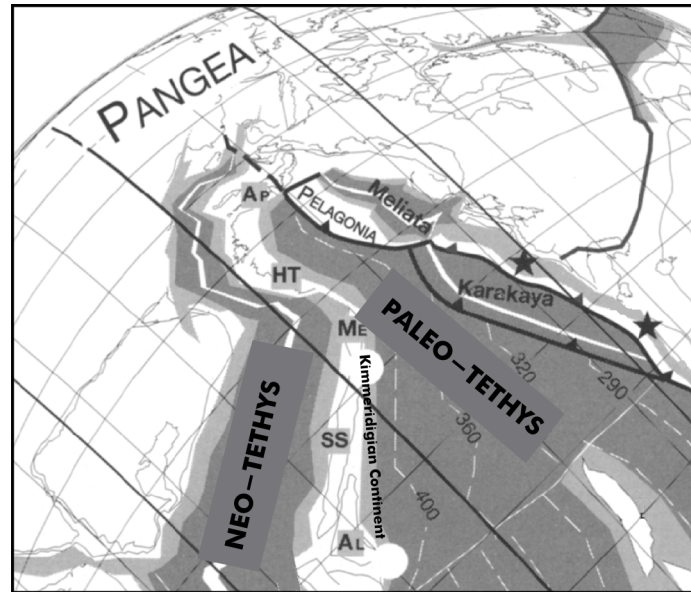


Figure 3.1. Paleogeographic sketch map at ca. 248 Ma (Triassic) showing the state of the Tethyan Oceans. Modified after Stampfli (2000). Ap: Apulia, HT: Hellenides-western Taurides externides, Me: Menderes-Taurus Block, Ss: Sanandaj-Sirjan Block, Al: Albortz.

Tectonic units of the Eastern-Mediterranean and Anatolia are constructed around the idea of Tethyside sutures. Accreted remnants (ophiolites and melanges) of the Tethys oceans allowed researchers to make distinctions between paleotectonic units of Anatolia. In particular, Neo-Tethyan Ophiolitic Melanges found in Anatolia, draws the closure of Neo-Tethyan Ocean near İAES (Figure 3.2) (Okay and Tüysüz, 1999). Rhodope-Strandja, İstanbul and Sakarya terranes, which are collectively called as Pontides; The Anatolid-Taurides, Kırşehir Block and Arabian Platform are blocks all separated from Gondwana. Although they all have the same Cadomian/Pan-African crystalline basement, Pontides and the southern units have never been contiguous and rifted-off from Gondwana at different geological times from distinct spatial positions (Okay et al., 2008b). This is the first evolutionary model for the development of Karakaya Complex. It describes the Permo-Triassic Karakaya Unit as an accretionary remnant of a northwardly-subducting Paleo-Tethyan Block (Okay and Göncüoğlu, 2004). The second model suggest that, Karakaya Complex represents a short-lived marginal ocean developed due to rifting that occurred at Permo-Triassic times (Şengör

and Yılmaz, 1981). Today, the overall consensus and the data are in favor of the first model. The separation between Pontides and Anatolian units are marked by the Neo-Tethyan Ophiolitic Melanges and accretionary complexes which can be seen all along the İzmir-Ankara-Erzincan Suture (IAES) (Figure 3.2) (Okay and Tüysüz, 1999). Within the Cenozoic framework, Pontides are considered as a part of Eurasia and most of it exist within the borders of Alpide Collision Zone.

3.2. Active Tectonics of Anatolia and North Anatolian Fault

Movement of the Anatolian Plate with respect to Eurasia is constrained by the strike-slip mechanisms of dextral North Anatolian Fault (NAF), sinistral East Anatolian Fault (EAF) and subduction roll-back mechanism of the Hellenic Subduction Zone (HSZ). Calculated slip motion of Anatolian Plate near the NAF is 24 ± 1 mm/yr and 9 ± 1 mm/yr for the EAF, while Aegean/Peloponnisos move towards south-west with the velocity of 30 ± 2 mm/yr (McClusky et al., 2000). By using these boundaries, roughly rigid Anatolian Plate makes a counter-clockwise rotation around northern Egypt, resulting in escape tectonics during Plio-Quaternary times (McKenzie, 1972; McClusky et al., 2000) with an average geodetic rate of 25 mm/yr (Reilinger et al., 2006). As a conclusion of escape tectonics, Anatolian Plate shows characteristics of westerly widening extension moving from Karlıova Junction to western Anatolia. Although the initiation of these boundaries are considered as early-Miocene, N-S extension and westward escape tectonics of the Anatolian Region started prior to Miocene collision of the Arabian Plate, where several evidences are indicated with mechanisms developed between Late Cretaceous and Miocene (Jolivet, 2001; Okay et al. 2008a, Cavazza et al., 2009). This situation suggests that the main driving force behind the escape motion was actually the slab suction of the HSZ rather than the Arabian-Eurasian Collision (Reilinger et al., 2006).

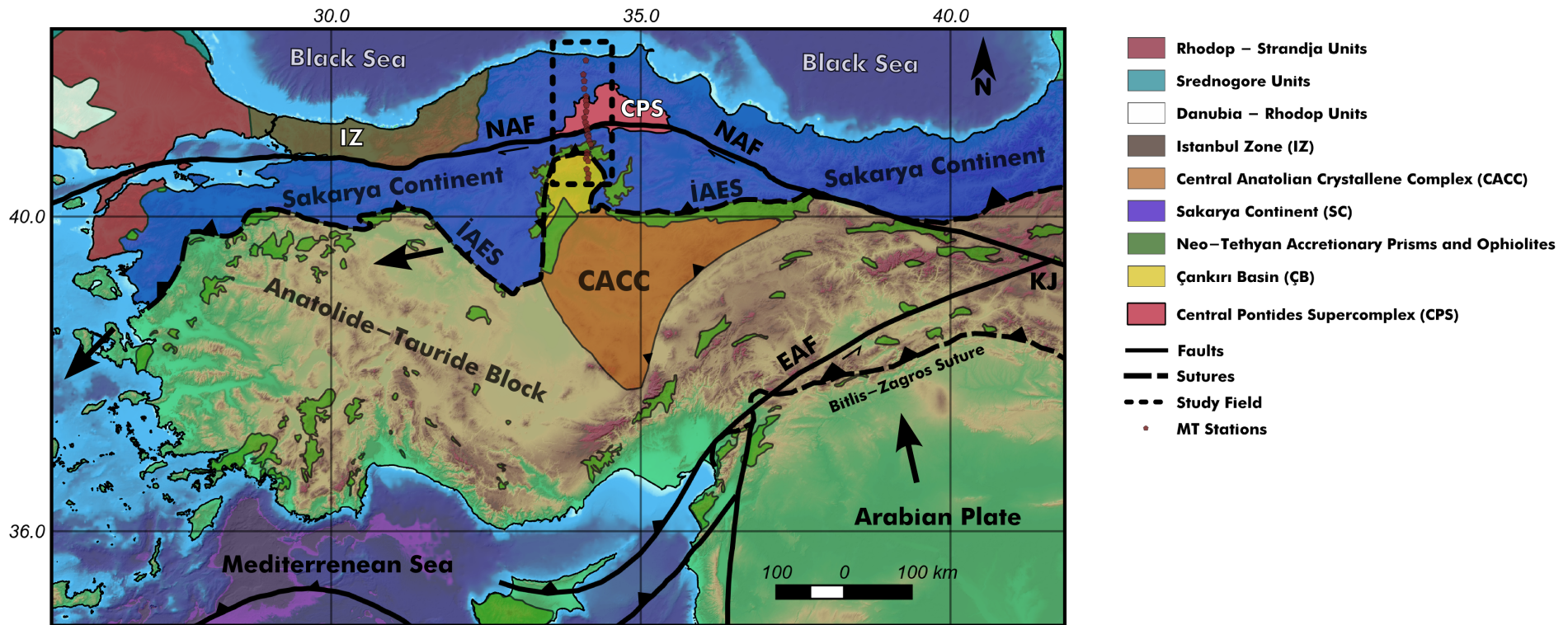


Figure 3.2. Tectonic units of Turkey are plotted alongside with the Neo-Tethyan Ophiolitic Melanges, modified after Okay et al. (1999), Advokaat et al. (2014). CACC: Central Anatolian Crystalline Complex, EAF: East Anatolian Fault, İAES: İzmir-Ankara-Erzincan Suture Zone, İZ: İstanbul Zone, KJ: Karlıova Junction, NAF: North Anatolian Fault.

Subduction of the African Plate through Cypriot Arc is also another important driving force for the evolution of the many major geological features especially for the Central Anatolian Volcanic Province and Alpide Orogeny of the Tauride Mountains (Whitney et al., 2007). To the east of Karlıova Junction, Eastern Anatolian Plateau represents a post-collisional fore-arc platform of Neo-Tethyan Subduction through Bitlis-Pötürge Massif, where wide-spread volcanism and extension are observable throughout the region (Şengör et al., 2003). Geophysical data suggest that Eastern Anatolian-Iranian High Plateau do not possess a mantle lithosphere (Al-Lazki et al., 2003; Zor et al., 2003; Türkoğlu et al., 2008).

3.3. Neotectonics of Anatolia

Anatolia is a well-known place within the geoscience community for its rich geological variety and intense seismic activity especially concentrated on NAF, EAF and related structures. After the 1939 Erzincan Earthquake ($M_s = 7.8$), a rapid series of westwardly migrating earthquake succession have occurred just in a five year time-interval (Figure 3.3a) (Niksar-Erbaa ($M_s = 7.1$), 1942; Ladik, 1943 ($M_s = 7.3$); Bolu-Gerede, 1944 ($M_s = 7.4$)). It was Ketin (1948) to firstly notice that the right-lateral motion is the common characteristic for all of these earthquakes. Accordingly, he interpreted correctly the fact that whole of the NAF is actually a major strike-slip zone. Over the last century, especially after the hazardous 1999 İzmit Earthquake ($M_s = 7.6$), a large number of studies have been carried out on the NAF with numerous disciplines to create a better understanding of the mechanics behind it.

Today, the NAF is known as a 1200-km-long dextral strike-slip fault zone that starts from Karlıova Junction, lies along to the Black Sea coast until it divides into several branches near İzmit. Seismicity is known to be periodical with centennial cycles and travels from east to west as stated before. Historical earthquakes also show this migrating characteristic of 1939 to recent succession (Ambraseys and Finkel, 1995; Parsons et al., 2000), but their reliability is questionable before the 17th century (Şengör et al., 2005). The progressive failure of the fault segments along the NAF is partly explained by Coulomb stress transfer along the fault-axis to the next locked

fault segment (Stein and Barka, 1997). Age of the NAF is approximated to be 13 Ma in the east and 5 Ma in the west (Hubert-Ferrari et al., 2002). Average slip motion for the last few thousand years calculated from ^{14}C dating of stream terrace offsets are found to be $18 \pm 5 \text{ mm/yr}$ (Hubert-Ferrari et al., 2002). This is comparable within the error range of present-day slip motion $22 \pm 3 \text{ mm/yr}$ estimated from rigid block modeling of GPS data (Reilinger et al., 2006). The total offset of the NAF is estimated to be $80 \pm 15 \text{ km}$ along the Tosya and Vezirköprü basins (Hubert-Ferrari et al., 2002).

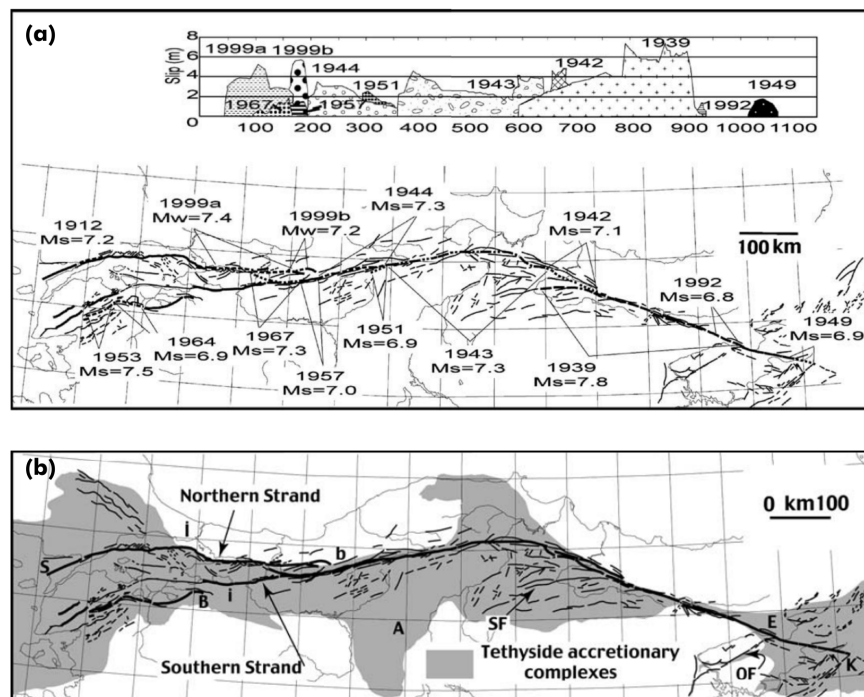


Figure 3.3. (a) Map representing the earthquake succession at NAF occurred in the last century. (b) Distribution of Tethyside accretionary complexes around Anatolia.

Taken from (Şengör et al., 2005).

Seismicity along the NAF naturally does not show homogeneous characteristics due to complex geology and geodynamical state of Anatolia. Many segments can be stated as seismic gaps (Toksöz et al., 1979; Ergintav et al., 2014), while the surface creep (Çakır et al., 2005) or microseismic activity (Bulut et al., 2009) are also valid explanations for stress release on some segments. The NAF is in possession of many subsidiary structures related to variational shear related extension-compression dis-

tribution throughout the zone, which can be named as North Anatolian Shear Zone (NASZ). Collectively, NAF and NASZ are called North Anatolian Keirogen (NAK) (Şengör et al., 2005). It is an important observation to point out that NAK almost exclusively remains in the Tethyside accretionary complexes distributed around İAESZ (Figure 3.3b). Accordingly, it is not hard to interpret that Neogene formation of NAK most probably followed the preceding weakness areas of these Tethyside accretionary complexes (Şengör et al., 2005). Traveling from east to west, NASZ exhibits overall widening characteristic similar to N-S oriented spatial-span of Tethyside accretionary complexes, if one excludes the Ilgaz and Ankara Lobes, which do not hold seismically active structures relative to the other areas of NAK. Tokat Lobe is an exception, however the seismicity is mostly concentrated on the northern side of the lobe and the southern structures seems to be relatively quiescent.

3.4. Geology and Tectonics of Central Pontides

Pontides are a mountain chain that were episodically created and deformed by the Variscan (Hercynian), Kimmeridgian and Alpidic orogenic events (Okay et al., 2017). During Phanerozoic, they have been built up as a tectonic unit, which in conclusion were amalgamated onto Laurasian/Eurasian Continent as an active margin. On a global scale, these orogenic events are made up by heterochronous collisions of smaller microplates, intra-oceanic arc blocks and their accretionary residues. This situation makes the paleogeographical reconstructions of the region drastically more difficult to handle in comparison with the more stable areas like cratons. Pontides, which are delimited by the Black Sea from the north and İzmir-Ankara-Erzincan Suture from the south, are perfect examples of crustal growth caused by successive subduction-accretion mechanisms; and their evolution have been a key part in constructing the geological history of the Tethyan Realm (Okay et al., 2006). Geological map of the area can be seen in Figure 3.4.

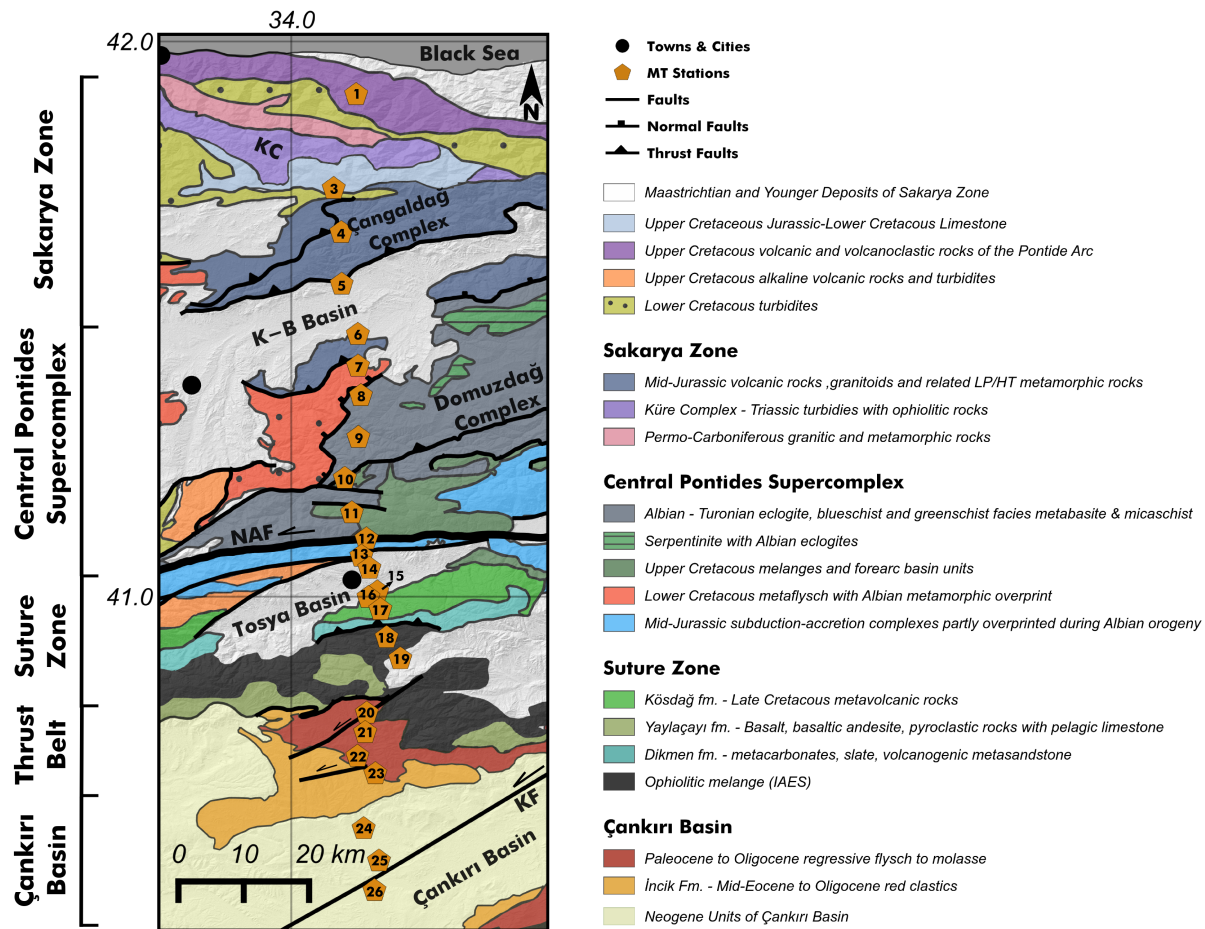


Figure 3.4. Geological map of the study area with the MT stations. Geological map was modified after Okay et al. (2013), Aygül et al. (2015), Kaymakçı et al. (2009). K-B: Kastamonu Boyabat, KF: Kızılırmak Fault

Central Pontides (CP) are the geographical term that describes the northwardly bended section of the Pontic Orogenic Belt and related tectonic structures. They consist of two distinct geological terranes: İstanbul and Sakarya. Although they are juxtaposed to each other, they were developed within different tectonic frameworks and do not share the same lithological timeline. Existence of the shallow marine İnaltı Formation that covers both tectonic units prove the amalgamation that took place in at least as early as Late Jurassic (Okay et al., 2013; 2017). Paleozoic - Mesozoic sequence of the İstanbul Zone shows similar characteristics to that of Moesian Platform which is a part of Eurasian Continent; while the basement of Sakarya Zone in CP were made up of Permo-Carboniferous granites and Triassic or older subduction-accretion complexes.

It is mostly accepted that western Black Sea started to open as a back-arc basin simultaneously with the subduction of the Neo-Tethyan lithosphere along IAES in Cretaceous (Hippolyte et al., 2016, Tüysüz, 1999). However, tectonic environment in the area does not solely stems from Neo-Tethyan convergence but also Paleo-Tethyan convergence which are co-existed in Cretaceous. Most of the CP is made up of large metamorphic bodies. The northernmost one is the Küre Complex and this unit shows similar affinities with the Upper-Karakaya Complex which can be seen in the western Sakarya Zone in Turkey (Okay et al., 2013). This unit is juxtaposed with Permo-Carboniferous granites, which collectively made up the continental basement of Central Pontides of Sakarya Zone. In terms of their ages, there is a clear distinction between Küre Complex and the southern metamorphic units, Domuzdağ and Çangaldağ complexes, all together known as Central Pontides Supercomplex (CPS) (Okay et al., 2013). Previously, metamorphic units that make up CPS were not aged properly and considered as a remnant of the subduction that was occurred within the same environment where Küre Complex was amalgamated onto Laurasian active margin in Permo-Triassic ages. However, the latest isotopic data showed that the events that have been responsible for the development of CPS actually occurred between Late Jurassic to Late-Cretaceous (Okay et al., 2006; 2013; 2017; Aygül et al., 2015; 2016). Metamorphic print over these units and the way of emplacement of the Çağlayan Turbidite Sequence over them are suggestive of several episodes of extension or shortening related to the subduction

environment and development of the fore- and back-arc basins that surrounds them (Okay et al., 2013). Today, these units of CPS are in contact with each other with north-dipping thrust faults and made up the Eurasian front of Anatolian collision in CP.

Northernmost unit of the CPS is the Çangaldağ Complex. The unit has two outcrops at the both side of the Tertiary aged Kastamonu Basin. Çangaldağ Complex consists of volcano-clastic and fine-grained clastic rocks metamorphosed in regional low-grade greenschist facies. Units are cut by mid-Jurassic granitic intrusions, which put a reliable constrain on the age of this unit (Okay et al., 2006). Geochemical analyses of the volcanic units in this section are in favor of a model claiming that Çangaldağ Complex is developed as an ensimatic volcanic arc (Ustaömer and Robertson, 1999). Along our MT profile, at the south of the Çangaldağ Complex, Esenler Unit is present which is made up of flysch and lesser amounts of metabasite, marble and serpentinite lenses metamorphosed in blueschist facies. Presence of blueschist within the turbiditic material in Esenler Unit suggests that this unit was developed in an accretionary trench environment of the Laurasian active continental margin. On the southern side, the unit is in contact with Domuzdağ Complex through a low-angle detachment fault overprinted by the strike-slip motion of Post-Miocene tectonic environment (Aygül et al., 2016). Domuzdağ Complex is a large metamorphic body metamorphosed in blueschist to eclogite facies. It represents another episode of subduction-accretion process existed within the Paleo-Tethyan Ocean (Okay et al., 2006). Domuzdağ Complex exhumed through using the Acisu Fault in the Late Cretaceous (Okay et al., 2006). The unit is underlain by a large E-W elongated ophiolitic melange unit named as Kirazbaşı Formation. This formation deposited during Turonian-Coniacian prior to accretion of exotic terraneous block of Kargı Microcontinent (Okay et al., 2013). In a classically progressive setting of a subduction-accretionary model, units have to appear younger closer to active margin. However, recurring and non-linearly timed ages of metamorphism and emplacement of the CPS units point out active tectonic climate, which infers to a rather complex kinematic history (Okay et al., 2006; 2013). Evolution of the accretion and the deformation history related to the Cretaceous tectonic climate are summarized in the sketch of Okay et al. 2013 (Figure 3.5).

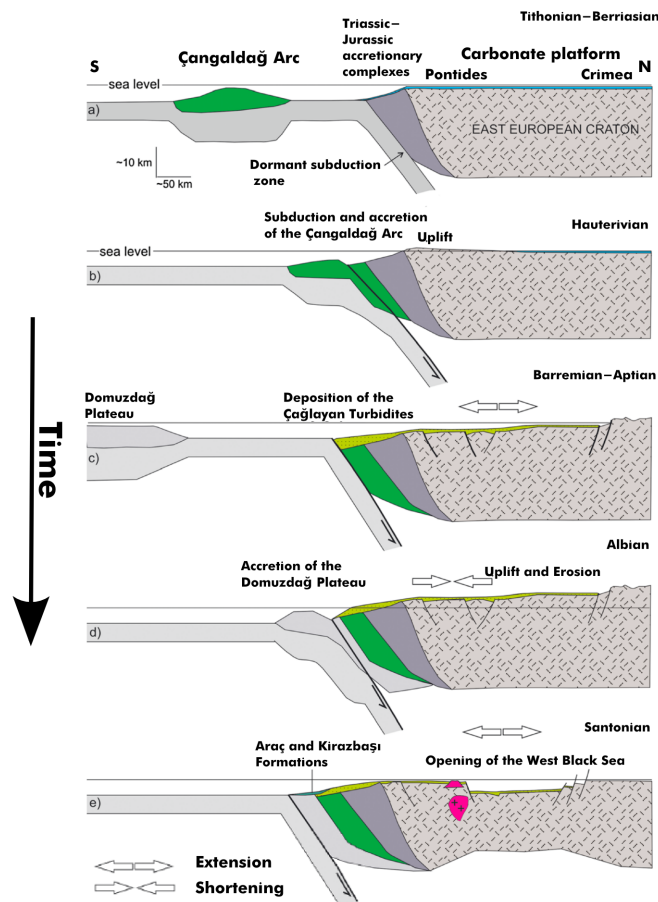


Figure 3.5. Schematic representation of the Cretaceous evolution of the Eurasian margin in Central Pontides; taken from Okay et al. (2013).

To the south of Paleo-Tethyan Metamorphic Sole, a zone made up of arc sequences appears. Northernmost one of these units is called the Köşdağ Formation, which is represented by mafic and felsic low-grade meta-volcanic rocks interbedded with micritic limestones developed prior to subduction of main closure of Neo-Tethys along IAES (Aygül et al., 2015). Köşdağ Formation is overlain by meta-sedimentary rocks of the Dikmen Formation in the south. Existence of radiolaria in Dikmen Formation suggests that this unit was developed in a deep marine environment and the arc did not end with the collision of Kırşehir Block (Aygül et al., 2015). Age of the arc is determined to be Cenomanian-Turonian. The whole sequence was thrust by ophiolitic melanges, which forced the Köşdağ Arc units to become structurally positioned as a steeply

dipping anticline. Moving further southwards, another volcano-clastic unit Yaylaçayı Formation was situated with a younger geologic age of Upper-Cretaceous. Geochemical analyses of Köşdağ Arc suggests; it was developed in a supra-subduction environment, which was later terminated due to roll-back of Neo-Tethyan Oceanic Lithosphere (Aygül et al., 2015). All of the units described above were amalgamated into each other before the collision of the Kırşehir Block. A schematic diagram illustrates the evolution of supra-subduction environment in Figure 3.6.

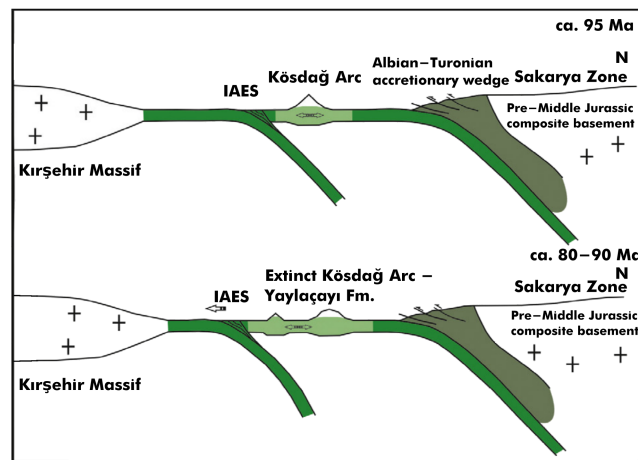


Figure 3.6. Schematic diagram of the evolution of supra-subduction zone developed prior to Neo-Tethyan Collision, modified from Aygül et al. (2015).

South of the İAES, there lies a large Tertiary sedimentary basin surrounded by Neo-Tethyan Ophiolitic Melanges (NTOM). The thick sequence consists of continuous sedimentation since Upper-Cretaceous, making the basin significant in understanding the evolution of Neo-Tethyan realm in Turkey. Five cycles of sedimentation processes were reported in the basin (Kaymakçı et al., 2010). Oldest one consists of Yapraklı Formation, which is made up of volcano-clastic rocks and regressive shallow marine sequences, respectively. Together with NTOM, they make up the basement of the Çankırı Basin. In an exploration well, NTOM was found at a depth of 3566 m (Kaymakçı et al., 2009). The first cycle of units were overlain by Paleocene to Eocene regressive flysch to molasse sequence and continued by Middle-Eocene to Oligocene continental red clastics named as İncik Formation. The first and second cycles were

structured with many thrust faults in between. Moving away to the center of Çankırı Basin, Neogene fluvial and lacustrine based flat-lying sediments appear. Basin is cut through with three major dextral fault systems: Yoncalı Fault at the northern rim of the basin, Kızılırmak Fault at the center of the basin and Ezinepazarı - Sungurlu Fault at the southern side of the basin (Kaymakçı et al., 2010).

The contractional development of Çankırı Basin took place coevally with the northern Neo-Tethyan Fore-arc Basin, Sinop Range (Espurt et al., 2014). Our MT data do not cover this area, but the geological implications derived from here are important in understanding the geodynamical evolution of Black Sea and all of the Pontic Terrane. Sinop Basin was firstly developed as a fore-arc basin beneath the Late-Cretaceous aged Pontide Arc. The extension of the basin took place from Late-Cretaceous to Paleocene assisted by Neo-Tethyan slab retreat (Espurt et al, 2014). The slab retreat was evidenced in the region by the ultrapotassic magmatic rocks found in the proximity of CPS borders, which infer to southward progression of the slab in Late-Cretaceous (Gülmez et al., 2016). After Eocene, tectonic inversion of the extensional regime took place (Espurt et al., 2014), which resulted in 33 % crustal shortening and ductile thickening in the area between the two strong mechanical units of CPS and Black Sea Basin (Espurt et al., 2014).

3.5. Seismicity on Central Pontides

Even though it is relatively quiescent compared to the other seismically active regions of Anatolia, CP are prone to earthquake hazard too like most of Turkey. During the rapid earthquake succession in 20th century, the NAF produced four major earthquakes (1942 Erbaa-Niksar Earthquake, M_w : 6.8; 1943 Tosya Earthquake, M_w : 7.4; 1944 Gerede Earthquake and 1951 Kurşunlu Earthquake, M_w : 6.9) in the region. The right-lateral motion of the NAF and related structures are dominant sources of seismicity in the region, where distinct segments naturally display different mechanical characteristics. West of our study area, Kurşunlu Segment exhibits shallow creep motion, which is still presumably locked in seismogenic depths and have produced large earthquakes in historical period (Çakır et al., 2005). The particular segment that our

study placed on is 275 km long (Wesnousky, 2006) and ruptured with five large earthquakes during the last 2000 years, one of them is being the 1943 Tosya Earthquake (Hartleb et al., 2003). The most notable characteristics of this segment are: (1) 30° change in strike direction within the fault trace and (2) possession of secondary splay fault systems, which are named as Ezinepazarı-Sungurlu, Merzifon and Laçın faults (Hubert-Ferrari et al., 2002). Earthquakes in this region have more occurrence rate on these splays rather than the main strand of NAF (Yolsal-Çevikbilen et al., 2012). The sense of deformation acquired from focal mechanisms of earthquakes in the central part of the segment appear to have some normal or thrust component (Şengör et al., 2005). Peyret et al. (2012) found that the vertical deformation in the area appears to be significantly lower (2 mm) compared to the dextral movement of NAF and subsidiary fault systems. Beyond the Ekinveren Fault, the thrust bend in Sinop range shows active compressional deformation (Yıldırım et al., 2011).

By developing block tectonic models of the region with the analysis of persistent-scattered InSAR data, Peyret et al. (2012) estimated the locking depth of this segment to be varying between 15 km to 25 km. Earthquake hypocenters of Yolsal-Çevikbilen et al. (2012) are in good agreement with this result. Increase in locking depth occurs within the northernmost points of the convex bend of the NAF between the longitudes of 34.20° and 34.50°. The fact that there is no clear observation of asymmetrical strain distribution around the fault, it could be stated that the NAF is confined within the mechanically symmetric units at depth (Şengör et al., 2005). Earthquakes occurred in the area since 1909 and major tectonic features are depicted in Figure 3.7.

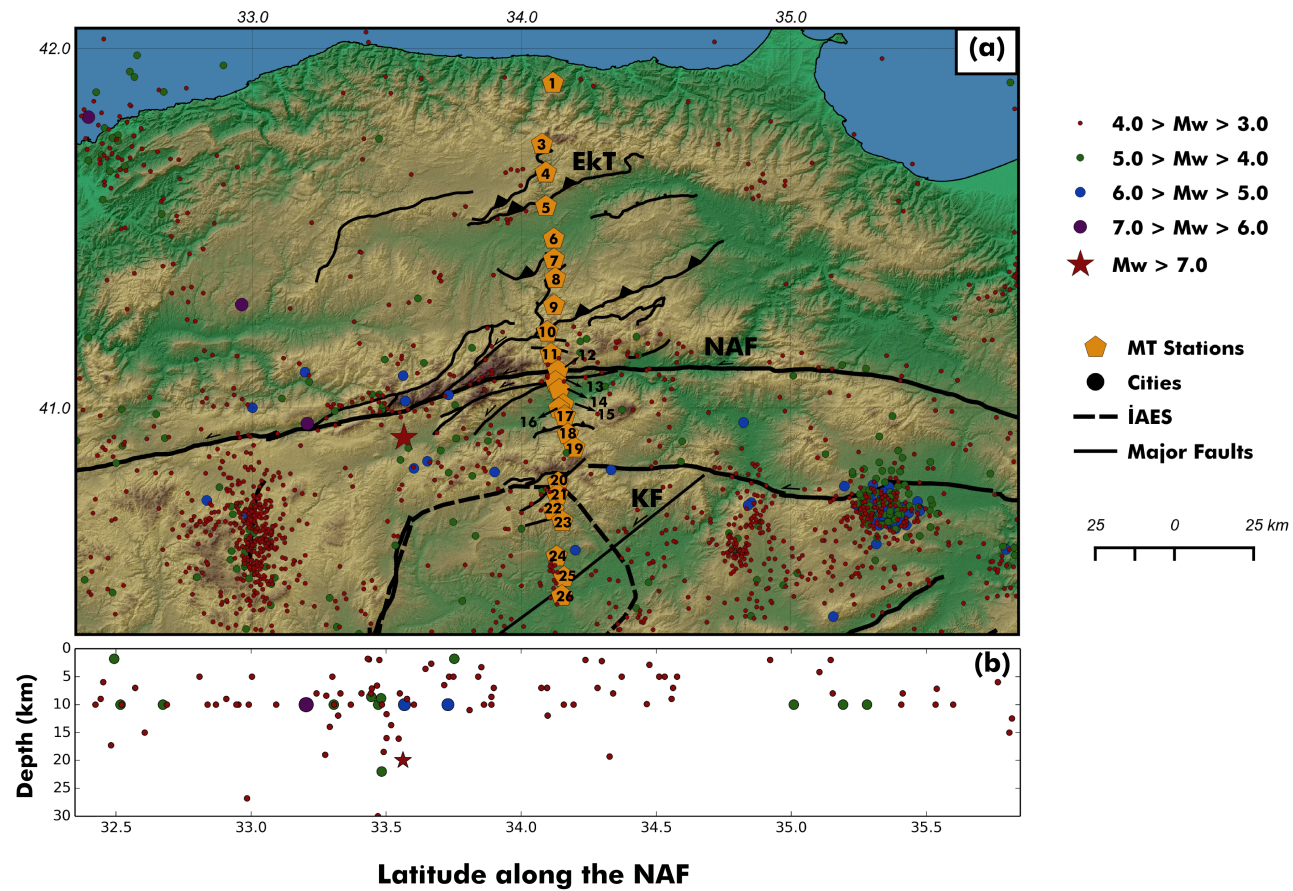


Figure 3.7. (a) Map showing the MT stations, tectonic features, and earthquake hypocenter locations in the area. Yellow pentagons represent the wide-band MT stations, earthquake hypocenters are taken from the ISC catalogue. They are plotted according to their magnitude. (b) A graph representing the earthquakes occurring near the NAF with a proximate distance of 10 km. NAF: North Anatolian Fault, EkT: Ekinveren Thrust, KF: Kızılırmak Fault, İAES: İzmir-Ankara-Erzincan Suture.

4. DATA ACQUISITION AND PROCESSING

4.1. Introduction

This chapter describes the methodologies that have been used during the acquisition and analysis of the MT data. The data were collected during a two field surveys in 2012. The study is a part of NSF funded project Continental Dynamics - Central Anatolian Tectonics (CD-CAT).

4.2. Instrumentation and Field Procedure

In MT surveys, two components of the natural electric field and three components of the magnetic field are recorded simultaneously by a computer system. The instruments of the system are synchronized with the Global Positioning System (GPS). In this study two Phoenix Geophysics (MTU-5A) recording sets were used. Two horizontal components of electric field (E_x and E_y) were received with four non-polarizing $Pb - PbCl_2$ electrodes. By using a sensitive compass, one dipole set of electrodes were placed to align along the geomagnetic north to gather information about N-S component of electric field (E_x), while the other dipole set was placed orthogonally to record E-W component of the electric field (E_y). The spacing between the electrodes for wide-band measurements taken in values between 50 m to 100 m and determined accordingly depending on the circumstances in the survey area. Spacing between the electrodes must be measured in a precise manner, otherwise it would induce inaccurate analysis of the electric fields. Electrodes are planted in a salty muddy mixture to strengthen the electrical contact with the Earth and prevent the loss of moisture. If the moisture level drops significantly in the vicinity of the electrode, drift in measurements can be observed (Chave and Jones, 2013). In order to prevent faulty measurements, electrodes were buried under the ground completely. Another electrode is connected to the recording system for grounding purposes, in case of a high variation in electrical current would damage the recording set.

Magnetic measurements are deployed by the magnetic coils (MTC-50) placed in three directions. In classical MT analysis, vertical component of the geomagnetic field is not a necessary measure. Nevertheless, vertical component of the magnetic field can be used to generate tipper, an essential parameter used in MT studies. Tipper data can be included in modeling scheme to investigate resistivity variation of subsurface, as well as dimensionality information and lateral variations of conductive behavior. Three coils were placed delicately with the assistance of compasses and water gauges to form accurate geomagnetic references. Magnetic coils were buried as deep as possible to decrease the effects of temperature- and wind-assisted noises. A sketch diagram, representative of an MT installation is given in Figure 4.1.

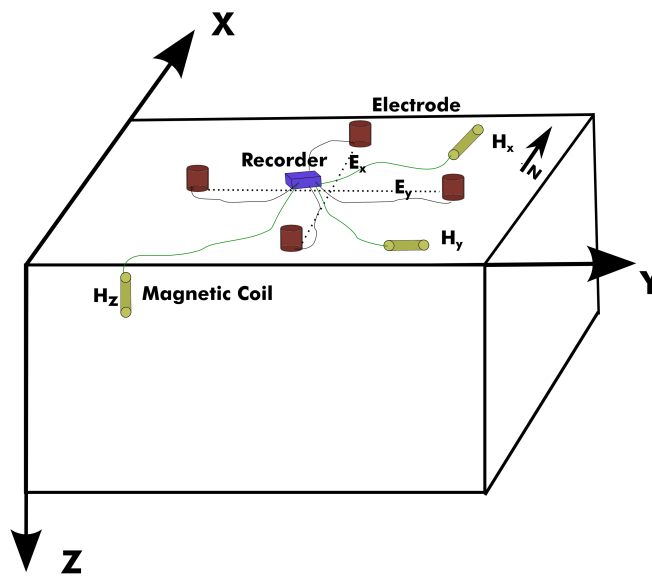


Figure 4.1. Sketch diagram of a MT installation site. Red cylinders are electrodes, yellow cylinders are magnetic coils.

There are many kind of noises, cultural or natural, that could affect electromagnetic fields. To acquire the most reliable measurements, one must perform MT field surveys with the most meticulous manner. Stations are placed to avoid the effects of anthropogenic electric sources like power lines, gas pipelines or water pumps. Wires of the receivers have to be straight and remain as stable as possible. Any loop formation in the wires might trigger noise in magnetic field measurements. Magnetic coils also have to be far away from any kind of moving metal object and from each other. MT measurement devices are depicted in the Figure 4.2.



Figure 4.2. MT equipments, Phoenix Geophysics MTU-5A

4.3. MT Data

In total, 26 MT stations were deployed as a profile to depict the crustal structure in the area (Figure 3.7). Eighteen to forty-two hours of electric and magnetic field recordings were performed at every station. The recorded time window allowed the possibility to obtain data from the wide-band frequency range 320 Hz - 0.00055 Hz (1818 s). The profile passes through Çankırı Basin, İzmir-Ankara-Erzincan Suture, North Anatolian Fault, Domuzdağ and Çangaldağ complexes, Pontide Arc and many other smaller-scale structures. All of the geological entities mentioned above have impact on our data and found to be well-open for interpretation. One of the collected stations were found to be highly affected by noise (CPon 02), thus the processing and modeling steps were carried out only through data of 25 stations.

4.4. Time Series Analysis

MT data were collected as a function of time in five channels (E_x, E_y, H_x, H_y and H_z). Analyses and modeling techniques require the MT data to be in the frequency domain. The first step of the time series analysis is to look at the irregularities at the data that might stem from instrumental error, cultural interference or drastic activity in geomagnetic field. The time-series data converted into frequency domain by applying Fast Fourier transform. In theory, obtained frequency-domain data must confirm the following impedance relations:

$$E_x(\omega) = Z_{xx}(\omega)H_x(\omega) + Z_{xy}(\omega)H_y(\omega) \quad (4.1)$$

$$E_y(\omega) = Z_{yx}(\omega)H_x(\omega) + Z_{yy}(\omega)H_y(\omega) \quad (4.2)$$

By making the assumption that the noise is Gaussian in nature, one can estimate the impedance values by linear least square methods (Simpson and Bahr, 2005). For instance, a least-square solution for n-point data of Z_{xx} and Z_{xy} will be:

$$\Lambda = \sum_{i=1}^n (E_{xi} - Z_{xx}H_{xi} - Z_{xy}H_{yi}) \cdot (E_{xi}^* - Z_{xx}^*H_{xi}^* - Z_{xy}^*H_{yi}^*) \quad (4.3)$$

where * denotes to complex conjugate. Minimizing Λ will give out approximations for the impedance values. Setting derivatives of Z_{xx} and Z_{xy} to zero independently will yield:

$$\sum_{i=1}^n E_{xi}H_{xi}^* = Z_{xx} \sum_{i=1}^n H_{xi}H_{xi}^* + Z_{xy} \sum_{i=1}^n H_{yi}H_{xi}^* \quad (4.4)$$

$$\sum_{i=1}^n E_{xi}H_{yi}^* = Z_{xx} \sum_{i=1}^n H_{xi}H_{yi}^* + Z_{xy} \sum_{i=1}^n H_{yi}H_{yi}^* \quad (4.5)$$

Solving the 4.3 together with 4.4 and 4.5, will minimize the noise of E_x . For every impedance relation, there are six possible least-square solutions that minimize the distinct errors of a electromagnetic field component. Fortunately, these solutions can be solved simultaneously by making power-density estimates. For instance two of the six equations for the solution of Z_{xy} are (Sims et al., 1971):

$$Z_{xy} = \frac{\langle H_x E_x^* \rangle \langle E_x E_y^* \rangle - \langle H_x E_y^* \rangle \langle E_x E_x^* \rangle}{\langle H_x E_x^* \rangle \langle H_y E_y^* \rangle - \langle H_x E_y^* \rangle \langle H_y E_x^* \rangle} \quad (4.6)$$

$$Z_{xy} = \frac{\langle H_x E_x^* \rangle \langle E_x H_y^* \rangle - \langle H_x H_y^* \rangle \langle E_x E_x^* \rangle}{\langle H_x E_x^* \rangle \langle H_y H_y^* \rangle - \langle H_x H_y^* \rangle \langle H_y E_x^* \rangle} \quad (4.7)$$

where $\langle \rangle$ denotes to mean square estimates. While 4.7 tends to result in unstable solutions, 4.6 is a more suitable option for the estimation of Z_{xy} . In fact, for every component of impedance tensor, there are four suitable estimates. Since measured electric and magnetic fields contains measurement errors, 4.1 and 4.2 must have a frequency dependent residual variable $\delta Z(\omega)$ (Simpson and Bahr, 2005)

$$E_x(\omega) = Z_{xx}(\omega)H_x(\omega) + Z_{xy}(\omega)H_y(\omega) + \delta Z(\omega) \quad (4.8)$$

$$E_y(\omega) = Z_{yx}(\omega)H_x(\omega) + Z_{yy}(\omega)H_y(\omega) + \delta Z(\omega) \quad (4.9)$$

An important thing to point out here is that, most of these estimation relations contain auto-powers. This means that any uncorrelated noise in a component will be exaggerated and result in biased impedance calculations. A solution to this problem is to apply remote reference method (Gamble et al., 1979). It is basically using another nearby magnetic field data equivalent in time to eliminate the uncorrelated noises. Magnetic field data are preferred for applying remote reference method over electric field data, since it is not dependent on the local properties of the survey area and varies minimally within a relatively larger spatial extent. Remote reference method is applied on some of the simultaneously recorded data to remove such effects.

If the data contain non-Gaussian noise, more complex arrangements have to be implemented before getting into modeling and interpretation of the data. This may be carried out by the robust processing codes (Egbert, 1997). In this study, the robust processing code of SSMT2000 (Phoenix Geophysics Systems) was used. By implementing this processing code on time series data, 25 suitable apparent resistivity and phase curves of every component were obtained for further implementations (Figures 4.3-6).

4.5. Apparent Resistivity and Phase Curves

Impedance values might not be easy to comprehend even for the researchers with uttermost experience. For that purpose, four components of impedances are transformed into apparent resistivity and phase curves for every calculated frequency. Only xy - and yx -components of apparent resistivity and phase values are plotted due to the fact that xx - and yy -components are hard to interpret without any additional information on dimensionality analysis. Curves for the xy -component represent the ratio between the E_x and H_y , while the other components can be calculated by following the similar analogy. For our study, xy -component is referenced to N-S direction, while the yx -component contains information through the E-W direction. These curves are plotted in the Figure 4.3-6. Pseudo-sections for apparent resistivity and phase values of xy - and yx -components are also depicted in Figure 4.7.

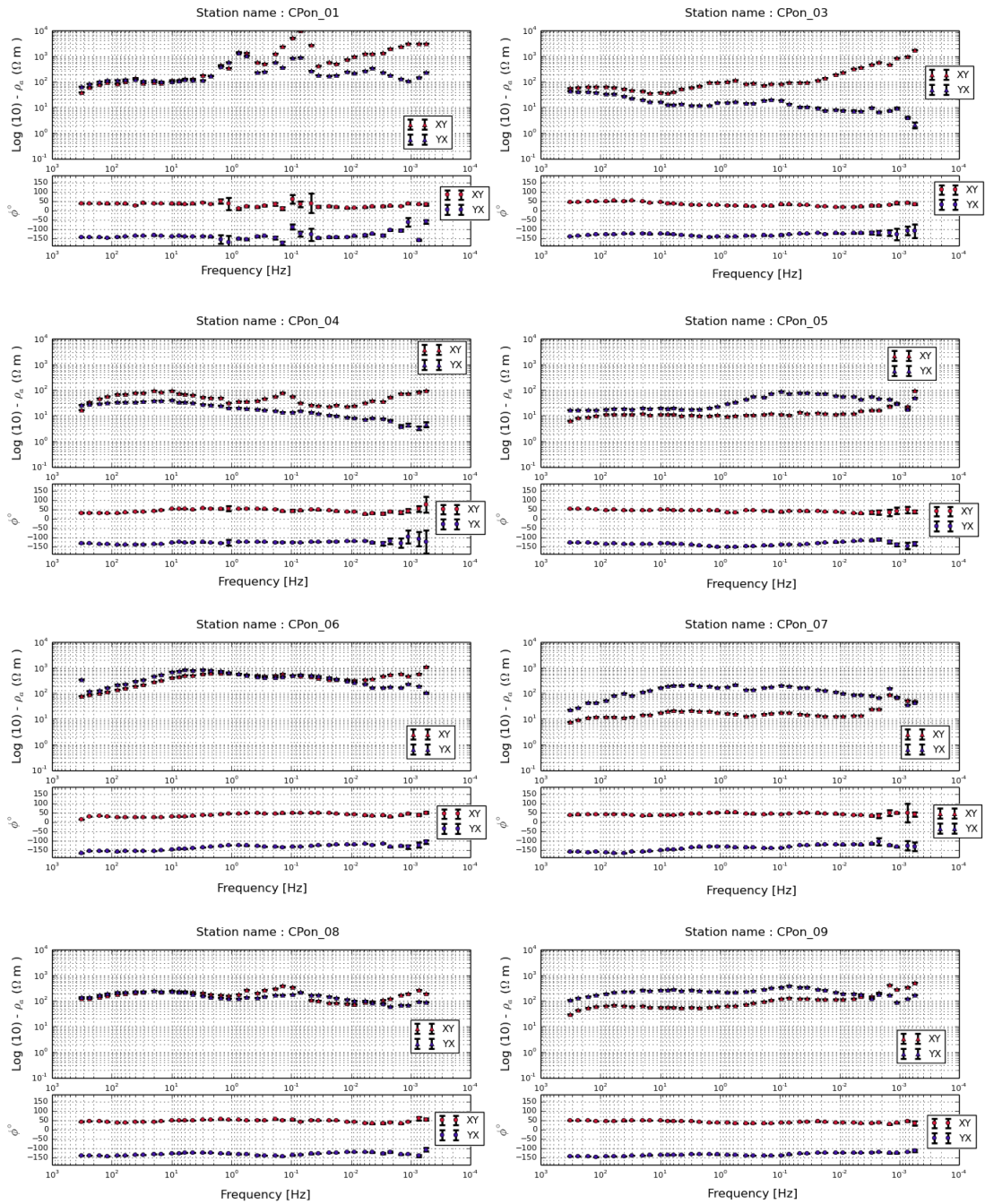


Figure 4.3. Observed apparent resistivity and phase curves for xy - and yx -components of stations 1 to 9.

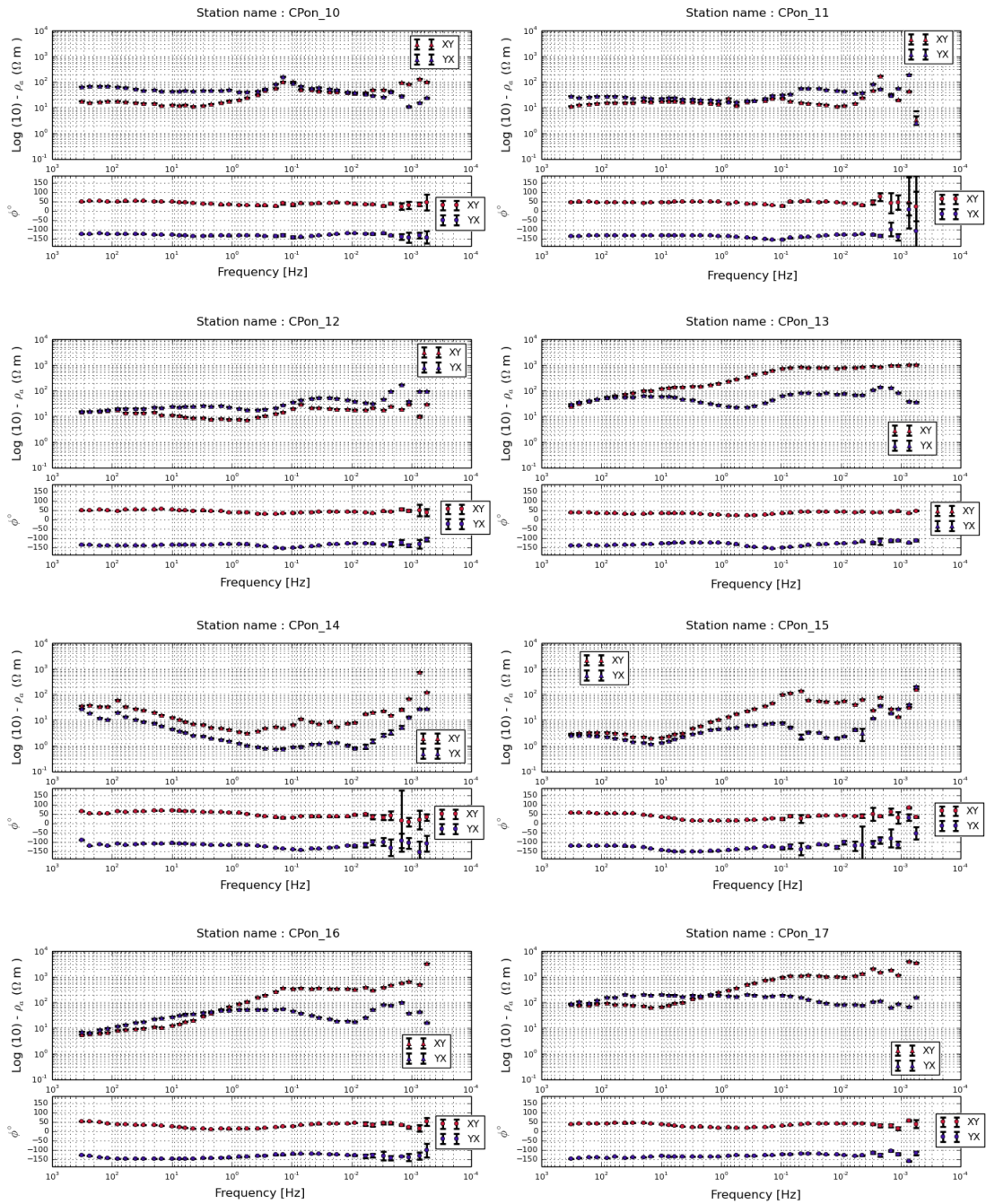


Figure 4.4. Observed apparent resistivity and phase curves for xy - and yx -components of stations 10 to 17.

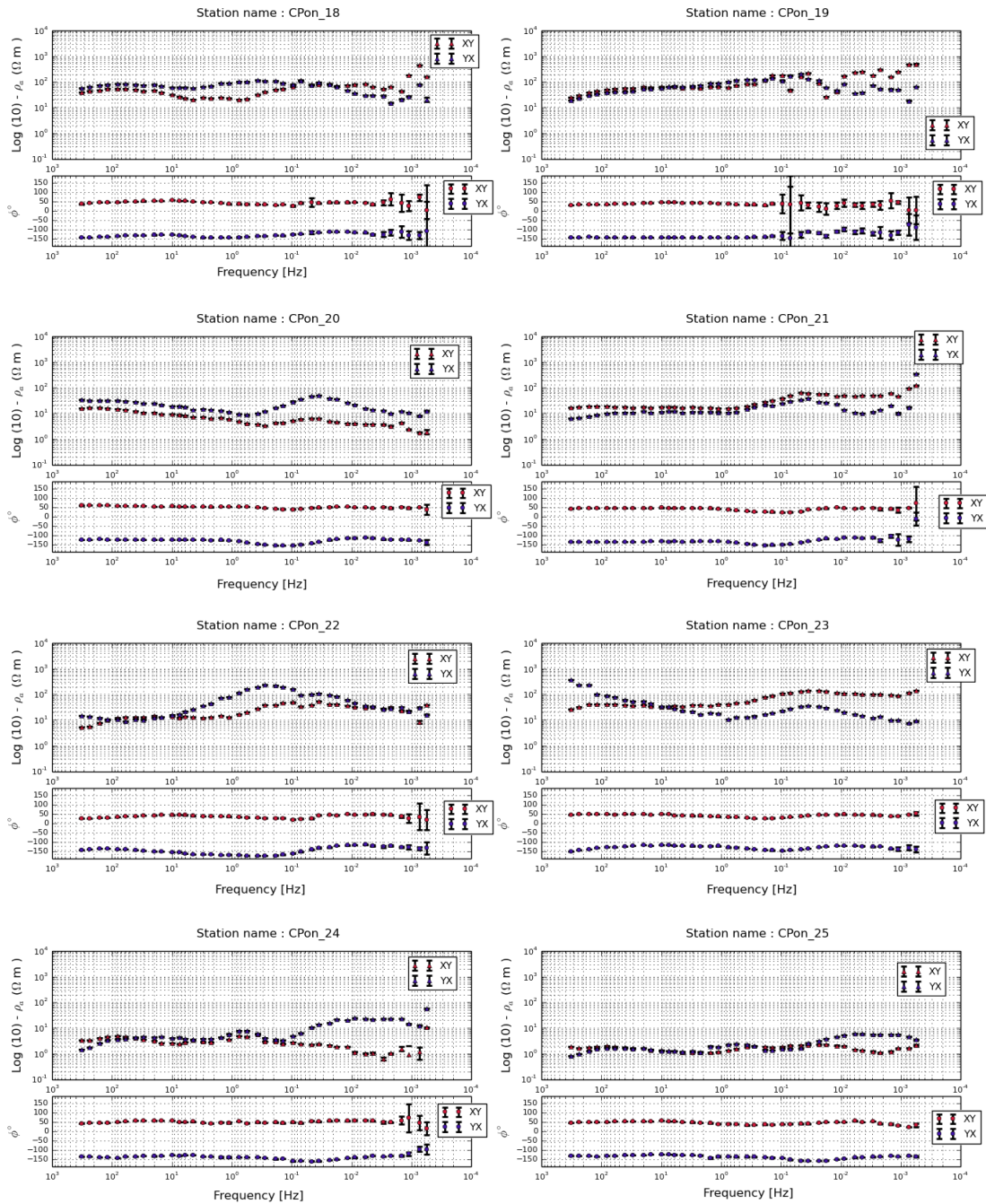


Figure 4.5. Observed apparent resistivity and phase curves for xy - and yx -components of stations 18 to 25.

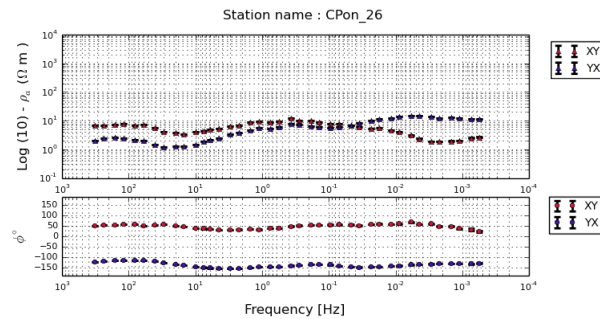


Figure 4.6. Observed apparent resistivity and phase curves for xy - and yx -components of station 26.

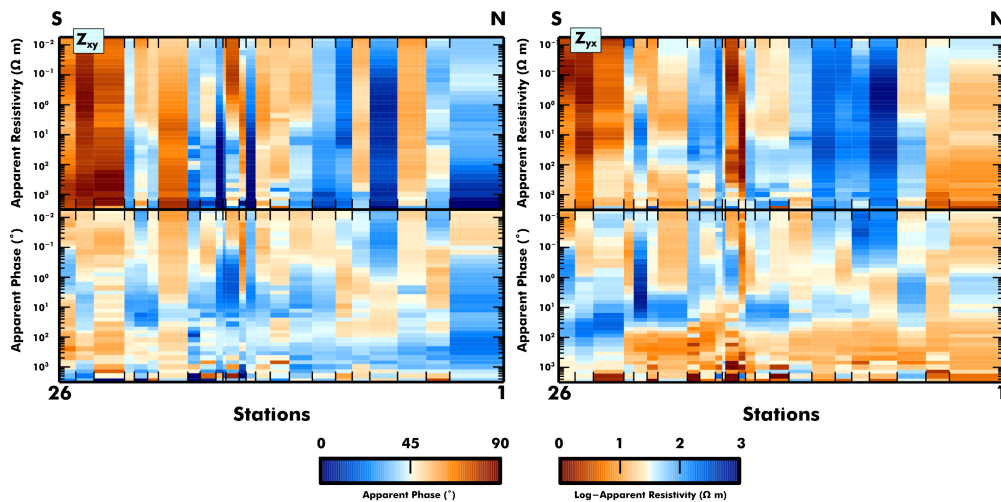


Figure 4.7. Observed apparent resistivity and phase pseudo-sections for xy - and yx -components.

4.6. Tipper Data and Induction Arrows

Tipper data can be used as a parameter to investigate the lateral conductivity variations and can be included in the inversion algorithms. For the first set of modeling trials, tipper data drastically enhanced the total RMS values. Due to their noisy state at some stations, the tipper data were excluded in the inversion of the final models. Pseudo-section of the real induction arrows for all stations is shown in Figure 4.8.

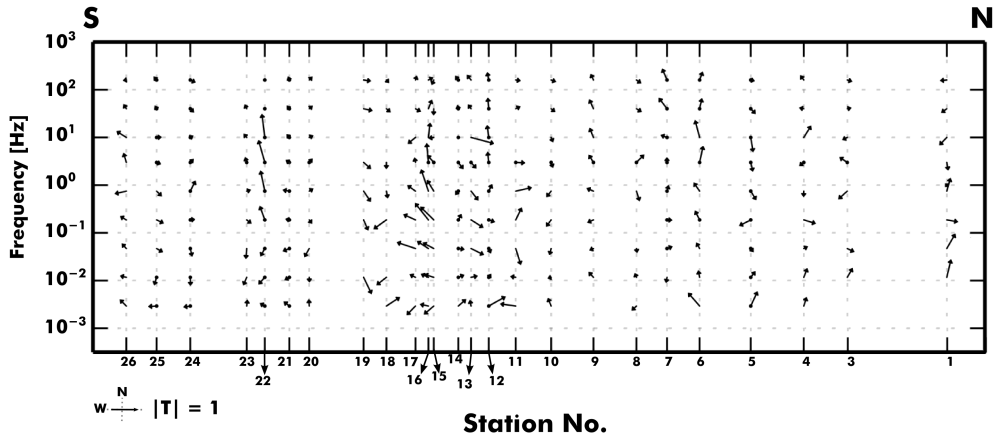


Figure 4.8. Pseudo-section of the real induction arrows for all stations.

4.7. Dimensionality

In this study, dimensionality analyses were not only used to prepare appropriate arrangements for modeling step but also to make detailed interpretations about the region. These interpretations include: (i) Detection of 2-D electrical elongations that could have caused by faults or other electrically elongated geological structures, (ii) characterization of the geological environment depending on its dimensional state, (iii) determining the position of concentrated conductive features and interpretation of their intrinsic meanings.

4.7.1. Phase Tensor

Phase tensor analyses were implemented to interpret and compare electrical structural properties of the region. After phase tensors were calculated at every data point, invariants ($\alpha, \beta, \theta, \phi$ and ellipticity) were computed to investigate the dimensional structure of the data. Observed electromagnetic fields are polarized through possible lineations like faults. They mostly align with the regional stress orientation. Local electrical characteristics of a region might change within very short distances, however in fault like systems they tend to follow the regional trend. Accordingly, implementing phase tensor analyses could help to make interpretations regarding the directional

geo-electric tendencies of the area.

4.7.2. Ellipticity of the Phase Tensor

Alignment of maximum phase value indicates the geo-electrical strike direction and its intensity grows strong when the difference between maximum and minimum phases increase. Hereby, any deviation from a perfect circle is considered as moving away from the ideal 1-D environment (Bibby et al., 2005). Ellipticity of the phase tensor is a measure to determine the amount of the two-dimensionality in a specific region. Basically, it is equal to normalized difference between maximum and minimum phases ($\frac{\phi_{max}-\phi_{min}}{\phi_{max}+\phi_{min}}$). Its value gets closer to 1.0 when the environment is 2-D. In this study, ellipticity values and strike orientations were used to depict the fault-like features. In Figure 4.9d, some of these structures can be seen around several stations, all of which show high ellipticity values and have a geological counterpart on their surface traces. These are: (i) Kızılırmak Fault (KF) zone, where the its effect is observable on the southernmost three stations, (ii) A possible dextral fault system observed near station 20, previously proposed as Yoncalı Fault by Kaymakçı et al. (2010), (iii) the NAF and related subsidiary systems between the stations 12 and 17, (iv) shallow thrust mechanism between the Esenler and Çangaldağ complexes near station 7 (Aygül et al., 2015); and finally (v) Ekinveren Thrust (EkT) near station 5.

A different approach to depict ellipticity values were made by plotting them as a graph to understand the regional tendencies of electrical variations in a more holistic manner (Figure 4.9a-c). Data are separated into three parts representing different geological environments: Stations 1 to 8 as Pontic Terrane, stations 9 to 17 as NAFZ and related structures, and stations 18 to 26 as Çankırı Region. All of the ellipticity values were plotted as well as their mean rates at each frequency. The most apparent characteristic of the three region is that, Pontic Terrane (c) does not hold 2-D features, relative to the other regions, except for two stations placed near thrust faults. On the other hand, (a) and (b) show clear 2-D characteristics but at different frequency ranges. In the zone related to NAF (b) the bell shaped curve related to seismogenic zone of NAF is quite apparent between the frequencies 4.5 Hz and 0.07 Hz. The 2-D zone of

Çankırı Basin (a) was depicted with more wide-spread values in frequency range due to conductive environment of thick sedimentary sequence of Çankırı Basin.

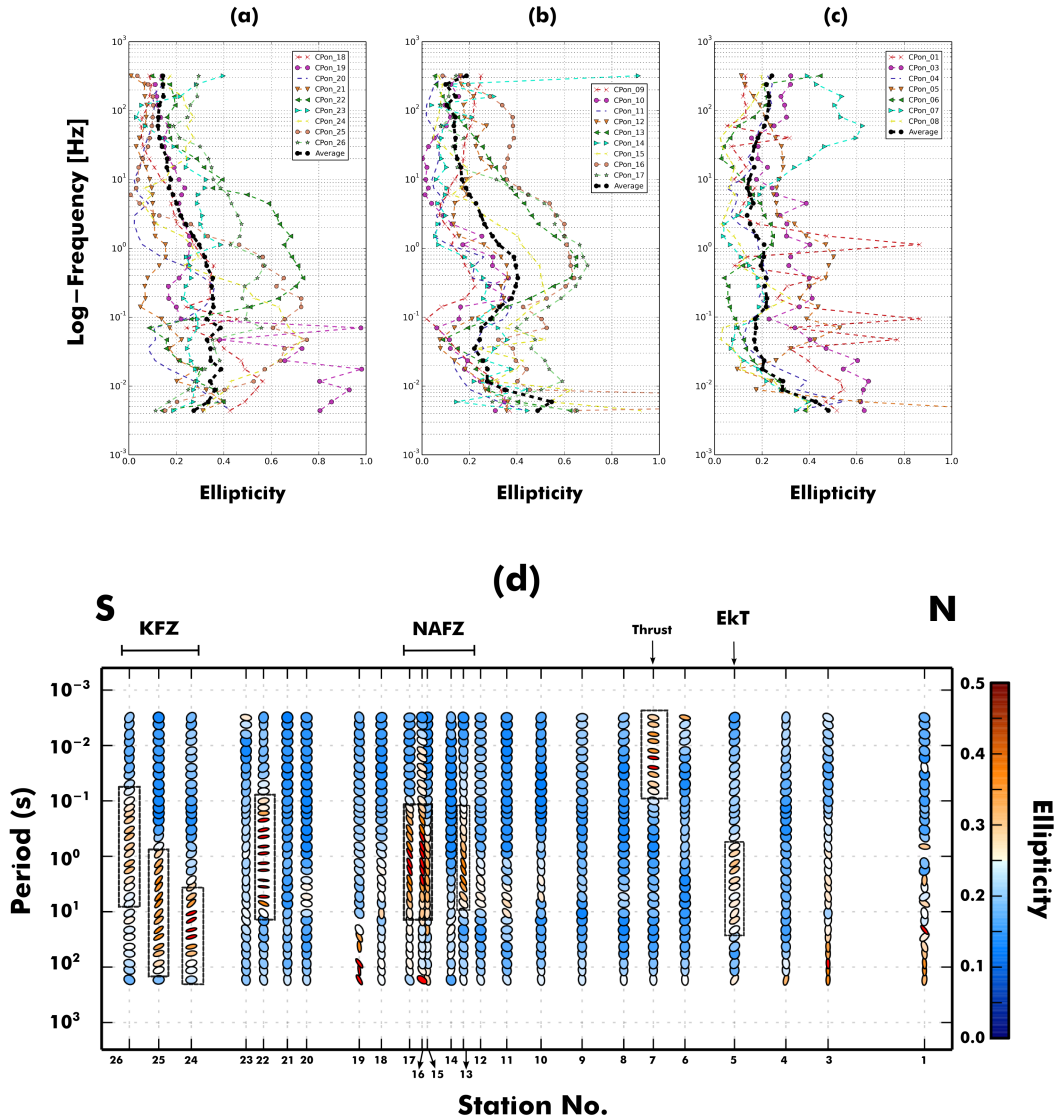


Figure 4.9. Phase tensor ellipticity variations at several frequencies of every recorded station for (a) Çankırı Region, (b) NAF Zone, (c) Pontic Terrane. (d) Pseudo-section of phase tensor ellipses filled with ellipticity values at every station. Fault-like features are shown with dashed lines. Phase tensor ellipses were reproduced after Bekin (2016).

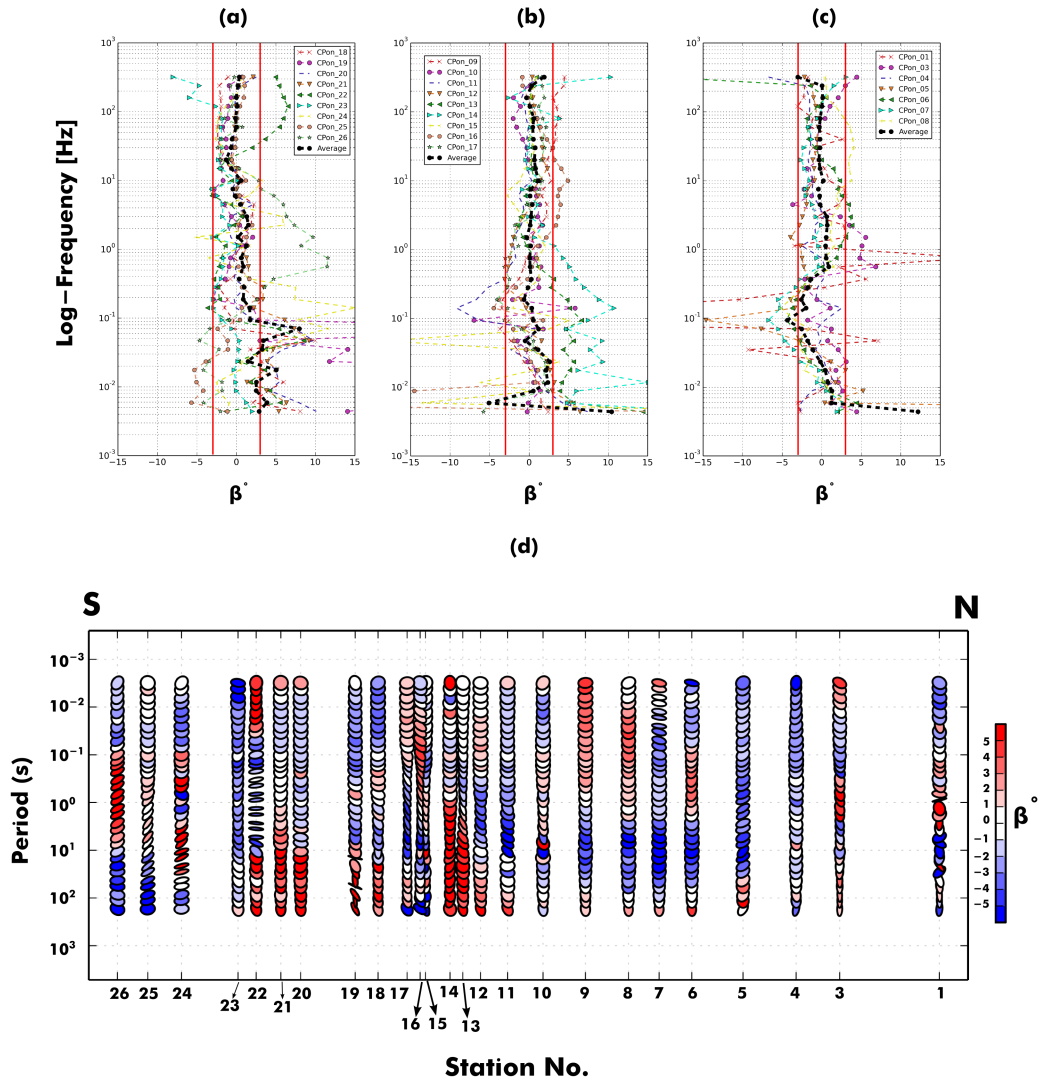


Figure 4.10. Phase tensor β variations of several frequencies at every recorded station for (a) Çankırı Region, (b) NAF Zone and (c) Pontic Terrane. (d) Pseudo-section of phase tensor ellipses filled with β angles at every station, both β° values and shapes of these ellipses reproduced after Bekin (2016).

4.7.3. Beta Invariant and Three-Dimensionality of the Data

Another property of the phase tensor can be used by calculating the β invariant. Theoretically any value of β other than zero points out a 3-D environment. However, taking the threshold value as $\pm 3^\circ$ deviation from zero is conventionally used and advised in a practical sense (Caldwell et al., 2004; Booker et al., 2013). To analyze the β invariant, the same separate data regions were used as in the ellipticity figure (Figure 4.10). The data seem to be fit within the 2-D interpretation range until 0.01 Hz at every region with a few exceptions. Some regions show high β angle variations which are relevant to their spatial position within their geological context. For instance, station 22 and 23 show high β deviations at the higher frequencies, which can be partly explained by the complex geology related to the presence of several anti- and syn-formed features probably related coexistence of dextral and normal-sense faults nearby (Kaymakçı et al., 2009). However, it will be ill-advised to make any assumptions about these shallow structures due to low skin-depth penetration of these frequencies and the relatively sparse MT data coverage in the region. Thus, an accurate discourse on the matter should be made by interpreting the lower frequencies. When a deeper seismogenic structure is present, increase in β deviations are usually observed. This is quite apparent in Çankırı and NAF regions (Figure 4.10a and b)), where β values start to increase at the lowest border while the ellipticity values indicate strong 2-D elongation. Subsequently, there is no common variation among the stations in the Pontic Terrane (Figure 4.10c). Analysis of both parameters points out the hardship that may arise from an ill-conditioned 2-D approximation, where no clear 2-D elongation exists. This may result in false interpretation of geological structures in regions like the Pontic Terrane, thus should be handled cautiously.

4.7.4. Azimuth Variations within the Region

For the phase tensor, geo-electric strike directions at corresponding frequencies are equal to $\phi = \alpha - \beta$. Figure 4.11 shows the rose diagram plot at the three regions at different frequency bands changing between $10^{-4} - 10^3$ Hz. Rose diagram graphs demonstrate the occurrence rate of observed strike values, changing from 0° to 180° .

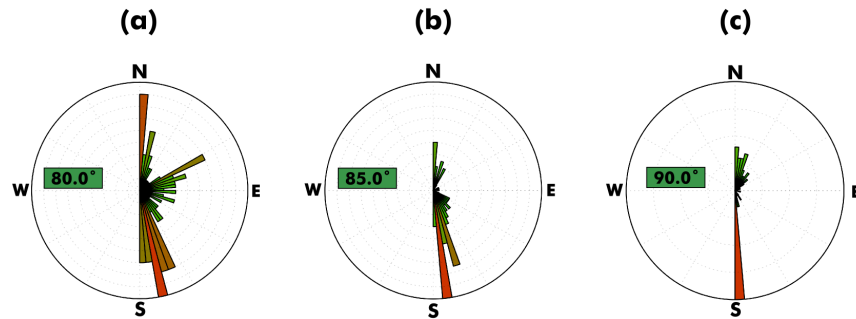


Figure 4.12. Rose diagrams for geo-electric strike directions in three different regions of (a) Çankırı Region, (b) NAF Zone and (c) Pontic Terrane. The frequencies between the range $1 \text{ Hz} - 10^{-3} \text{ Hz}$ are used.

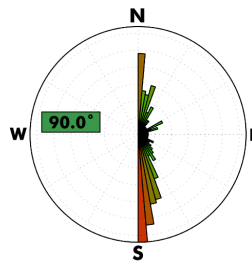


Figure 4.13. Rose diagram representation for geo-electric strike directions for all stations. The frequencies between the range $1 \text{ Hz} - 10^{-3} \text{ Hz}$ are used.

Figure 4.12 depicts the overall orientations in the desired frequency band for the three regions. Data in the vicinity of the NAF and Tosya Basin, exhibit consistent orientation of $N85^\circ E$ strike values at the southern side of the fault (Figure 4.12b). Despite the lack of seismogenic structures, data situated in the Pontic Terrane demonstrate consistent $N90^\circ E$ orientation in the region (Figure 4.12c). At the northern border of CPS, a near surface 2-D region is also spotted, which fits with the description of shallow thrust fault that exists between Çangaldağ and Esenler units (Aygül et al., 2016). Ekinveren Thrust appears at station 5 with higher rates of ellipticity and azimuth strike varying between $N60^\circ E$ and $N75^\circ E$. Data in Çankırı Region show the most complex orientation in all three of the regions. This is probably due to the existence of two separate faulting regimes in the area. One of them being the Kızılırmak

Fault Zone, which is present within the region where stations 24, 25 and 26 are situated. These data show $N75^{\circ}E$ geo-electric strike direction, which is consistent with the previous descriptions of the fault (Kaymakçı et al., 2010) and elongation of the Çankırı Basin sediments (Figure 4.9d). On the other hand, the geological formations and faulting regime is much more complex in the data from stations 20 to 23. This zone is marked by the İAES suture zone and consists of many small scale normal and dextral sense faults, in which their strike directions are closer to $N90^{\circ}E$ (Figure 4.9d). In general, targeted frequency ranges show 2-D characteristics with consistent azimuth angles, even though different geological environments were examined.

5. INVERSION OF MAGNETOTELLURIC DATA

The ultimate goal of MT analyses are to depict a reasonable resistivity image of the subsurface. Analyzing the data in their raw form may result in some understanding of a region, but it may be still hard to interpret the data in frequency-domain state and without the information that reside in the space between the stations. For this purpose, MT data are inverted into a resistivity model with an accurate physical and statistical framework. The goal of the MT researcher must be to obtain a smooth subsurface resistivity model that fits well to the data. This is a hard thing to achieve for most cases because of the non-linear nature of the MT data and the capability of it to produce infinite number of solutions. Subsequently, inversion procedure for the MT data may be a lengthy process and should be handled precisely to prevent any false interpretation. Comprehensive details of the inversion processes were described in Chapter 2.

Even though it is more computationally challenging, 3-D modeling has been proven to give more accurate results for many set of MT scenarios (Ledo et al., 2005). In this study, ModEM (Egbert and Kelbert, 2012; Kelbert et al., 2014) was used for 3-D modeling that applies a nonlinear conjugate gradients (NLCG) based algorithm. Main advantage of NLCG is that it only computes Jacobian matrix once, thus saves both computational time and memory. Two 3-D inversions were designed for the current MT data. The aim of the first scheme is to analyze the deeper structure and overall regional resistivity variations. Fifteen frequencies between the range 320 Hz - 0.001 Hz were selected for this purpose. Second MT inversion scheme was designed to depict the shallower structure (down to first 10 km) in the vicinity of NAF and related basin formations. For the NAF model, 15 frequencies were selected between 320 Hz - 0.035 Hz from the stations 9 to 19.

5.1. Regional Model

The first step of setting up an inversion scheme is to design an accurate model that fits the data. For the regional model, 25 wide-band MT stations were used in this study to form a N-S aligned profile. The nodes of the mesh were selected accordingly to prevent any overlap of stations on the mesh elements. At the core of the mesh, both northing and easting cell sizes were selected as 2.5 km. From every border, eight horizontal layers outside the core increasing in size with a factor of 1.5 were structured to prevent reverberation effects. Mesh had 42 cells in the vertical direction increasing in size with a factor of 1.2. The thickness of the first layer was selected as 0.1 km, which was accurate enough to solve the corresponding frequencies at shallower layers. The total number of cells in X-Y-Z directions were 87 x 36 x 42, respectively; resulting in a total cell number of 131544. Extents of the mesh were 342.49 km in northing, 214.99 km in easting and 1057.735 km in vertical directions. Resistivity of the initial model was selected as 100 Ωm . Northern end of the model was fixed to values of 0.3 Ωm to a certain depth, to mimic the coast effect of Black Sea.

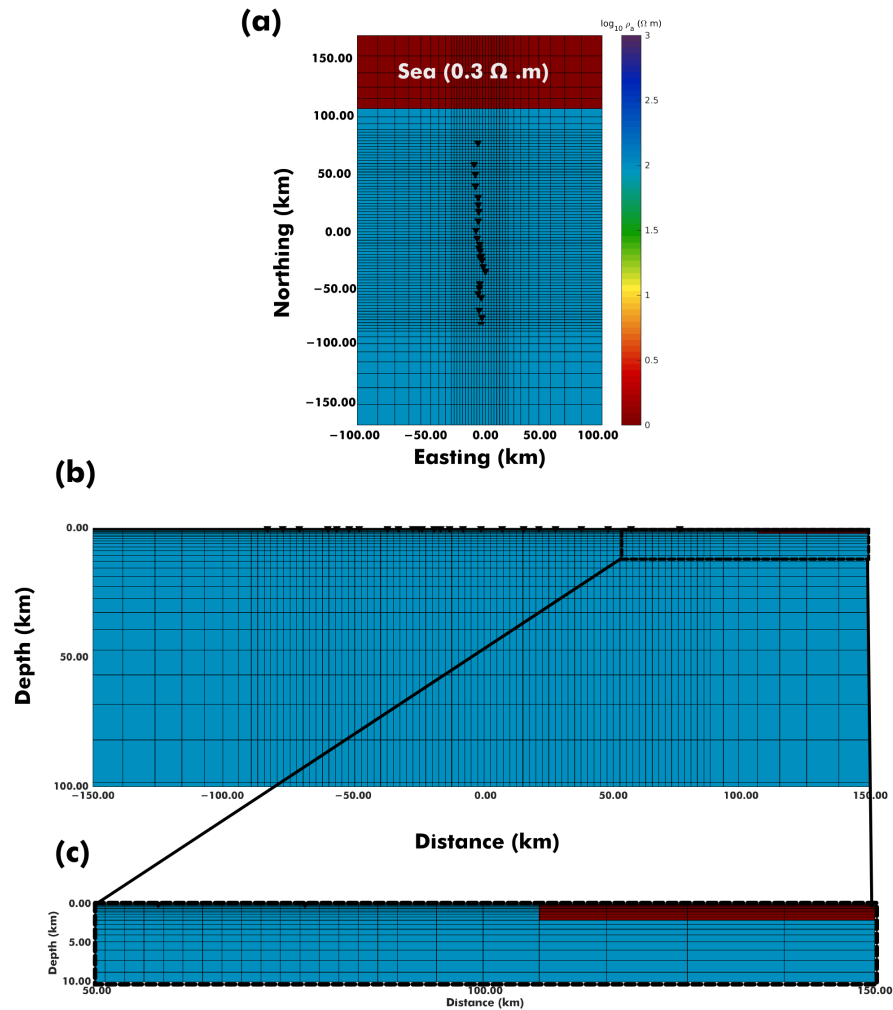


Figure 5.1. Illustration of the initial model of the 3-D modeling scheme (a) from top, (b) as a cross-section. The close up version of (b) was given in the figure (c) to illustrate the mesh nodes assigned for the sea effect. Logarithmic scale was used for the colorbar.

First set of experiments on 3-D modeling were made to test the effects of different components of impedance tensor and tipper data. Error rates were selected as $\sqrt{Z_{xy}Z_{yx}} * error\ rate$ for off-diagonal and $\sqrt{Z_{xx}Z_{yy}} * error\ rate$ for diagonal elements. Regularization parameter was selected as 0.1 for all trials. Covariance smoothing matrix was taken as a constant rate with 0.3 at every direction in every cell. Figure 5.2 depicts the 7 results of the trials alongside with a table that includes the parameters used.

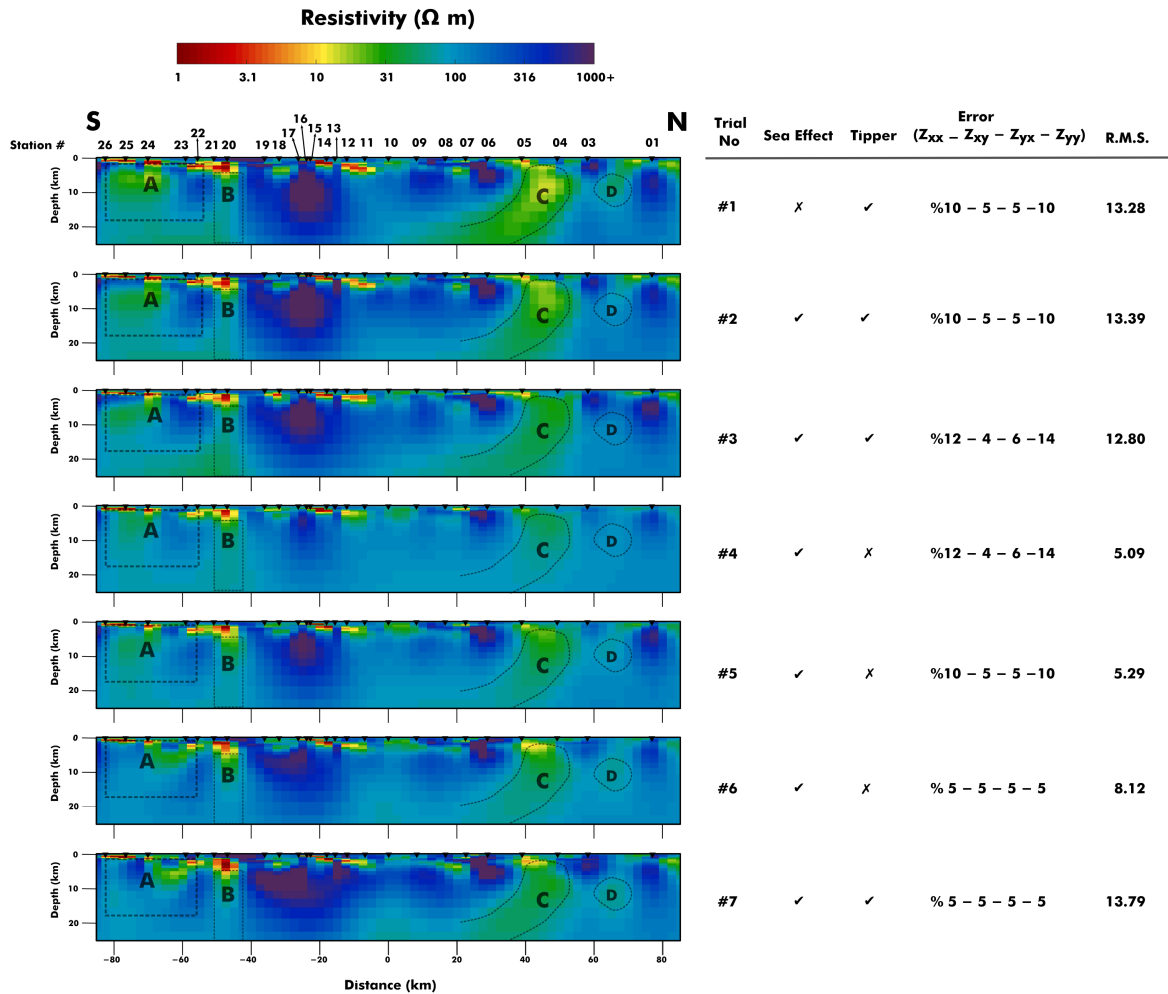


Figure 5.2. Seven 3-D modeling attempts with ModEM using different parameters as shown on the table. Dashed lines indicate the inconsistent regions on the models.

Logarithmic scale was used for the colorbar.

5.1.1. Interpretation of Preceding Modeling Attempts

The most consistent inference throughout all modeling attempts was that the tipper data drastically decreased the fitting rates on overall. This is understandable due to the noisy state of tipper data at some stations. Additionally, sharpening the edges of anomalies were observed within the modeling attempts that used tipper data. Since there was no significant input of tipper data regarding the interpretation of deeper and regional structure; they were not included in further inversion trials to reduce the overall RMS values.

The effect of error rates on diagonal elements are quite observable on both overall resistivity variation and values of some specific anomalies. These questionable features are indicated with dashed lines on Figure 5.2. They were selected due to their inconsistent resistivity distribution observed at different trials. On the models, Zone A is located under the thick sequence of sedimentary layers that make up the Çankırı Basin, where low resistivity values were observed. The fact that its value varied between the stations, make this area a ambiguous feature on the models. This area also is in possession of a localized strike direction of $N75^{\circ}E$, which is considerably different from the overall strike value of $N90^{\circ}E$. Such an angle agrees well with the geological strike of Kızılırmak Fault and may add complexity on the models that are produced. Zone B is situated beneath the station 20, which has remarkably low resistivity values. The low resistive zone at this location reaches out to the deeper structure, and geologically quite excessive. Ambiguous state of the output was also backed up by the residual rates at the area, which show persistently poor fit at mid-to-lower frequencies (see Appendix A). A third ambiguous feature on the models are labeled as C, appearing as a conductive feature located between the stations 3 and 6. Zone C seems to follow the possible border of CPS at depth. Considering the large scale of the anomaly, this zone has to be analysed with sensitivity tests for further interpretation. Zone D is another relatively conductive anomaly that connects with Zone C at shallower levels. Despite the overall and local fitting rates, major structures are all resolved with similar spatial attributes.

As expected, inversion schemes prepared with higher diagonal error rates have produced smoother but more geologically unreasonable models. This situation is overtly apparent, when trials 3 and 4 are compared. Without the assistance of tipper data, trial 4 failed to illustrate any reasonable detail about deeper structure that trial 3 was able to portray. This situation brings out the importance of selecting appropriate error floor rates as previously stated by Tietze and Ritter (2013).

Because the data were collected to form a 2-D profile, diagonal elements were much harder to fit when compared to off-diagonal elements. Before making any interpretation, one should understand that in profile-based measurements, most of the

off-profile contributions to the models are contained in the diagonal data (Siripunvaraporn et al., 2005). However, even in profile-based measurements, 3-D modeling is proven to give out more reliable results compared to 2-D modeling (Ledo, 2005; Siripunvaraporn et al., 2005). One of the main limitations while applying 3-D inversion in a large scale profile-based data is to reduce the RMS rates to an acceptable level. For further analyses, same model space was preserved, but some of the inversion parameters were changed accordingly to make a model that fits the data better and produce more geologically reasonable features.

5.1.2. Final Inversion Scheme for the Regional Resistivity Model

The final inversion attempt was carried out by choosing error rates as $5.0 \times \sqrt{Z_{xy}Z_{yx}}$ for the all elements of the impedance. This particular type of setting for error rates was used in many modern 3-D MT studies (Meqbel et al., 2014; 2016; Patro and Egbert, 2011; Karaş et al., 2017) and it prevents the diagonal data to be unduly weighted (Kiyani et al., 2013). However, its affect should not be still the same as using error rates based on their individual elements. Possible loss of information that may arise from downweighting the contribution of diagonal elements by using error variances based on off-diagonal data, as seen in the previous modeling attempts, can be compensated by increasing the roughness parameter of the model. A possible method is to select different smoothness parameters for different directions, i.e. an anisotropic model covariance matrix. However, selecting an anisotropic covariance matrix might be tricky for MT modeling and may produce erroneous effects, especially if the model grid and the data are not aligned on geo-electric strike orientation (Patro and Egbert, 2011). Importance of data rotation in 3-D MT was also tested for the MT data near the San Andreas Fault by Tietze and Ritter (2013). They concluded that the data and model grid rotated to the geo-electric strike angle, should produce more reliable results for 3-D modeling for data-sets that cover a large spatial span. Fortunately, the data in this study were collected on an orthogonal profile to the regional geo-electric strike angle (Figure 4.13), thus there is no need for such rotation of the data.

Kiyani et al. (2013) produced synthetic models to test the capability of a 3-D

inversion scheme that uses only off-diagonal elements to depict an obliquely placed conductor at depth. According to these tests, models produced only with the off-diagonal elements were only capable of accurately detecting an oblique conductor if the data and model grid were rotated to the geo-electric strike orientation. This means that even with an inversion scheme only carried out with off-diagonal elements, there is a good chance of producing an accurate model that represents the regional resistivity distribution with the current data. Since the data in target frequency range show consistent strike angles (Figure 4.12,13), lacks regional oblique conductors and fit mostly within the practical description of 2-D phase tensor β range (Figure 4.10); constraining the diagonal error rates with off-diagonal based noise levels, becomes more applicable. Subsequently, this arrangement of selecting off-diagonal based error rates would help to enhance the overall fitting rates with minimal loss of regional resistivity information.

For the final inversion scheme, covariance matrix parameters were selected as 0.2 in N-S, 0.4 in E-W and 0.3 in vertical directions, which means a slightly rougher model in the N-S direction. The initial line search step size value was reduced to 1.0, because the preceding trials with longer step sizes were stuck in the local minima and were not able to reach a global minimum. Smaller initial trade-off parameter (τ) was also selected for the first iterations to increase the weighting on the data misfit rather than smoothing operator. For the later iterations this parameter gradually increases to bigger values to increase the effect of smoothing. Final regional inversion scheme converged in a model with RMS value of 3.52 at the end of 102th iteration. Cross-section of the resistivity model can be seen in Figure 5.3. The residual rates for the regional model is illustrated in 5.4.

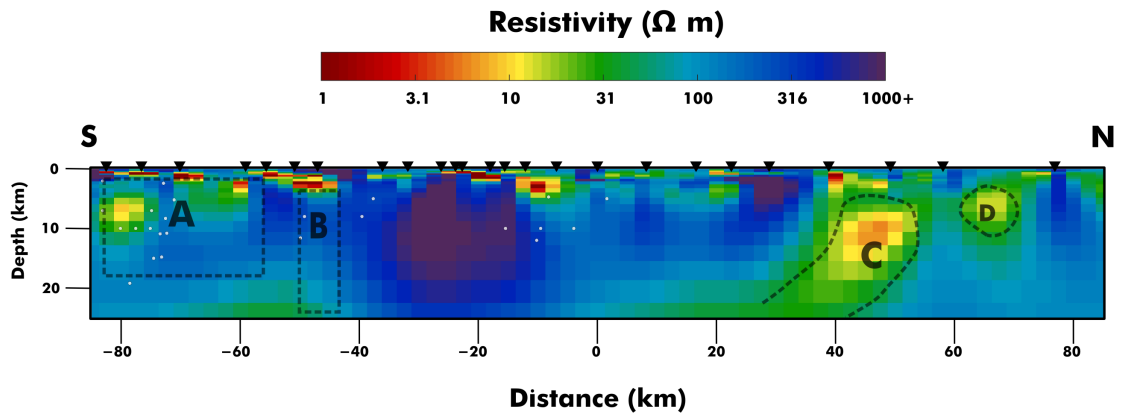


Figure 5.3. Final regional resistivity model. White dots represent the earthquake hypocenters taken from the ISC catalogue.

The output of the final inversion scheme appears rougher than the preceding trials. For the zones A and B, the final inversion results demonstrated more geologically sound resistivity distributions that agrees well with the descriptions of Kaymakçı et al. (2009; 2010). The fitting rates within the area, stations 19 to 26, were considerably increased in mid-to-lower frequencies for the final resistivity model (Figure 5.4, see Appendix A for the residual rates of the preceding models.). The fitting curves of the final model were given in Appendix B. In overall, regional resistivity distribution are pictured with better fitting rates.

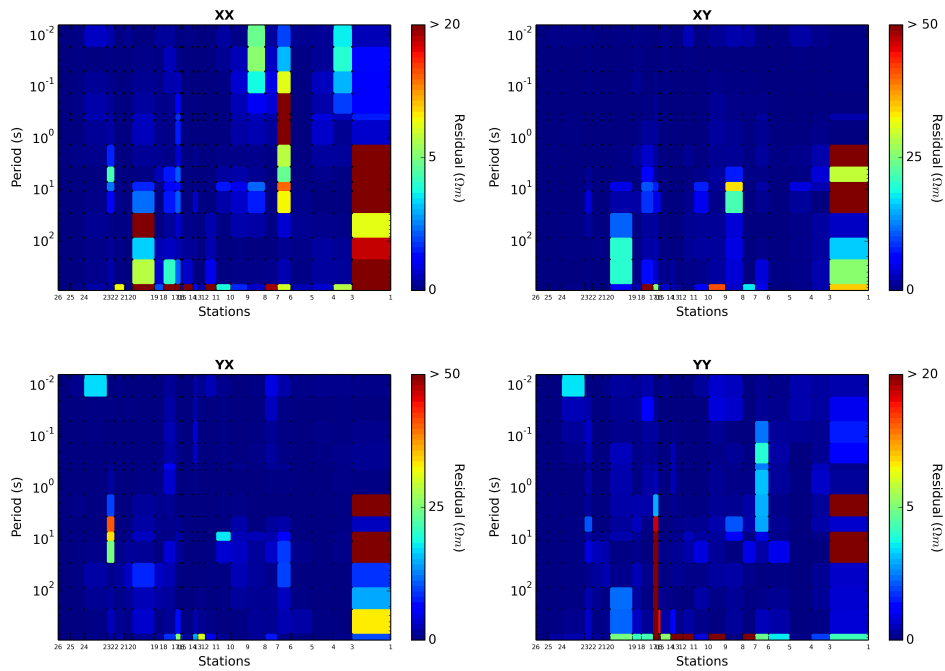


Figure 5.4. Apparent resistivity residuals for the four components of the impedances, acquired after the 102^{th} iteration of the final resistivity model.

5.2. The NAF Model

The second MT inversion scheme was carried out by using the data of 10 stations (stations 9 to 19) within a frequency range of 320 Hz - 0.035 Hz. By implementing this inversion scheme, a more densely structured model is sought, which should resolve the first 10 km with higher resolution than the regional model. The mesh was built with evenly spaced 0.75×0.75 km nodes at the core of the mesh. Eight padding stations are placed increasing by a factor of 1.5. 35 vertical layers were selected with 1.2 increasing factor starting with initial layer thickness of 0.05 km. Every cell are selected as constant value of $100 \Omega m$ for starting model. The attained initial model for these parameters can be seen in Figure 5.5.

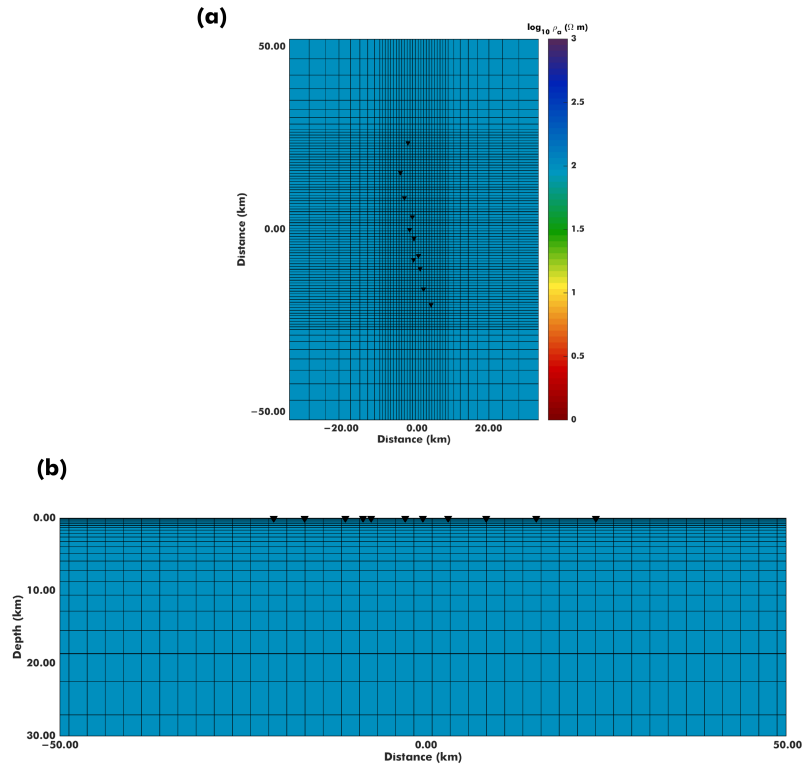


Figure 5.5. Initial model of the 3-D modeling scheme for the NAF model. Black triangles indicate the stations. Logarithmic scale was used for the colorbar.

For the inversion scheme, isotropic covariance matrix was used with 0.3 at every direction and every cell. Tipper data were not included in inversion scheme due to their noisy state. Full impedance tensor was inverted with error floor selected as $5.0 \times \sqrt{Z_{xy}Z_{yx}}$ for all components. The final model was acquired after 82th iteration with 2.03 RMS. A cross-section of the final resistivity model passing through the model center can be seen in the Figure 5.6. Residual rates for all components are also given in Figure 5.7. The fitting curves of the NAF model can be seen in Appendix C.

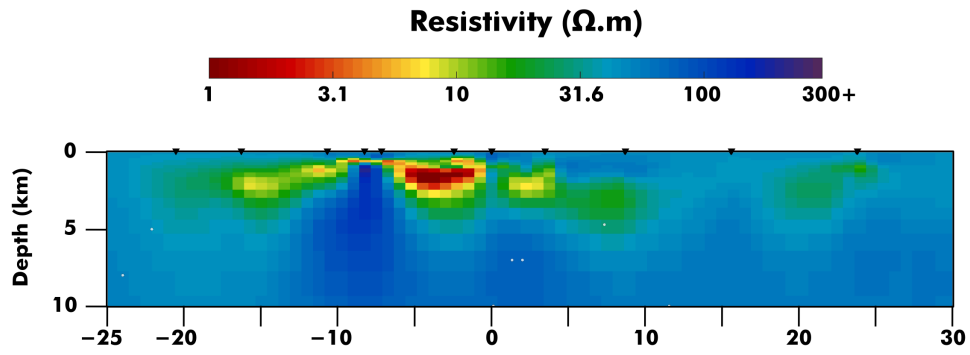


Figure 5.6. Resistivity section for the NAF model passing through model center. White dots represent the earthquake hypocenters taken from the ISC catalogue.

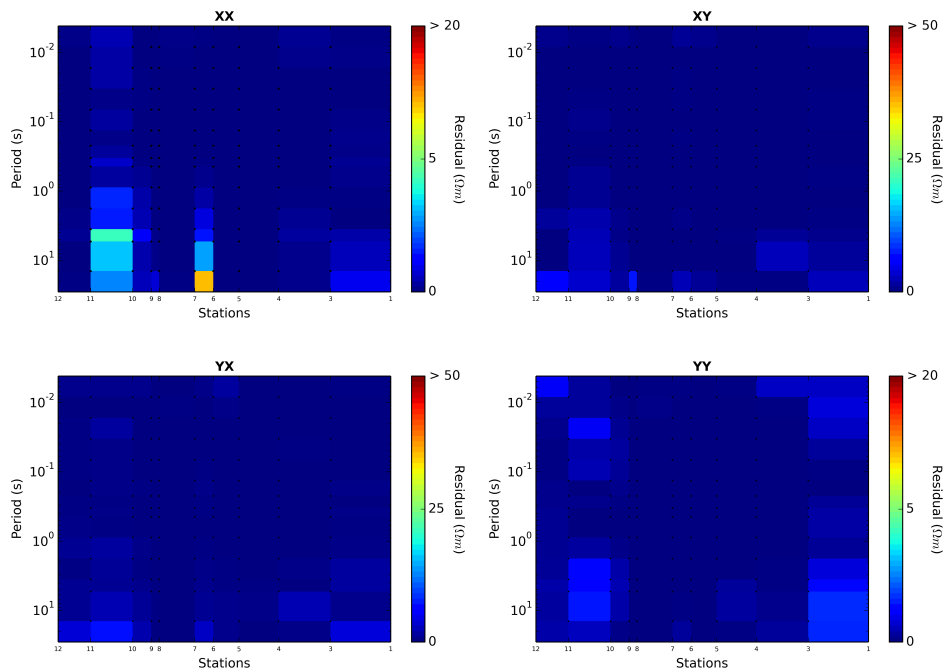


Figure 5.7. Apparent resistivity residuals for the four components of the impedances, acquired after the 82th iteration of the NAF model.

5.3. Sensitivity Tests

Sensitivity tests were carried out to check the validity of certain anomalies seen on the models. They were carried out by injecting resistive anomalies over the conductive questionable features in resultant models. Then the forward run for the altered models were performed.

5.3.1. Sensitivity Test for the Conductive Anomaly C

First test was made to investigate the deep conductor placed beneath stations 4 to 6. This anomaly was masked with $300\ \Omega m$ values starting at the bottom of the model reaching to three different upper boundaries: 6 km, 11 km and 16.3 km for three different sensitivity experiments. The results of these experiments can be seen in Figure 5.8.

Difference between data and sensitivity responses get lower when the upper bound of the injected structure gets deeper. RMS values also gradually decreased from 3.89 to 3.52, while injecting a deeper anomaly in the region. According to the forward model tests, data turned out to be sensitive to this anomaly at all tested depths. However, beneath the depths of the last experiment, regions beneath it may be rather poorly resolved.

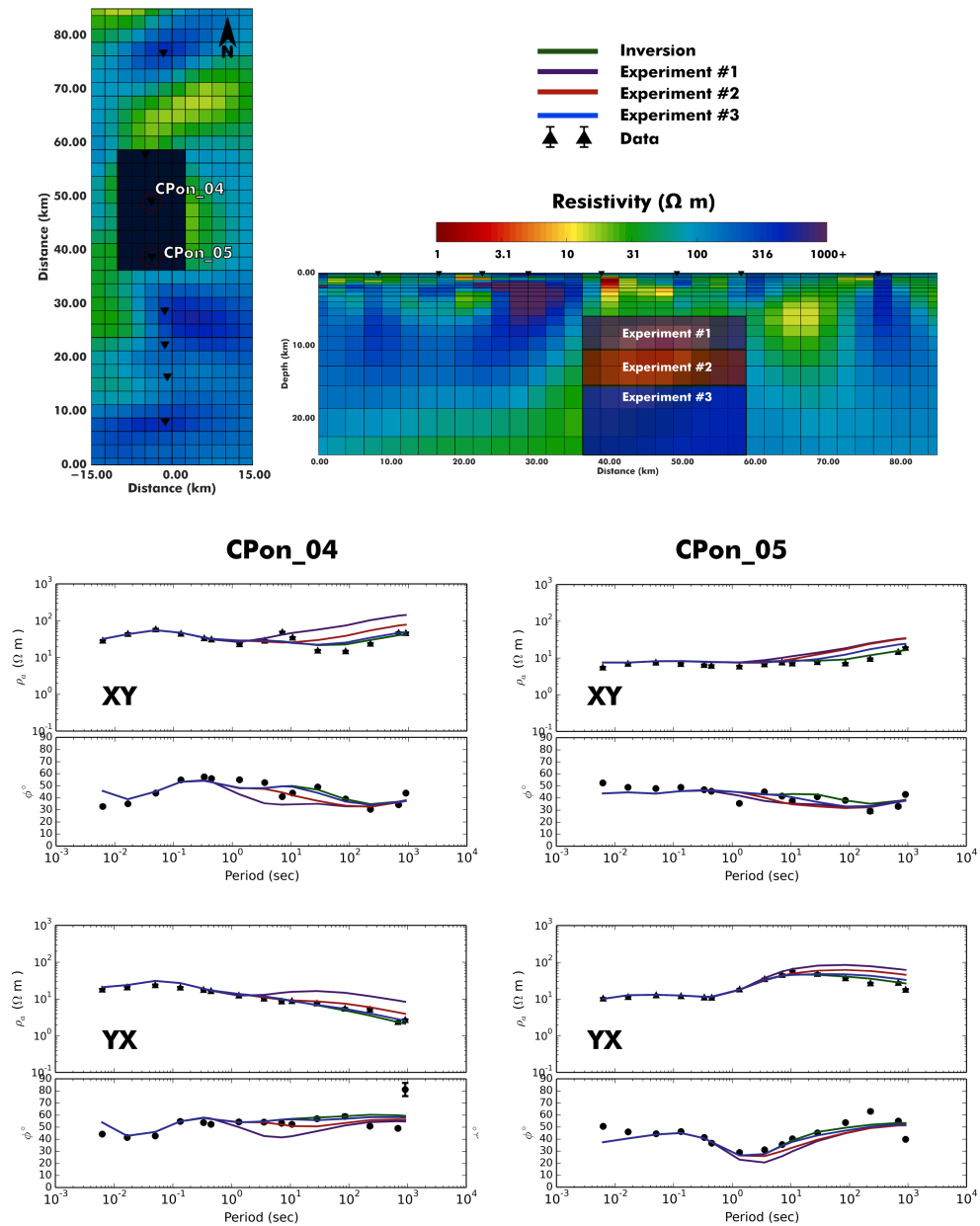


Figure 5.8. Sensitivity tests for conductive anomaly placed between the stations 4 and 5. Maps indicate the injection methodology and the graphs represents the responses of xy - and yx -components for the three sensitivity experiments.

5.3.2. Sensitivity Tests for the Base of the Tosya Basin

Another sensitivity test was conducted for determining the base of the Tosya Basin to validate the shadow effect of conductive feature. For this purpose, conductive

feature representing the Tosya Basin was injected with anomalies representing the surrounding region for depths: 1.9, 2.4, 2.9 and 3.6 km. Interpretation of this test was carried out by checking the RMS values of the forward responses. RMS values gradually decrease from 2.12 to 2.0363, while the top of the injected anomaly reaches at 3.6 km (Figure 5.9). This result indicates that the base of the Tosya Basin is in proximity of a value between 3.6 and 4.3 km and shadow effect is present for deeper structure.

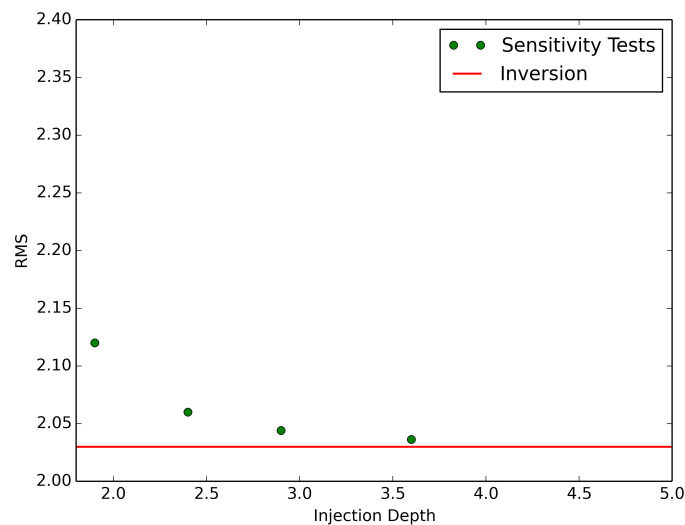


Figure 5.9. RMS values of the forward responses produced with sensitivity tests made to determine the validity of the conductive anomalies around Tosya Basin. Graph demonstrates the upper position of the injected anomaly versus RMS rates that were observed.

6. RESULTS AND DISCUSSION

Wide-band MT data were collected in the form of a profile in north-central Turkey passing through Neo- and Paleo-Tethyan accretionary realms and their active tectonic imprints. Inversion schemes and data analysis techniques were implemented to resolve target structures in the study area. There are many extensive geological explanations for this region, but few geophysical studies were performed. Resolving the structure by means of MT method should invoke uncovered details on the rheological and tectonic properties of the study region.

6.1. Resistivity Structure in the vicinity of the NAF and Relative Tectonic Implications

In the final model, with all the stations involved (Figure 6.1,2), the major geological structures playing a dominant role in the region are depicted as clear resistive or conductive anomalies. One of the most distinguishable features is a large resistive body ($> 1000 \Omega m$) observed just south of the NAF. Its voluminous nature is quite reasonable within the evolutionary context of supra-subduction environment that took place in the region, referring to ophiolite obduction and collision of Köşdağ Island Arc (Kaymakçı et al., 2009; Aygül et al., 2015). The surface trace of the Köşdağ Arc is visible on the NAF model (Figure 6.3), describing a major anticline as previously claimed by Aygül et al. (2015). The models shown in Figure 6.1b and 6.3 enlighten its deeper roots, too. Acquired models and geological implications on the area suggest that obduction/emplacement of the ophiolites in accordance with collision of the Köşdağ Arc are plausible explanations for the presence of this large resistive body that extends towards Gondwanan margin and constitutes a basement for the suture zone.

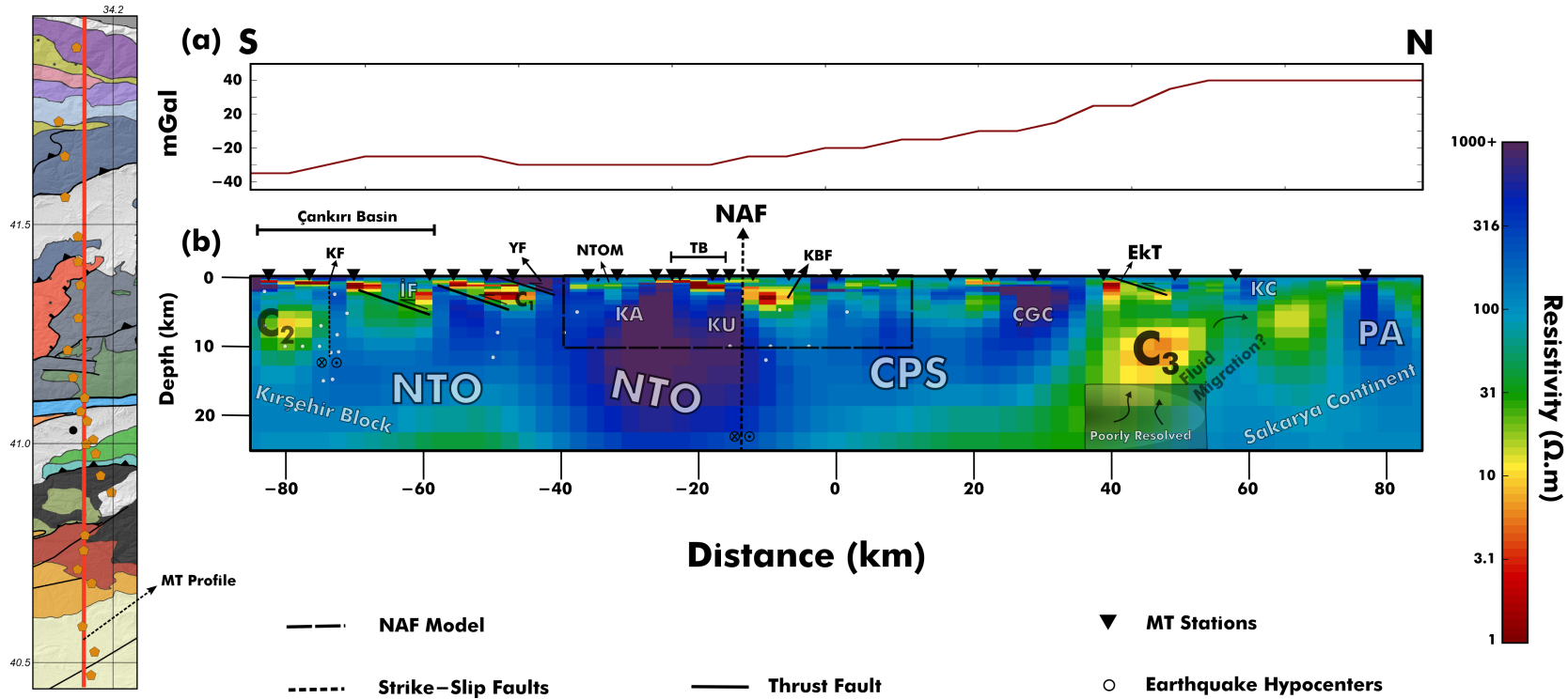


Figure 6.1. (a) Free Bouguer anomaly values along the selected profile taken from Ateş et al. 1999. (b) Cross-section from the regional resistivity model with interpretation. ÇB: Çankırı Basin, ÇGC: Çangaldağ Complex, DC: Domuzdağ Complex, İF: İncik Formation, KA: Kösdağ Arc, KU: Kunduz Unit, KBF: Kirazbaşı Formation, KC: Küre Complex, KF-1: Kızılırmak Fault 1, KF-2: Kızılırmak Fault 2, KF-3: Kızılırmak Fault 3, NTO: Neo-Tethyan Ophiolites, NTOM: Neo-Tethyan Ophiolitic Melange, PA: Pontide Arc, TB: Tosya Basin, YF: Yaylaçayı Formation. Logarithmic scale was used for the colorbar. White dots represent the earthquake hypocenters taken from the ISC catalogue.

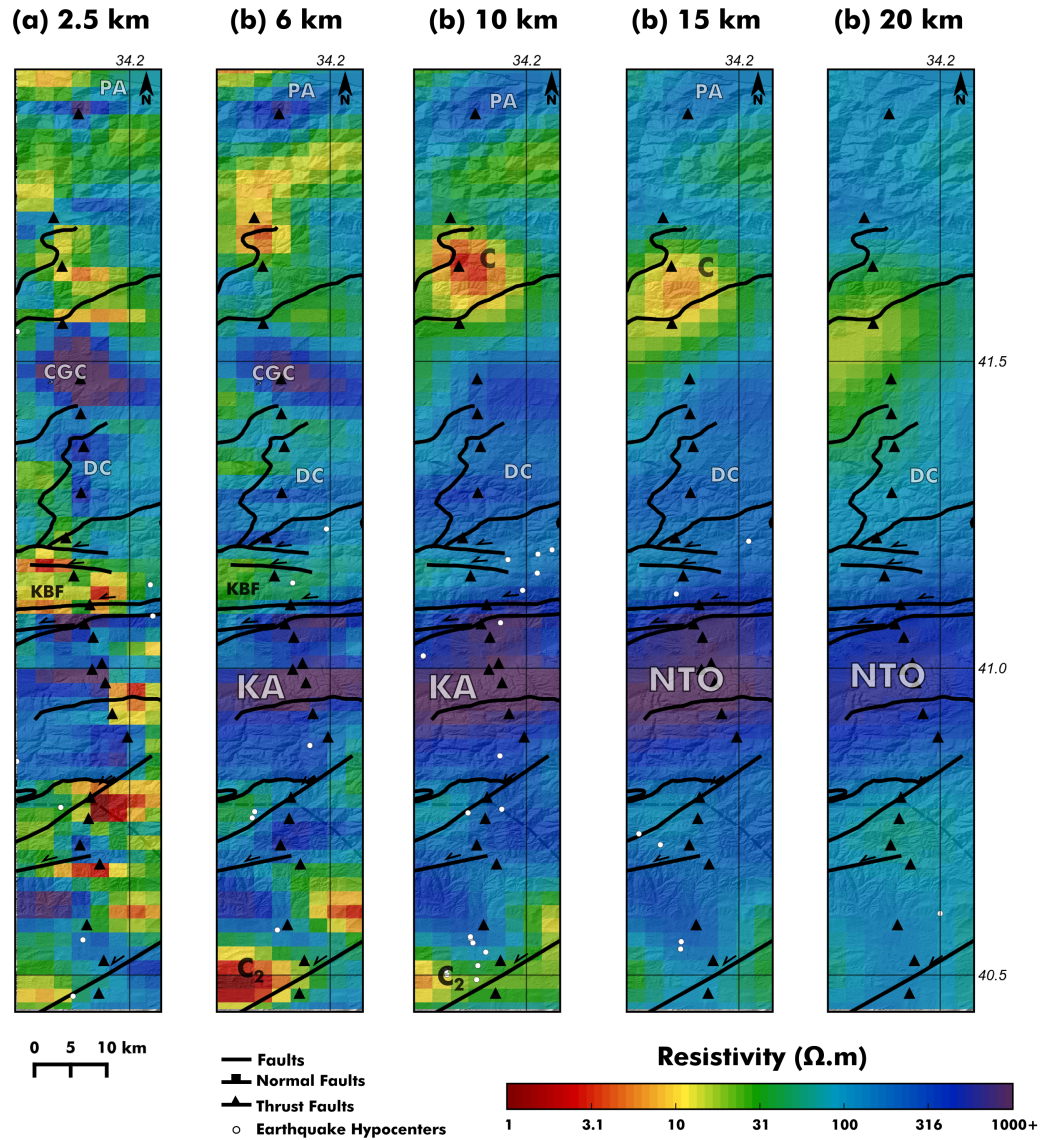


Figure 6.2. Map view of regional resistivity model for depth slices (a) 2.5 km, (b) 6 km, (c) 10 km, (d) 15 km, (e) 20 km. CPS: Central Pontides Supercomplex, ÇGC: Çangaldağ Complex, KA: Kösdag Arc, KBF: Kirazbaşı Formation, NTO: Neo-Tethyan Ophiolites, PA: Pontide Arc. Logarithmic scale was used for the colorbar. White dots represent the earthquake hypocenters taken from the ISC catalogue.

The large resistive body in the south of the NAF is in tectonic contact with relatively lower resistive ($> 150 \Omega m$) zone made up of large metamorphic sole of Central Pontides Supercomplex (CPS)(Figure 6.1,2). The sharp resistivity contrast clearly illustrates the effect of ~ 85 km total offset along the fault (Hubert-Ferrari et al., 2002). This large resistive body also depicted with lower V_p/V_s ratios suggesting lack of fluid inclusion within the area (Yolsal-Çevikbilen et al. 2010). Relatively quiescent moderate-to-high magnitude seismicity on the fault segment might be linked to the rheological attributes of the region. Previously, MT measurements made on locked strike-slip segments of major faults demonstrated a similar characteristic portrayed by presence of resistive bodies appearing at both sides of the fault (Karaş et al., 2017 ; Goto et al., 2005 ; Unsworth et al., 1999). Reasoning of this concept mainly stems from velocity strengthening effect of fluid inclusion into fault zones (Rice, 1992; Hickman et al., 1995). This property has been depicted several times earlier by MT applications along the NAF (Tank et al., 2003, 2005; Kaya et al., 2013). Both the metamorphic units of CPS and mafic units south of the NAF can be interpreted as reasonable geological bodies to resist such inclusion of fluids into the fault zone due to their low porosity values or poor interconnection between their pores.

The unstable seismogenic portion of a fault may increase in length without any additional hydrostatic pressure backed up by interconnected fluid-filled pore systems (Scholz, 1998). Peyret et al. (2012) found that the brittle to ductile transition near NAF gradually increases from 15 km to 25-30 km between the longitudes of N34.20°E and N34.50°E. MT profile collected in this study crosses the NAF at N34.15°E, but causative geological features that ensure a mechanically strong base (Central Pontides Super Complex and Köşdağ Arc) converge together between these determined intervals. Existence of quartz-poor and feldspar-rich mafic minerals in the vicinity of NAF might also infer to the deeper lower-crust exposure, since the transition to plasticity is closely related to mineral composition of these formations (Scholz, 1988). Hence, an accurate extrapolation of MT resistivity model should be a possible option to explain the rheological environment, which causes a deeper brittle-ductile transition zone in the area.

The conductive environment just north of the fault coincides with the ophiolitic melange units of Kirazbaşı Formation placed below 5 km (Aygül et al., 2016; Figure 6.3,4). This unit overlies the Domuzdağ Complex from the north and it is in tectonic contact with the Kunduz Metamorphic Unit via the NAF. Kunduz Unit meets with the Cenozoic Tosya Basin sediments in the south, which appears as a clear conductive syncline in the models (Figure 6.3). Sensitivity tests made near the Tosya Basin reveal that the basement of the basin is in a proximate value between 3.6 km and 4.3 km. It is debatable whether Köşdağ Arc or Kunduz Unit are underlying the Tosya Basin sedimentary sequence. Neo-Tethyan Ophiolitic Melange (NTOM) also depicted as heterogeneous conductive features just placed south of the resistive feature corresponds to Köşdağ Arc (Figure 6.1b, 6.3).

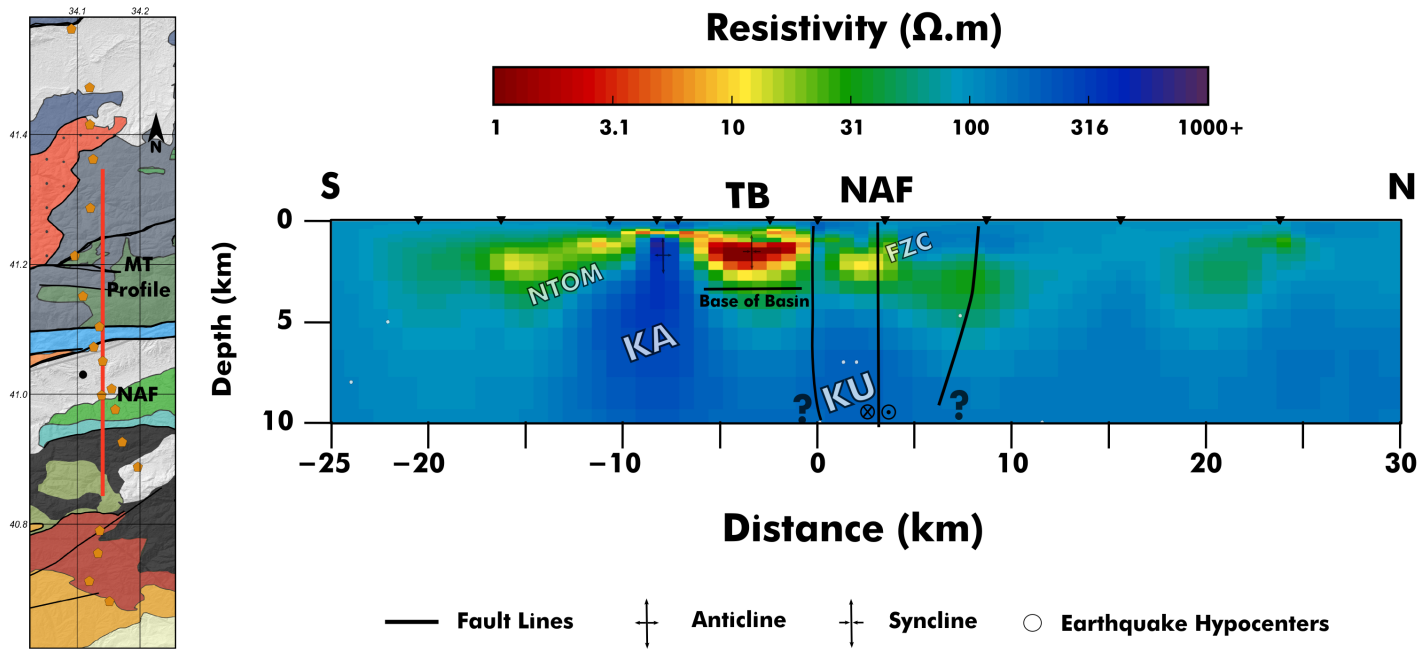


Figure 6.3. Cross-sections of the NAF model passing through model center. FZC: Fault Zone Conductor, KA: Kösdağ Arc, KU: Kunduz Unit, TB: Tosya Basin, NTOM: Neo-Tethyan Ophiolitic Melange. Logarithmic scale was used for the colorbar. White dots represent the earthquake hypocenters taken from the ISC catalogue.

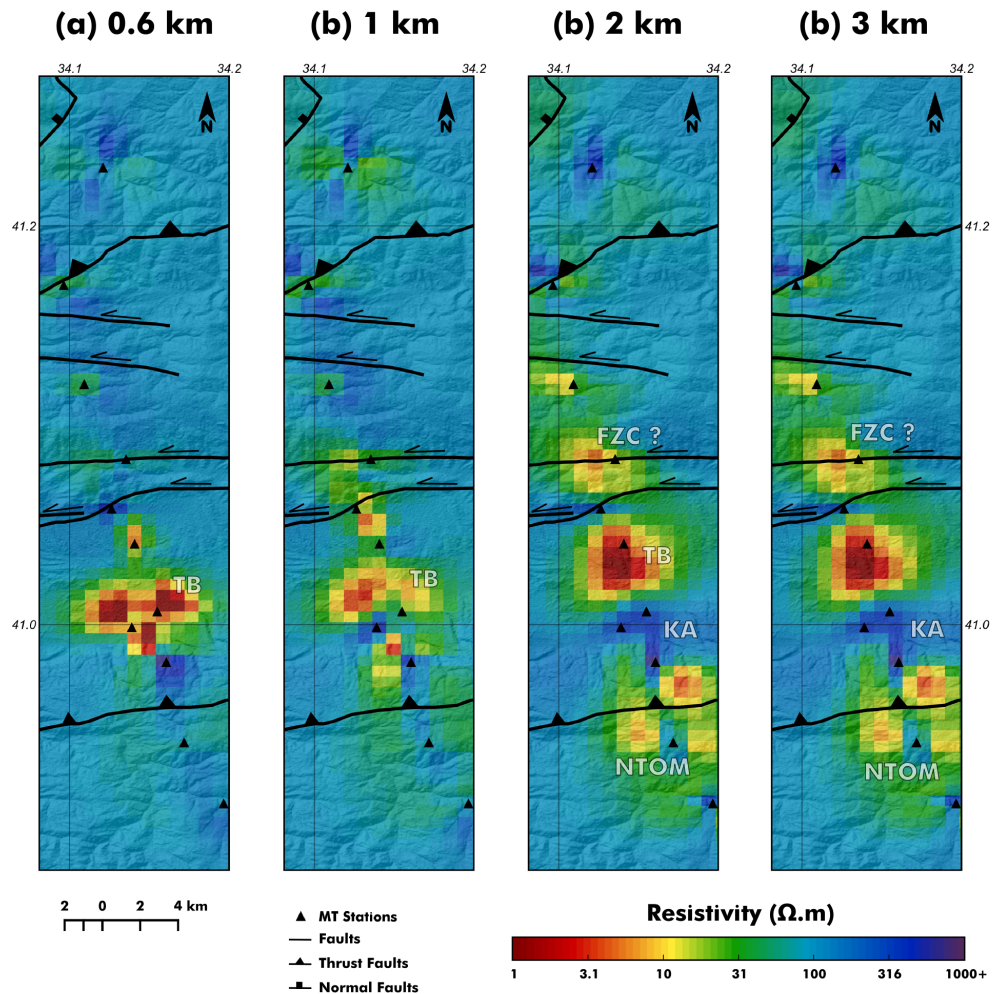


Figure 6.4. Map view of regional resistivity model for depth slices (a) 0.6 km, (b) 1 km, (c) 2 km, (d) 3 km. FZC: Fault Zone Conductor, KA: Kösdağ Arc, KU: Kunduz Unit, NTO: Neo-Tethyan Ophiolites, NTOM: Neo-Tethyan Ophiolitic Melange. Logarithmic scale was used for the colorbar. White dots represent the earthquake hypocenters taken from the ISC catalogue.

In the NAF model, conductive anomalies that resemble fault zone conductors (FZC) around the NAF, coincides well with the spatial positions of the main strand and subsidiary fault systems (Figure 6.3,4). Porosity and pore-fluid interconnectivity of the fault zones at shallow depths can be investigated with Archie's law (1942) (6.1):

$$\rho_r = \rho_f \kappa^{-m_c}, \quad (6.1)$$

where κ is the porosity value and m_c is the cementation factor. ρ_r and ρ_f are resistivity values of the anomaly and pore fluid, respectively. For values closer to $m_c = 1$, more pore-fluid interconnectivity with fractured environment should be at place, whereas values near $m_c = 2$ indicates poor connectivity between the pore fluids. Implementing Archie's Law with resistivity values of $\sim 12 \Omega m$ observed at the main fault zone conductor and taking ρ_f value as $0.3 \Omega m$ representing saline fluids; porosity within the area is calculated to be in an approximate range of 2.4-16%. Because fracture alignments and interconnected pore systems should develop along the faults orientation, values closer to $m_c = 1$ should refer to more realistic measurements for this particular zone.

6.2. Resistivity Structure of Çankırı Region

The southern side of the İEAS is dominated by a buried thrust belt, which is also cut by dextral sense faults (Kaymakçı et al., 2010). The thrust faults within the area was depicted with northwardly dipping resistive-conductive interfaces. Furthermore, conductive feature denoted as C_1 in Figure 6.2b, possibly corresponds to southwards extension of NTOM and overlying pelagic sediments, following the descriptions of Kaymakçı et al. (2009). Southernmost end of C_1 anomaly refers to İncik Formation (İF), which was seemingly ascended through this thrusting regime and eroded, while footwall-counterpart exists as a much thicker conductive feature. Above C_1 , volcanic unit Yaylaçayı Formation (YF) is visible as a resistive feature, over-thrusting the whole sequence.

Çankırı Basin matches with heterogeneously distributed conductive features, which are located south of the thrust belt. Beneath the Çankırı Basin, there is an explicitly conductive anomaly (C_2) indicating a fluid-bearing area that coincides with a zone of low Bouguer anomaly values (Kaymakçı et al., 2010). Resistive-conductive interface,

situated just north of the C_2 , is compatible with earthquake projections, thus points out a suitable position for the Kızılırmak Fault (KF). Moreover, the projected hypocenters distributed around C_2 anomaly supports the idea that earthquakes should concentrate on the resistive sides of the fault-interfaces (Gürer and Bayrak, 2007). This situation advocates that C_2 have a rheologically sound response in the area. Additionally, Kaymakçı et al. (2010) points out the existence of salt domes in the area. Under normal conditions, salt domes appear as resistive bodies (100 - 150 Ωm). However, they are hard to resolve without any additional information because of the masking effect caused by the surrounding conductive sedimentary structures (Avdeeva et al., 2012).

6.3. Resistivity Structure of the Pontic Terrane

In the northern side of the NAF, CPS appears as a downward convex shaped resistive feature (Figure 6.1b). The upper portion of CPS ($< 5 km$) is made up of relatively heterogeneous and conductive features, while these features merge in a resistive body at depth. Beneath the surface trace of Pontide Magmatic Arc and Küre Complex, the crustal structure depicted as large resistive zone extending to very end of the model, pointing out the crustal thickening in the region (Espurt et al., 2014; Okay et al., 2017). This property was also visible in seismic tomography studies (Mutlu and Karabulut, 2011; Tezel et al., 2013) where high Bouguer anomaly values were also observed (Figure 6.1a, Ateş et al., 1999). Southern portion of Çangaldağ Complex (ÇGC) appears as a highly resistive body at the tip of CPS. Beneath the northern surface trace of the complex, there is an unexpectedly large conductive feature, denoted as C_3 (Figures 6.1b, 6.2). Sensitivity tests confirm the location of this conductive anomaly. Furthermore, the results of the sensitivity tests here show that beneath 16.3 km (the depth of the last sensitivity experiment), resistivity structure was rather poorly resolved (Figure 5.7).

Existence of a large conductive zone similar to C_3 in the mid-crustal depths in active tectonic settings usually associated with the aqueous saline fluids or partial melts (Unsworth, 2010). The most recent active source for a direct partial melt emplacement in this area can be addressed via Neo-Tethyan arc-magmatism. However, this proposition is highly unlikely to occur because the active magmatism in the Pontides was

largely considered to be terminated in Late-Cretaceous (Okay et al., 2013). In addition, The heat flow variations in the area are not in favor of this option with average values of 60 mW/m^2 (Tezcan, 1995) and more importantly do not show an anomalous feature. Maden (2009) also found that the heat flow gradually decreases towards to the Pontide Arc, whereas in active convergent boundaries, heat flow may exhibit values much over 100 mW/m^2 (Tanaka et al., 2004; Springer and Förster, 1998). There are areas that exhibit partial melt zones presented with high heat flow and low resistivity regions in Tibet (Francheteau et al., 1984; Unsworth et al., 2005) and in Eastern Anatolia (Tezcan, 1995; Türkoğlu et al., 2008).

Aqueous fluids, on the other hand, is another option for this crustal range. Similar kind of large zones of fluid-filled structures were detected by earlier MT studies (Becken et al., 2011; Wannamaker et al., 2002; Ogawa et al., 2001; Jones et al., 1987, Lemonnier et al., 1999). MT data governed in this study do not reach enough depth resolution to give out such information about the source of the fluid and there are no studies directly pointing out to this feature for the sake of making a comparison on the matter. However, one can still develop a scenario within the geological and geophysical context of the area.

A possible explanation for a fluid source is prograde metamorphism. Prograde metamorphism reactions occur in specific thermodynamic conditions for different minerals. It can be seen in rapidly thickened lithospheric conditions (Unsworth et al., 2005; Wannamaker et al., 2002; Bertrand et al., 2009) or more complex thermodynamic states like dehydration of fore-arc mantle wedges (Hyndman and Peacock, 2003). Effects of Eocene to recent thickening is visible within the Pontic Range (Yıldırım et al., 2011; Cavazza et al., 2012; Espurt et al., 2014). Dehydration of serpentized mantle wedge appears as an attractive explanation, because the conductive feature positioned beneath the fore-arc region.

During the subduction processes, serpentization of the fore-arc upper mantle occurs via hydration of the mafic minerals when the excess fluid of subducting slab reaches to the mantle wedge (Hyndman and Peacock, 2003). Serpentine minerals can

sustain water up to 10-13 % (Iwamori, 1998). If the stable conditions for fluid bearing serpentinite wedge was surpassed, upwards fluid flux to the crustal levels should be observed. This may occur when the ridge subduction or opening of a slab window change the thermal conditions of serpentinite-rich fore-arc mantle (Hyndman and Peacock, 2003). Black Sea Back-arc and Pontide Fore-arc basins undergo extension from Cretaceous to Paleocene. Espurt et al. (2014) suggest that the extension in these basins have coeval existence with the emplacement of Domuzdağ Complex, in which both of the mechanisms were caused by Neo-Tethyan slab retreat. Evidences of the slab-retreat in the area suggested by ultrapotassic volcanic rocks found outside the borders of CPS (Gülmez et al., 2016). The opening of the lithospheric window accompanied by the southward slab-retreat may have caused the dehydration of mantle serpentinite and migration of metamorphic fluids to the crustal depths beneath the Pontide Fore-arc.

Entrapment of fluids in the crust is a complicated process and requires certain pressure-temperature conditions (Jones, 1987). These conditions generally meet near the brittle-ductile transition (Jiracek et al., 2007) and cause the lower-crust to appear conductive in the MT measurements (Jones, 1987). So, the conductive feature C_3 on our models, might have an entrapped source in the unresolved lower crust in this study. Additionally, existence of fluid in the region may cause low-temperature partial melting at $650^{\circ}C$. In earlier studies, similar sources for fluid-filled zones were observed at western NAF (Tank et al., 2005; Kaya, 2007; Kaya et al., 2013). Figuring out the source of these fluid bearing zones might elucidate the tectonic processes in post-collisional environment of the area and the NAF.

All the evolutionary theories aside, this upwelling conductive feature (C_3) could enhance crustal weakness, defining the seismic nature of the area. Due to its position, presence of this unit is particularly significant for the seismicity of the Ekinveren Fault. Because of the profile based measurement of MT data, it remains ambiguous whether this conductive zone is elongated within the fore-arc region or only localized in the measured area. More comprehensive investigation is clearly needed for the sole reason of its capacity to induce hypotheses regarding the geological evolution and active tectonic state of the region. For future investigations, more densely structured wide-band and

long-period MT data coverage in the region should be implemented to address the rheological attributes of the lower-crust in the region with a more holistic manner, which should have important implications on seismic heterogeneity along the NAF. The sketch representing the findings of this study is drawn in Figure 6.5.

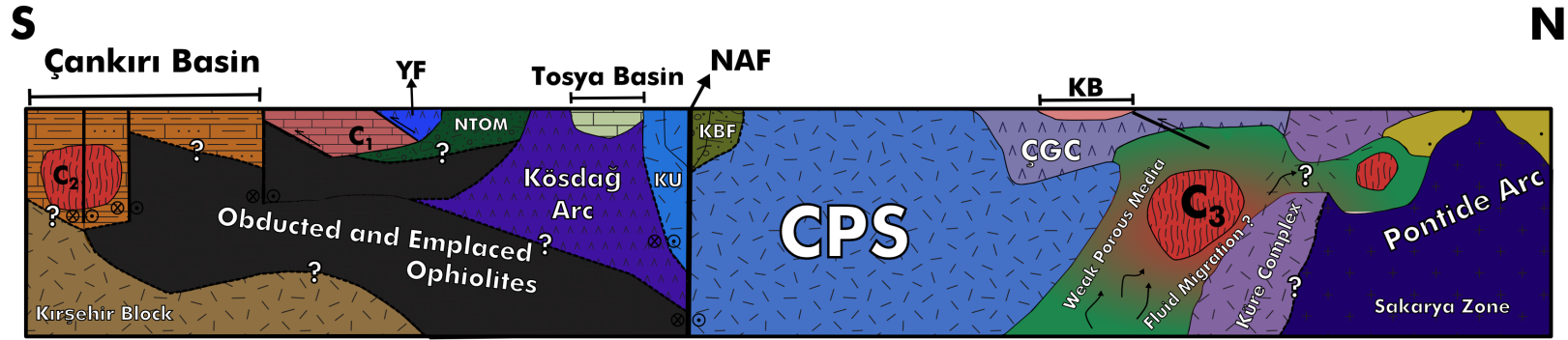


Figure 6.5. Simplified geological sketch of the area interpreted from MT resistivity models. Dashed lines indicate the borders solely based on qualitative interpretation of the MT results. CPS: Central Pontide Supercomplex, ÇGC: Çangaldağ Complex, KU: Kunduz Unit, KB: Kastamonu Basin, KBF: Kirazbaşı Formation, NAF: North Anatolian Fault, NTOM: Neo-Tethyan Ophiolitic Melange, YF: Yapraklı Formation

7. CONCLUSION

Magnetotelluric (MT) data analysis and 3-D modeling were carried out by using 25 wide-band MT stations to investigate the crustal structure along Central Pontides, İzmir-Ankara-Erzincan Suture Zone and Çankırı Basin. The NAF was depicted as a sharp resistivity contrast, while both side of the fault made up by mechanically strong and electrically resistive units. Appearance of resistive structures correlate well with relative lack of seismicity and deep locking depth, because they can not establish an interconnected pore structure thus block the fluid transport to the fault zone.

The resistive zone south of the NAF is interpreted as obducted and emplaced ophiolites collided with the Köşdağ Arc, constituting a basement for the suture zone and possibly northern part of Çankırı Basin. Tosya Basin depicted as a conductive syncline which its basement should be in between 3.6 - 4.3 km. The NAF and nearby subsidiary fault structures coincides well with conductive features within the area.

The south of the suture zone was depicted as a thrust belt indicated by contact of conductive and resistive units before entering the Neogene units of Çankırı Basin. Beneath Çankırı Basin, there appears a conductive region interrupted by resistive interfaces, which may be related to salt domes or tectonic shifting related to Kızılırmak Fault Zone. Conductive feature (C_2) and earthquake hypocenters coincides well with the resistivity variations and most accurately with the resistive-conductive interfaces indicating a fault zone in the region.

CPS was captured as a reverse convex structure which show moderate resistivity values (30-100 Ω m) for the first 5 km, than meet in a resistive body ($> 100 \Omega$ m) at depth. In the north tip of the CPS, Çangaldağ Complex appear as a resistive structure. Beneath the Çangaldağ Complex there is an unexpected conductive upwelling anomaly, which its source is not clear. Interpretation of this fluid may infer to several discussions about the geological evolution of the area. Additionally, this zone should have implications on the seismic nature in Central Pontides because of its capacity to

alter the rheological environment.

REFERENCES

Ambraseys N. N. N., C. F. Finkel, "Seismicity of Turkey and Adjacent Areas: A Historical Review, 1500-1800", Eren İstanbul", 240 pp, 1995.

Advokaat, E. L., D. J. J. van Hinsbergen, N. Kaymakçı, R. L. M. Vissers, B. W. H. Hendriks, "Late Cretaceous extension and Palaeogene rotation-related contraction in Central Anatolia recorded in the Ayhan-Büyükkişla basin.", *International Geology Review*, Vol. 56, No. 5, pp. 1813-1835, 2014. Al-Lazki, A. I., D. Seber, E. Sandvol, N. Türkelli, R. Mohammad, and R. Barazangi, "Tomographic Pn velocity and anisotropy structure beneath the Anatolian plateau (eastern Turkey) and the surrounding regions", *Geophysical Research Letters* Vol. 30, No. 24, 2003.

Archie, G. E., "The electrical resistivity log as an aid in determining some reservoir characteristics", *Transactions of the AIME*, Vol. 146, No.1, pp. 54-62, 1942.

Ateş, A., P. Kearey, S. Tufan, "New gravity and magnetic anomaly maps of Turkey.", *Geophysical Journal International*, Vol. 136, No.2, pp. 499-502, 1999.

Avdeev, D. B., "Three-dimensional electromagnetic modelling and inversion from theory to application", *Surveys in Geophysics*, Vol. 26, No. 6, pp. 767-799, 2005.

Avdeeva, A., D. Avdeev, M. Jegen, "Detecting a salt dome overhang with magnetotellurics: 3D inversion methodology and synthetic model studies", *Geophysics*, Vol. 77, No. 4, pp. 251-263, 2012.

Aygül, M., A. I. Okay, R. Oberhansli, A. Schmidt, M. Sudo, "Late Cretaceous infant intra-oceanic arc volcanism, the Central Pontides, Turkey: Petrogenetic and tectonic implications.", *Journal of Asian Earth Sciences*, Vol. 111, pp. 312-327, 2015.

Aygül. M., A. I. Okay, R. Oberhansli, M. Sudo, "Pre-collisional accretionary growth

of the southern Laurasian active margin, Central Pontides, Turkey.”, *Tectonophysics*, Vol. 671, pp. 218-234, 2016.

Barka, A., H. S. Akyüz, H. A. Cohen, F. Watchorn, ”Tectonic evolution of the Niksar and Tasova–Erbaa pull-apart basins, North Anatolian Fault Zone: their significance for the motion of the Anatolian block.”, *Tectonophysics*, Vol. 322, No. 3, pp. 243-264, 2000.

Bertrand, E., M. Unsworth, C. W. Chiang, C. S. Chen, C. C. Chen, F. Wu, E. Türkoğlu, H. Hsu, G. Hill, ”Magnetotelluric evidence for thick-skinned tectonics in central Taiwan”, *Geology*, Vol. 37, No. 8, pp. 711-714, 2009.

Becken, M., O. Ritter, P. A. Bedrosian, U. Weckmann, ”Correlation between deep fluids, tremor and creep along the central San Andreas fault.”, *Nature*, Vol. 480, pp. 87-92, 2011.

Becken, M., O. Ritter, ”Magnetotelluric studies at the San Andreas Fault Zone: implications for the role of fluids.”, *Surveys in Geophysics*, Vol. 33, No. 1, pp. 65-105, 2012.

Bedrosian, P. A., M. J. Unsworth, G. Egbert, ”Magnetotelluric imaging of the creeping segment of the San Andreas Fault near Hollister.”, *Geophysical Research Letters*, Vol. 29, No. 11, 2002.

Bedrosian, P. A., M. J. Unsworth, G. D. Egbert, C. H. Thurber, ”Geophysical images of the creeping segment of the San Andreas fault: implications for the role of crustal fluids in the earthquake process.”, *Tectonophysics*, Vol. 385, No. 1, pp. 137-158, 2004.

Bekin, E., ”The Magnetotelluric Phase Tensor Method for Imaging The North Anatolian Fault Zone.”, M.Sc. Thesis, Boğaziçi University, 2016.

Bellier, O., S. Över, A. Poisson, J. Andrieux, "Recent temporal change in the stress state and modern stress field along the North Anatolian Fault Zone (Turkey).", *Geophysical Journal International*, Vol. 131, No. 1, pp. 61-86, 1997.

Bibby, H. M., "Analysis of multiple-source bipole-dipole resistivity surveys using the apparent resistivity tensor", *Geophysics*, Vol. 51, No. 4, pp. 972-983, 1986.

Bibby, H. M., T. G. Caldwell and C. Brown, "Determinable and non-determinable parameters of galvanic distortion in magnetotellurics", *Geophysical Journal International*, Vol. 164, No.3 , pp. 915-930, 2005.

Booker, J. R., "The Magnetotelluric Phase Tensor: A Critical Review", *Surv Geophys*, Vol. 35, No. 1, pp. 7-40, 2014.

Bulut, F., M. Bohnhoff, L. W. Ellsworth, M. Aktar, G. Dresen, "Microseismicity at the North Anatolian fault in the Sea of Marmara offshore Istanbul, NW Turkey.", *Journal of Geophysical Research: Solid Earth*, Vol. 114, No. B19, 2009.

Bürgmann, R., G. Dresen, "Rheology of the lower crust and upper mantle: Evidence from rock mechanics, geodesy, and field observations.", *Annual Review of Earth and Planetary Sciences*, Vol. 36, 2008.

Cagniard, L., "Basic theory of the magneto-telluric method of geophysical prospecting" *Geophysics* Vol 18. No:3 (1953): pp. 605-635, 1953.

Caldwell, T. G., H. M. Bibby and C. Brown, "The magnetotelluric phase tensor", *Geophysical Journal International*, Vol. 158, No.2, pp. 457-469, 2004.

Cavazza, W. , A. I. Okay, and M. Zattin, "Rapid early-middle Miocene exhumation of the Kazdağ Massif (western Anatolia)", *International Journal of Earth Sciences*, Vol.

98, No. 8, pp. 1935-1947, 2009.

Cavazza, W., I. Federici, A. I. Okay, M. Zattin, "Apatite fission-track thermochronology of the Western Pontides (NW Turkey).", *Geological Magazine*, Vol. 149, No.1, pp. 133-140, 2012.

Chave, A. D., A. G. Jones, "The Magnetotelluric Method", *Cambridge University Press*, ISBN: 978-0-521-81927-5, 2012.

Constable, S. C., R. L. Parker, and C. G. Constable, "Occam's inversion: A practical algorithm for generating smooth models from electromagnetic sounding data", *Geophysics*, Vol. 52, No. 3, pp. 289-300, 1987.

Çakır, Z., A. M. Akoğlu, S. Balabbes, S. Ergintav, M. Meghraoui, "Creeping along the Ismetpasa section of the North Anatolian fault (Western Turkey): Rate and extent from InSAR.", *Earth and Planetary Science Letters*, Vol. 238, No. 1, pp. 225-234, 2005.

Egbert, G. D., and A. Kelbert, "Computational recipes for electromagnetic inverse problems", *Geophysical Journal International*, Vol. 189, No.1, pp. 251-267, 2012.

Ergintav, S., R. E. Reilinger, R. Çakmak, M. Floyd, Z. Çakır, U. Doğan, R. W. King, S. McClusky, H. Özener, "Istanbul's earthquake hot spots: Geodetic constraints on strain accumulation along faults in the Marmara seismic gap", *Geophysical Research Letters*, Vol. 41, No. 16, pp. 5783-5788, 2014.

Espurt, N., J. C. Hippolyte, N. Kaymakçı, E. Sangu, "Lithospheric structural control on inversion of the southern margin of the Black Sea Basin, Central Pontides, Turkey." *Lithosphere*, Vol.6, No.1, pp. 26-34, 2014.

Egbert, G. D., "Robust multiple-station magnetotelluric data processing.", *Geophysi-*

cal Journal International, Vol. 130, No. 2, pp. 475-496, 1997.

Fulton, P. M., D. M. Saffer, "Potential role of mantle-derived fluids in weakening the San Andreas Fault.", *Journal of Geophysical Research: Solid Earth*, Vol. 114, No. B7, 2009.

Groom, R. W. and R. C. Bailey, "Decomposition of magnetotelluric impedance tensors in presence of local three-dimensional galvanic distortion", *Journal of Geophysical Research: Solid Earth*, Vol. 94.B2, pp. 1913-1925, 1989.

Francheteau, J., C. Jaupart, S. X. Jie, K. Wen-Hua, L. De-Lu, B. Jia-Chi, W. Hung-Pin, D. Hsia-Yeu, "High heat flow in southern Tibet", *Nature*, Vol. 307, pp. 32-36, 1984.

Gamble, T. D., W. M. Goubau, J. Clarke, "Magnetotellurics with a remote magnetic reference.", *Geophysics*, Vol. 44, No. 1, pp. 53-68, 1979.

Gürer, A., M. Bayrak, "Relation between electrical resistivity and earthquake generation in the crust of West Anatolia, Turkey", *Tectonophysics*, Vol. 445, pp. 49-65, 2007.

Goto, T. N., Y. Wada, N. Oshiman, N. Sumitomo, "Resistivity structure of a seismic gap along the Atotsugawa Fault, Japan.", *Physics of the Earth and Planetary Interiors* Vol. 148, No.1, pp. 55-72, 2005. Gülmez, F., Ş. C. Genç, D. Prelevic, O. Tüysüz, Z. Karacık, M. F. Roden, Z. Billor, "Ultrapotassic Volcanism from the Waning Stage of the Neotethyan Subduction: a Key Study from the Izmir–Ankara–Erzincan Suture Belt, Central Northern Turkey." *Journal of Petrology*, Vol.57, No.3, pp. 561-593, 2016.

Hadamard, M. I., "On problems in partial derivatives, and their physical significance", *Princeton University Bulletin*, Vol. 13, pp. 82-88, 1902.

Hartleb, R. D., J. F. Dolan, H. S. Akyüz, B. Yerli, "A 2000-year-long paleoseismologic record of earthquakes along the central North Anatolian fault, from trenches at Alayurt, Turkey.", *Bulletin of the Seismological Society of America*, Vol. 93, No. 5, pp. 1935-1954, 2003.

Heise W., T. G. Caldwell, H. M. Bibby, C. Brown, "Anisotropy and phase splits in magnetotellurics.", *Physics of the Earth and Planetary Interiors*, Vol. 158, No. 2, pp. 107-121, 2006.

Hubert-Ferrari, A., R. Armijo, G. King, B. Meyer, A. Barka, "Morphology, displacement, and slip rates along the North Anatolian Fault, Turkey.", *Journal of Geophysical Research: Solid Earth*, Vol. 107, 2002.

Hickman, S., R. Sibson, R. Bruhn, "Introduction to special section: Mechanical involvement of fluids in faulting.", *Journal of Geophysical Research: Solid Earth*, Vol. 100, pp. 12831-12840, 1995.

Hippolyte, J-C., N. Espurt, N. Kaymakçı, E. Sangu, C. Müller, "Cross-sectional anatomy and geodynamic evolution of the Central Pontide orogenic belt (northern Turkey)." *International Journal of Earth Sciences*, Vol.105, No. 1, pp. 81-106, 2016.

Hyndman, R. D., S. M. Peacock, "Serpentinization of the forearc mantle." *Earth and Planetary Science Letters*, Vol.212, No.3, pp. 417-432, 2003.

Irwin, W. P, I. Barnes, "Effect of geologic structure and metamorphic fluids on seismic behavior of the San Andreas fault system in central and northern California.", *Geology*, Vol. 3, No. 2, pp. 713-716, 1975.

Iwamori, H, "Transportation of H₂O and melting in subduction zones.", *Earth and Planetary Science Letters*, Vol.160, No.1, pp. 65-80, 1998.

Jiracek, G. R., V. M. Gonzalez, T. G. Caldwell, P. E. Wannamaker, D. Kilb, "Seismogenic, Electrically Conductive, and Fluid Zones at Continental Plate Boundaries in New Zealand, Himalaya, and California, USA", *A Continental Plate Boundary: Tectonics at South Island, New Zealand*, pp. 347-369, 2007.

Jones, A. G., "MT and reflection: an essential combination." *Geophysical Journal International* Vol.89, No.1, pp. 7-18, 1987.

Jolivet, L., "A comparison of geodetic and finite strain pattern in the Aegean, geodynamic implications", *Earth and Planetary Science Letters*, Vol. 187, pp. 95-104, 2001.

Kaufman, A. A. and G. V. Keller, "The Magnetotelluric Sounding Method", *Methods in geochemistry and geophysics*, vol. 15, 1981.

Ketin, İ., "Ketin, I. (1948). Über die tektonisch-mechanischen Folgerungen aus den grossen anatolischen Erdbeben des letzten Dezenniums", *Geologische Rundschau*, Vol. 36, No.1, pp. 77-83, 1948.

Karaş, M., S. B. Tank, S. Özaydın, "Electrical conductivity of a locked fault: investigation of the Ganos segment of the North Anatolian Fault using three-dimensional magnetotellurics." *Earth, Planets and Space* Vol. 69, No. 1 pp. 107, 2017.

Kaya, C., "Deep crustal structure of northwestern part of Turkey.", *Tectonophysics*, Vol. 481, No.1, pp. 227-239, 2010.

Kaya, T., T. Kasaya, S.B. Tank, Y. Ogawa, M. K. Tunçer, N. Oshiman, Y. Honkura, M. Matsushima, "Electrical characterization of the North Anatolian Fault Zone underneath the Marmara Sea, Turkey by ocean bottom magnetotellurics", *Geophysical Journal International*, Vol. 193, No.2 ,pp. 664, 2013.

Kaymakçı, N., Y. Özçelik, S. H. White, P. M. Van Dijk, "Tectono-stratigraphy of the Çankırı Basin: late Cretaceous to early Miocene evolution of the Neotethyan suture zone in Turkey.", *Geological Society, London, Special Publication*, Vol. 311, No.1, pp. 67-106, 2009.

Kaymakçı, N., Özmutlu, Ş., P. M. Van Dijk, Y. Özçelik, "Surface and subsurface characteristics of the Çankırı Basin (Central Anatolia, Turkey): Integration of remote sensing, seismic interpretation and gravity.", *Turkish Journal of Earth Sciences*, Vol. 19, No. 1, pp. 79-100, 2010.

Kelbert, A., N. Meqbel, G. D. Egbert, K. Tandon, "ModEM: a modular system for inversion of electromagnetic geophysical data", *Computers & Geosciences*, Vol. 66, pp. 40-53, 2014.

Kiyan, D., A. G. Jones, J. Vozar, "The inability of magnetotelluric off-diagonal impedance tensor elements to sense oblique conductors in three-dimensional inversion", *Geophysical Journal International*, Vol. 196, No. 3, pp. 1351-1364, 2013.

Krieger, L., J. R. Peacock, "MTPy: A Python toolbox for magnetotellurics.", *Computers & Geosciences*, Vol. 72, pp. 167-175.

Ledo, J., "2-D versus 3-D magnetotelluric data interpretation.", *Surveys in Geophysics*, Vol. 26, No. 5, pp. 511-543, 2005.

Lemmonnier, C., G. Marquis, F. Perrier, J-P. Avouac, G. Chitrakar, B. Kafle, S. Sapkota, U. Gautam, D. Tiwari, M. Bano, "Electrical structure of the Himalaya of Central Nepal: high conductivity around the mid-crustal ramp along the MHT", *Geophysical Research Letters*, Vol. 26, No. 21, pp. 3261-3264, 1999.

Madden, T. and P. Nelson, "A defense of Cagniard's magnetotelluric method", *ONR Report, MIT Geophysics Lab*, 1964.

Maden, N., "Crustal Thermal Properties of the Central Pontides (Northern Turkey) Deduced from Spectral Analysis of Magnetic Data", *Turkish Journal of Earth Sciences*, Vol. 18, pp. 383-392, 2009.

McClusky S., S. Balassanian, A. Barka, C. Demir, S. Ergintav, I. Georgiev, O. Gurkan, M. Hamburger, K. Hurst, H. Kahle, K. Kasten, G. Kekelidze, R. W. King, V. Kotzev, O. Lenk, S. Mahmoud, A. Mishin, M. Nadariya, A. Ouzoumis, D. Paradissis, Y. Peter, M. Prilepin, R. Reilinger, I. Sanli, H. Seeger, A. Tealeb, M. N. Toksöz, G. Veis, "Global Positioning System constraints on plate kinematics and dynamics in the eastern Mediterranean and Caucasus", *Journal of Geophysical Research*, Vol. 105, No. B3, pp. 5695-5719, 2000.

McKenzie, D., "Active tectonics of the Mediterranean region", *Geophysical Journal International*, Vol. 30, No. 2, pp. 109-185, 1972.

Meqbel, N. M., G. D. Egbert, P. E. Wannamaker, A. Kelbert, A. Schultz, "Deep electrical resistivity structure of the northwestern US derived from 3-D inversion of USArray magnetotelluric data.", *Earth and Planetary Science Letters*, Vol. 402, pp. 290-304, 2014.

Meqbel, N. M., U. Weckmann, G. Munoz, O. Ritter, "Crustal metamorphic fluid flux beneath the Dead Sea Basin: constraints from 2-D and 3-D magnetotelluric modelling.", *Geophysical Supplements to the Monthly Notices of the Royal Astronomical Society*, Vol. 207, No. 3, pp. 1609-1629, 2016.

Mutlu, A. K., H. Karabulut, "Anisotropic Pn tomography of Turkey and adjacent regions", *Geophysical Journal International*, Vol. 187, No. 3, pp. 1743-1758, 2011.

Ogawa, Y., M. Mishina, T. Goto, H. Satoh, N. Oshiman, T. Kasaya, Y. Takahashi, T. Nishitani, S. Sakanaka, M. Uyeshima, Y. Takahashi, Y. Honkura, M. Matsushima,

"Magnetotelluric imaging of fluids in intraplate earthquake zones, NE Japan back arc.", *Geophysical Research Letters*, Vol. 28, No. 19, pp. 3741-3744, 2001.

Okay, A. I., and O. Tüysüz, "Tethyan sutures of northern Turkey", *Geological Society, London, Special Publications*, Vol. 156, No.1, pp. 475-515, 1999.

Okay, A. I., and M. C. Göncüoğlu, "The Karakaya Complex: a review of data and concepts", *Turkish Journal of Earth Sciences*, Vol. 13, No.2, pp. 75-95, 2004.

Okay, A. I., O. Tüysüz, M. Satır, S. Özkan-Altıner, D. Altıner, S. Sherlock, and R. H. Eren, "Cretaceous and Triassic subduction-accretion, high-pressure-low-temperature metamorphism, and continental growth in the Central Pontides, Turkey", *Geological Society of America Bulletin*, Vol. 118, No. 9-10, pp. 1247-1269, 2006.

The Uludağ Massif, northwest Turkey—Implications for the westward translation of Anatolia", *Geological Society of America Bulletin*, Vol. 120, No. 7-8, pp. 893-911, 2008a.

Okay, A. I., E. Bozkurt, M. Satır, E. Yiğitbaş, Q. G. Crowley, and C. K. Shang, "Defining the southern margin of Avalonia in the Pontides: Geochronological data from the Late Proterozoic and Ordovician granitoids from NW Turkey", *Tectonophysics*, Vol. 461, No.1, pp. 252-264, 2008b.

Okay, A. I., M. Satır, M. Zattin, W. Cavazza, G. Topuz, "An Oligocene ductile strike-slip shear zone: Okay, A. I., "Geology of Turkey: a synopsis", *Anschnitt*, Vol. 21, pp. 19-42, 2008c.

Okay, A. I., G. Sunal, S. Sherlock, D. Altıner, O. Tüysüz, A. R. Kylander-Clark, M. Aygül, "Early Cretaceous sedimentation and orogeny on the active margin of Eurasia: Southern Central Pontides, Turkey.", *Tectonics*, Vol. 32, no. 5, pp. 1247-1271, 2013.

Okay, A. I., D. Altiner, G. Sunal, M. Aygöl, R. Akdoğan, S. Altiner, M. Simmons, "Geological evolution of the Central Pontides.", *Geological Society, London, Special Publications*, Vol. 464, No.3, 2017.

Parsons, T., S. Toda, R. S. Stein, A. Barka, J. H. Dieterich, "Heightened Odds of Large Earthquakes Near Istanbul, An Interaction-Based Probability Calculation", Vol. 288, pp. 661-665.

Patro, P. K., G. D. Egbert, "Application of 3D inversion to magnetotelluric profile data from the Deccan Volcanic Province of Western India.", *Physics of the Earth and Planetary Interiors*, Vol. 187, No. 1, pp. 33-46, 2011.

Parkinson, W. D., "Directions of rapid geomagnetic variations", *Geophysical Journal International*, Vol 2, No. 1, pp. 1-14, 1959.

Peyret, M., F. Masson, H. Yavaşoğlu, S. Ergintav, R. Reilinger, "Present-day strain distribution across a segment of the central bend of the North Anatolian Fault Zone from a Persistent-Scatterers InSAR analysis of the ERS and Envisat archives", *Geophysical Journal International*, Vol. 192, No.3, pp. 929-945, 2012.

Rice, J. R., "Fault stress states, pore pressure distributions, and the weakness of the San Andreas fault.", *International Geophysics*, Vol. 51, pp. 475-503, 1992.

Ritter, O., A. Hoffmann-Rothe, P. A. Bedrosian, U. Weckmann, V. Haak, "Electrical conductivity images of active and fossil fault zones.", *Geological Society, London, Special Publications*, Vol. 245, No. 1, pp. 165-186, 2005.

Rikitake, T., "1. Notes on the Electromagnetic Induction within the Earth.", *Earth. Bull. Earthquake Res. Inst.*, Vol. 24, pp. 1-9, 1948.

Scholz, C. H., "The brittle-plastic transition and the depth of seismic faulting.", *Geologische Rundschau*, Vol. 77, No. 1, pp. 319-328, 1988.

Scholz, C. H., "Earthquakes and friction laws.", *Nature*, Vol. 391, pp. 37, 1998.

Siripunvaraporn, W., G. Egbert, Y. Lenbury, M. Uyeshima, "Three-dimensional magnetotelluric inversion: data-space method.", *Physics of the Earth and planetary interiors*, Vol. 150, No.1, pp. 3-14, 2005a.

Siripunvaraporn, W., G. Egbert, M. Uyeshima, "Interpretation of two-dimensional magnetotelluric profile data with three-dimensional inversion: synthetic examples.", *Geophysical Journal International*, Vol. 160, No. 3, pp. 804-814, 2005b.

Simpson, F. , K. Bahr, "Practical Magnetotellurics.", *Cambridge University Press*, 2005.

Sims , W. E., F. X. Bostick Jr., H. W. Smith, "The estimation of magnetotelluric impedance tensor elements from measured data.", *Geophysics*, Vol. 35, No. 5, pp. 938-942, 1971.

Stampfli, G. M., "Tethyan Oceans", *Geological society, london, special publications*, Vol. 173, No.1, pp. 1-23, 2000.

Reilinger, R., S. McClusky, P. Vernant, S. Lawrance, S. Ergintav, R. Çakmak, H. Özener, F. Kadirov, I. Guliev, R. Stepanyan, M. Nadariya, G. Hahubia, S. Mahmoud, K. Sakr, A. ArRaheji, D. Paradissis, A. Al-Aydrus, M. Prilepin, T. Guseva, E. Evren, A. Dmitrotsa, S. V. Filikov, F. Gomez, R. Al-Ghazzi, and G. Karam, "GPS constraints on continental deformation in the Africa-Arabia-Eurasia continental collision zone and implications for the dynamics of plate interactions", *Journal of Geophysical Research*, Vol. 111, No. B05411, 2006.

Rodi, W., R. L. Mackie, "Nonlinear conjugate gradients algorithm for 2-D magnetotelluric inversion", Vol. 66, No. 1, pp. 174-187, 2001.

Simpson, F. and K. Bahr, "Practical Magnetotellurics", *Cambridge University Press*, ISBN: 0 521 81727 7, 2005.

Sims, W. E., F. X. Bostick Jr. and H. W. Smith, "The estimation of magnetotelluric impedance tensor elements from measured data", *Geophysics*, Vol. 36, pp. 938-942, 1971.

Springer, M., A. Förster, "Heat-flow density across the Central Andean subduction zone.", *Tectonophysics*, Vol. 291, No. 1, pp. 123-139, 1998.

Stein, R. S., A. A. Barka, and J. H. Dieterich, "Progressive failure on the North Anatolian fault since 1939 by earthquake stress triggering", *Geophysical Journal International*, Vol. 128, No. 3, pp. 594-604, 1997.

Swift, C. M., "A magnetotelluric investigation of an electrical conductivity anomaly in the southwestern United States", Ph.D. Thesis, Massachusetts Institute of Technology, 1967.

Şengör, A. M. C., and Y. Yılmaz, "Tethyan evolution of Turkey: a plate tectonic approach", *Tectonophysics*, Vol. 75, No. 3-4, pp. 181-241, 1981.

Şengör, A. M. C., "Tectonics of the Tethysides: orogenic collage development in a collisional setting", *Annual Review of Earth and Planetary Sciences*, Vol. 15, No.1, pp. 213-244, 1987.

Şengör, A. M. C., S. Özeren, T. Genç, and Ekrem Zor, "East Anatolian high plateau as a mantle-supported, north-south shortened domal structure", *Geophysical Research Letters*, Vol. 30, No. 24, 2003.

Şengör, A. M. C., O. Tüysüz, C. İmren, M. Sakiñç, H. Eyidođan, N. Görür, X. Le Pichon, C. Rangin, "The North Anatolian Fault: A New Look", *Annual Reviews of Earth Planetary Sciences*, Vol. 33, pp. 37-112, 2005.

Tanaka, A., M. Yamano, Y. Yano, M. Sasada, "Geothermal gradient and heat flow data in and around Japan (I).", *Earth, planets and space*, Vol. 12, No. 12, pp. 1191-1194, 2004.

Tank, S. B., Y. Honkura, Y. Ogawa, N. Oshiman, M. Matsushima, C. Çelik, A. M. Işıkara, "Resistivity structure in the western part of the fault rupture zone associated with the 1999 Izmit earthquake and its seismogenic implication.", *Earth, planets and space*, Vol. 55, No.7, pp. 437-442, 2003.

Tank, S. B., Y. Honkura, Y. Ogawa, M. Matsushima, N. Oshiman, M. K. Tunçer, C. Çelik, E. Tolak, A. M. Işıkara, "Magnetotelluric imaging of the fault rupture area of the 1999 İzmit (Turkey) earthquake", *Physics of the Earth and Planetary Interiors*, Vol. 150, No.1, pp. 213-225, 2005.

Tank, S. B., "Fault zone conductors in Northwest Turkey inferred from audio frequency magnetotellurics", *Earth, planets and space*, Vol. 64, No. 9, pp. 729-742, 2012.

Tezcan, A. K., "Geothermal explorations and heat flow in Turkey.", *Terrestrial heat flow and geothermal energy in Asia: New Delhi*, Oxford and IBH Publishing Co., pp. 23-42, 1995. Toksöz, M. N, A. F. Shakal, and A. J. Michael, "Space-Time Migration of Earthquakes Along the North Anatolian Fault Zone and Seismic Gaps", *Earthquake Prediction and Seismicity Patterns*, Vol. 117, pp. 1258-1270, 1979.

Tietze, K., O. Ritter, "Three-dimensional magnetotelluric inversion in practice-the electrical conductivity structure of the San Andreas Fault in Central California.", *Geophysical Journal International*, Vol. 195, No. 1, pp. 130-147, 2013.

Tikhonov, A. N. "On determining electrical characteristics of the deep layers of the Earth's crust" *Doklady*. Vol. 73. No. 2., 1950.

Tikhonov, A. N. and V. I. Arsenin, "Solutions of ill-posed problems", *New York: Wiley*, 1977.

Türkoğlu, E., M. Unsworth, İ. Çağlar, V. Tuncer, and Ü. Avşar, "Lithospheric structure of the Arabia-Eurasia collision zone in eastern Anatolia: Magnetotelluric evidence for widespread weakening by fluids?", *Geology*, Vol. 36, No. 8, pp. 619-622, 2008.

Türkoğlu, E., M. Unsworth, F. Bulut, İ. Çağlar, "Crustal structure of the North Anatolian and East Anatolian Fault Systems from magnetotelluric data.", *Physics of the Earth and Planetary Interiors*, Vol. 241, pp. 1-14, 2015.

Tüysüz, O., "Geology of the Cretaceous sedimentary basins of the Western Pontides." *Geological Journal*, Vol. 34, No.1-2, pp. 75-93, 1999.

Unsworth, M. J., P. E. Malin, G. D. Egbert, J. R. Booker, "Internal structure of the San Andreas fault at Parkfield, California.", *Geology*, Vol. 25, No. 4, pp. 359-362, 1997. Unsworth, M. J., G. Egbert, J. Booker, "High-resolution electromagnetic imaging of the San Andreas fault in central California.", *Journal of Geophysical Research: Solid Earth*, Vol. 104, pp. 1131-1150, 1999.

Unsworth, M. J., P. A. Bedrosian, "On the geoelectric structure of major strike-slip fault and shear zones.", *Earth, planets and space*, Vol. 56, No.12, pp. 1177-1184, 2004.

Unsworth, M. J., A. G. Jones, W. Wei, G. Marquis, "Crustal rheology of the Himalaya and Southern Tibet inferred from magnetotelluric data.", *Nature*, Vol.438, No.7064, pp.78, 2005.

Unsworth, M. J., "Magnetotelluric studies of active continent–continent collisions." *Surveys in Geophysics*, Vol. 31, No. 2, pp. 137-161, 2010.

Ustaömer, T., A. H. F. Robertson, "Geochemical evidence used to test alternative plate tectonic models for pre-Upper Jurassic (Palaeotethyan) units in the Central Pontides." *Geological Journal*, Vol. 34, No. 1-2, pp. 25-53, 1999.

Wannamaker, P. E., G. R. Jiracek, J. A. Stodt, T. G. Caldwell, V. M. Gonzalez, J. D. McKnight, A. D. Porter, "Fluid generation and pathways beneath an active compressional orogen, the New Zealand Southern Alps, inferred from magnetotelluric data." *Journal of Geophysical Research: Solid Earth*, Vol. 107, No. B6, 2002.

Wannamaker, P. E., T. G. Caldwell, G. R. Jiracek, V. Maris, G. J. Hill, Y. Ogawa, M. H. Bibby, S. L. Bennie, W. Heise, "Fluid and deformation regime of an advancing subduction system at Marlborough, New Zealand", *Nature*, Vol. 460, pp. 733, 2009.

Wiese, H., "Geomagnetische Tiefentellurik Teil II: die Streichrichtung der Untergrundstrukturen des elektrischen Widerstandes, erschlossen aus geomagnetischen Variationen", *Pure and applied geophysics*, Vol 52, No. 1, pp. 83-103, 1962.

Wesnousky, S. G., "Predicting the endpoints of earthquake ruptures.", *Nature*, Vol. 444, pp. 358, 2006.

Yolsal-Çevikbilen, S., C. B. Biryol, S. Beck, G. Zandt, T. Taymaz, H.E. Adiyaman, A.A. Özacar, "3-D crustal structure along the North Anatolian Fault Zone in north-central Anatolia revealed by local earthquake tomography.", *Geophysical Journal International*, Vol. 188, No. 3, pp. 819-849, 2012.

Yıldırım, C., T. F., Schildengen, H. Echtler, D. Melnick, M. R. Strecker, "Late Neogene and active orogenic uplift in the Central Pontides associated with the North Anatolian Fault: implications for the northern margin of the Central Anatolian Plateau, Turkey."

Tectonics, Vol.30, No.5, 2011.

Zhao, D., O. P. Mishra, R. Sanda, "Influence of fluids and magma on earthquakes: seismological evidence", *Physics of the Earth and Planetary Interiors*, Vol. 132, pp. 249-267, 2004.

Zhdanov, M. S. and G. V. Keller, "The Geoelectrical Methods in Geophysical Exploration", *Elsevier*, ISBN: 0444896783, 9780444896780, 1994.

Zhdanov, M. S., "Geophysical Inverse Theory and Regularization Problems", *Elsevier Science*, ISBN: 9780444510891, 2002.

Zor, E., E. Sandvol, C. Gürbüz, N. Türkelli, D. Seber, and M. Barazangi, "The crustal structure of the East Anatolian plateau (Turkey) from receiver functions", *Geophysical Research Letters*, Vol. 30, No.24, 2003.

APPENDIX A : RESIDUAL MAPS OF MODELING ATTEMPTS

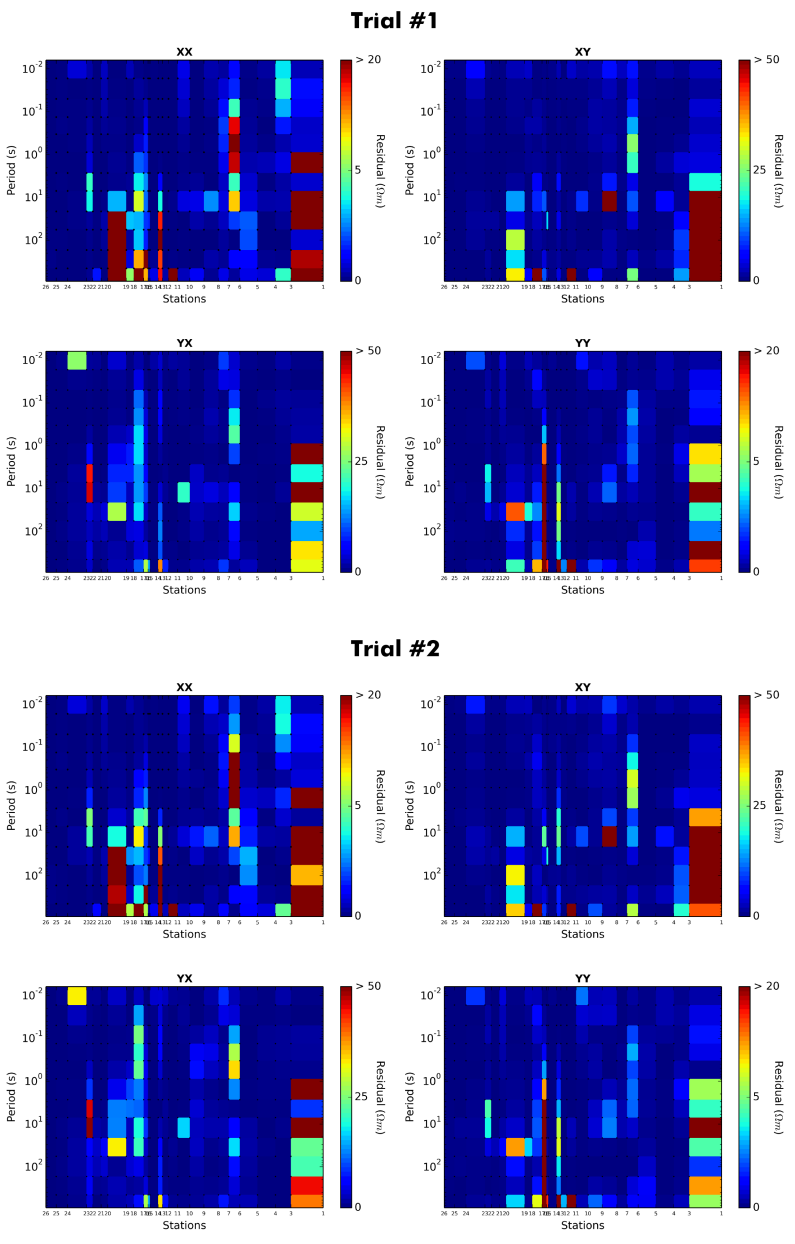


Figure 7.1. Apparent resistivity residuals of trials 1 and 2 for the four components of the impedances.

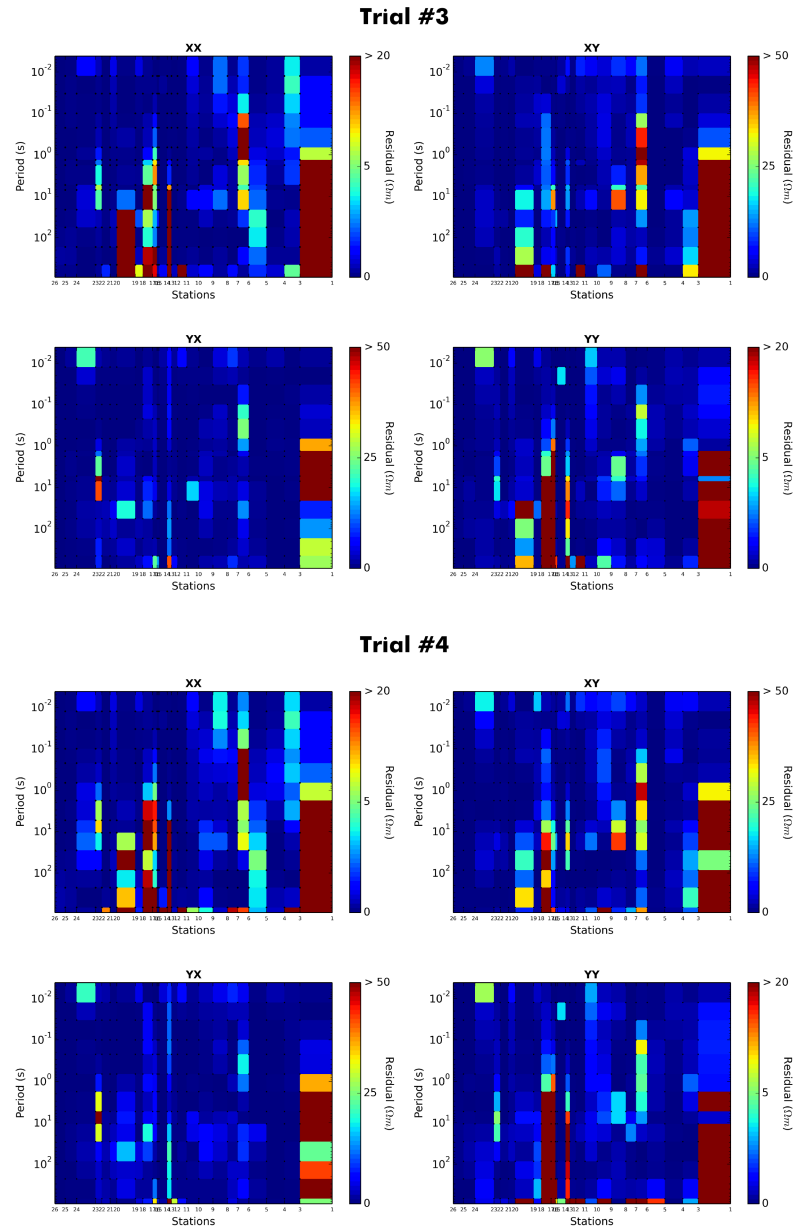


Figure 7.2. Apparent resistivity residuals of trials 1 and 2 for the four components of the impedances.

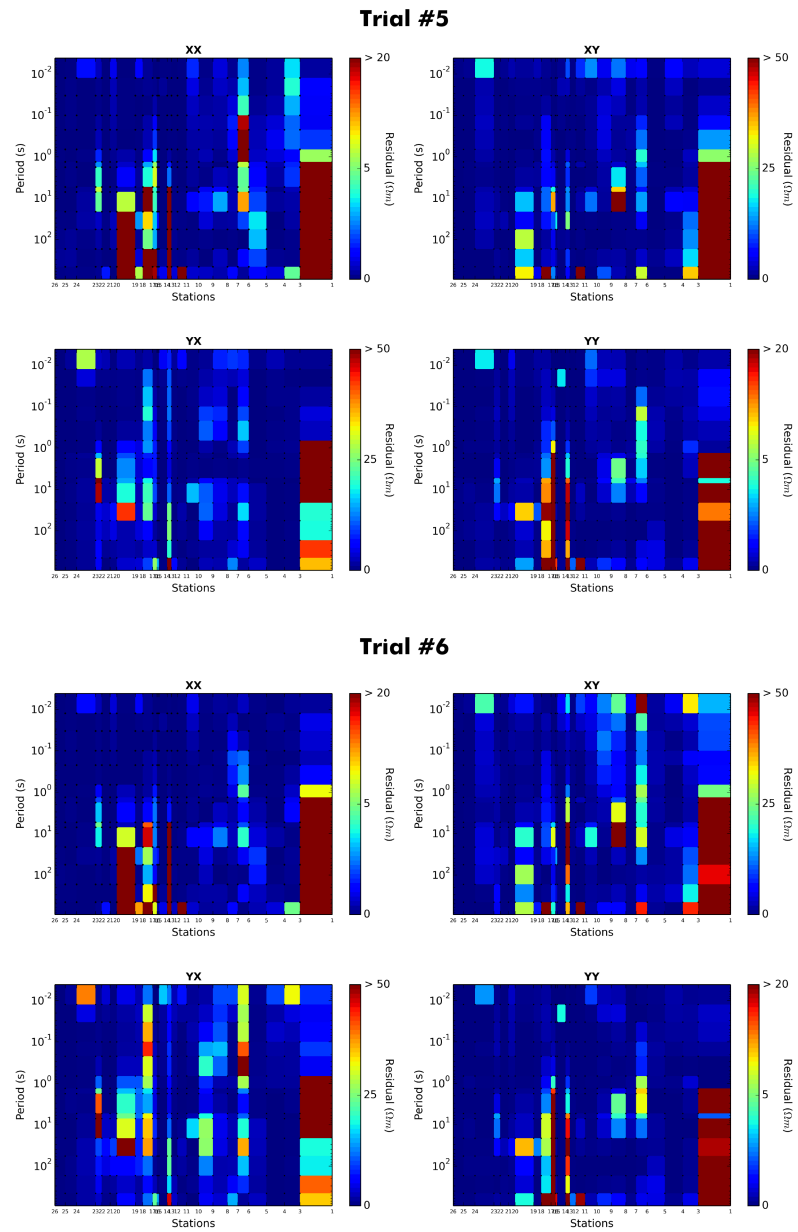


Figure 7.3. Apparent resistivity residuals of trials 1 and 2 for the four components of the impedances.

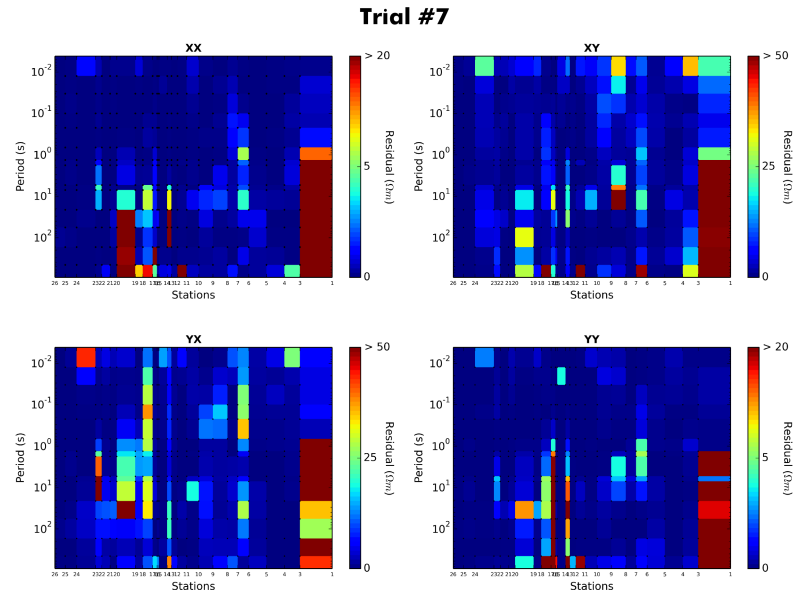


Figure 7.4. Apparent resistivity residuals of Trial 7 for the four components of the impedances.

APPENDIX B: FITTING CURVES OF FINAL REGIONAL MODEL

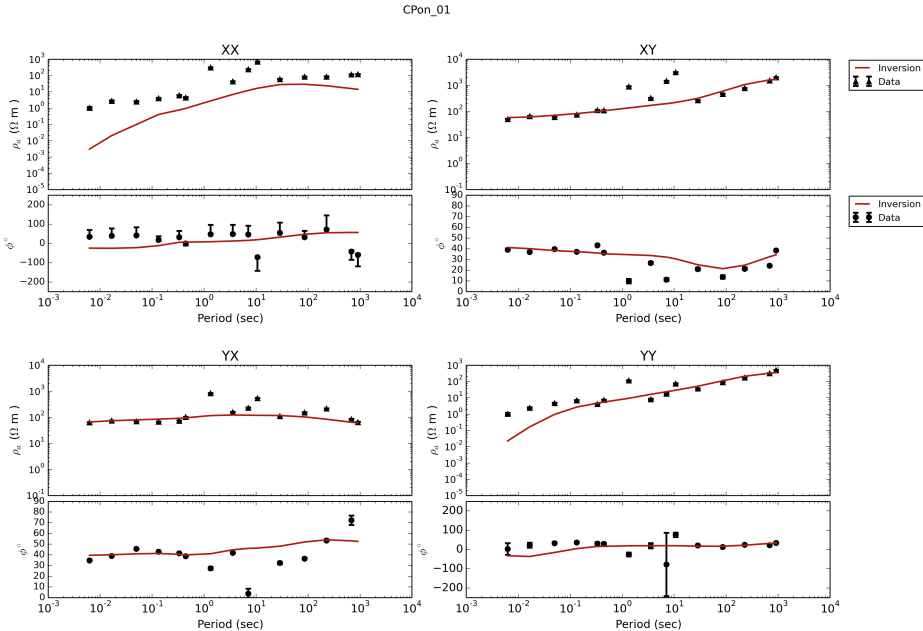


Figure 7.5. Fitting curves of station 1 for the final resistivity model.

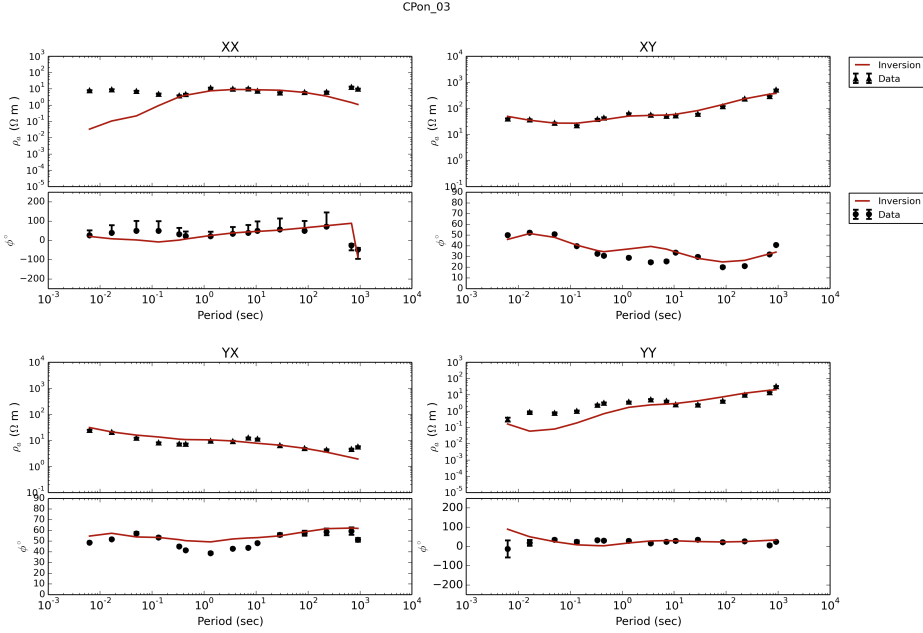


Figure 7.6. Fitting curves of station 3 for the final resistivity model.

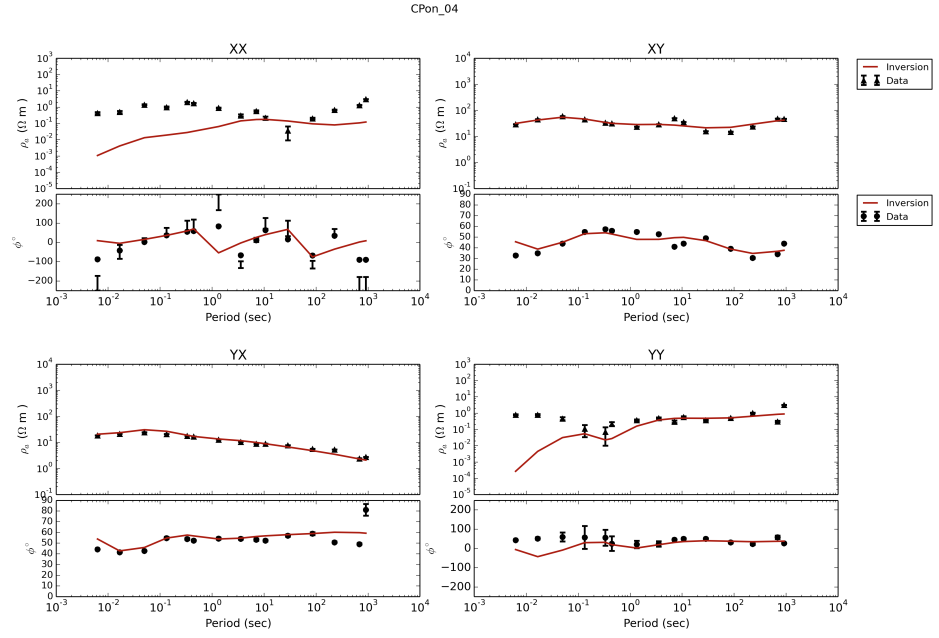


Figure 7.7. Fitting curves of station 4 for the final resistivity model.

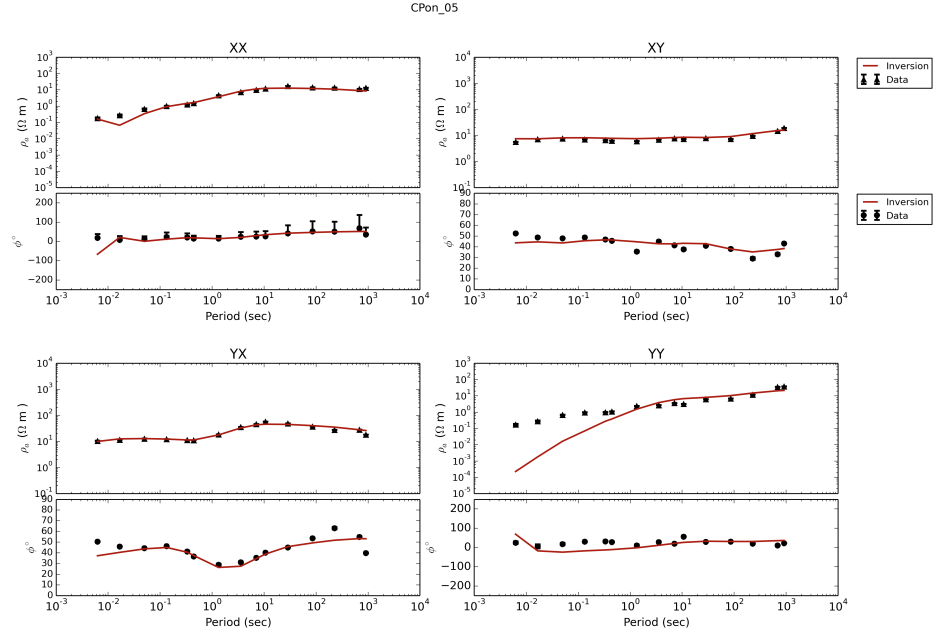


Figure 7.8. Fitting curves of station 5 for the final resistivity model.

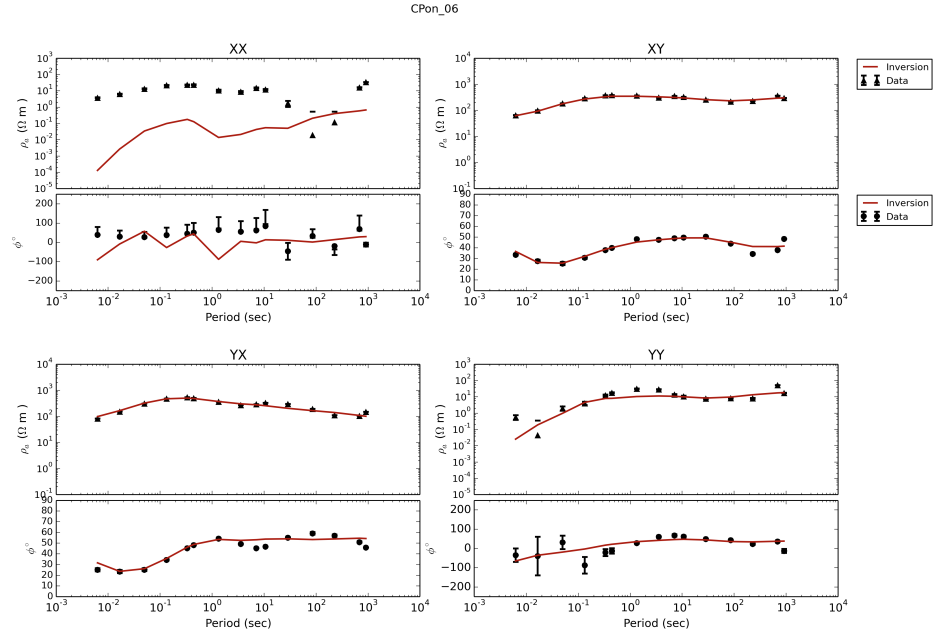


Figure 7.9. Fitting curves of station 6 for the final resistivity model.

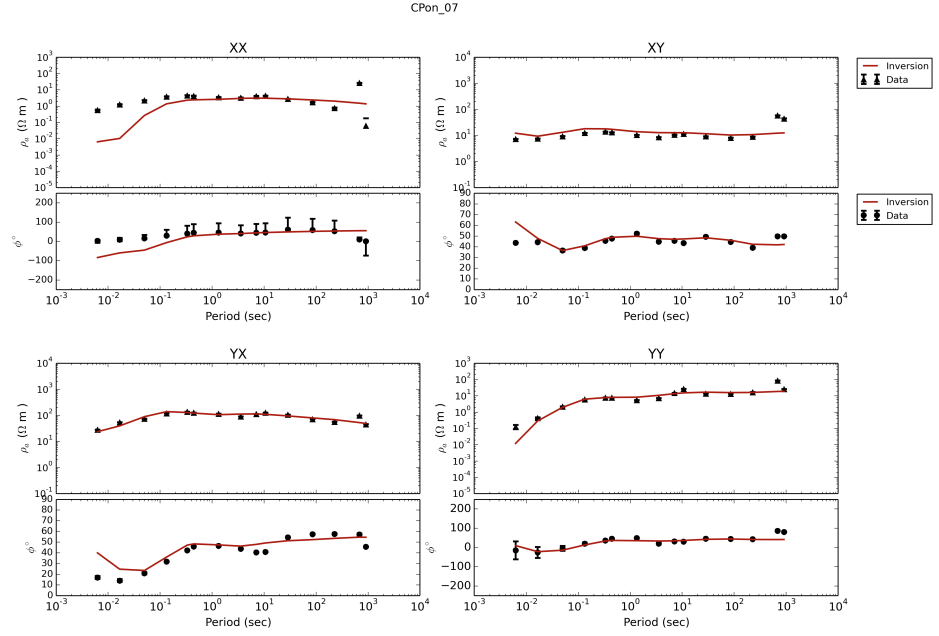


Figure 7.10. Fitting curves of station 7 for the final resistivity model.

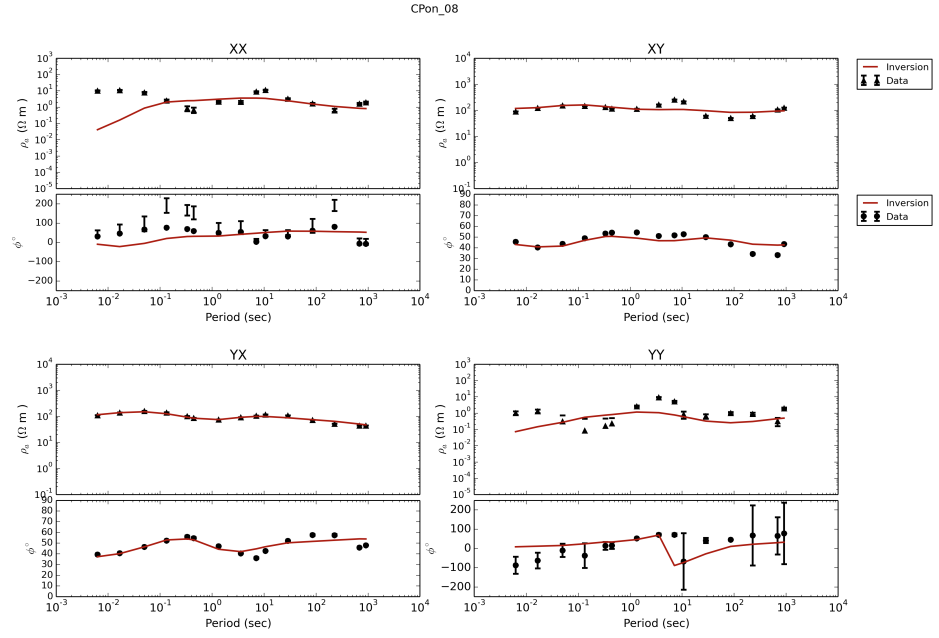


Figure 7.11. Fitting curves of station 8 for the final resistivity model.

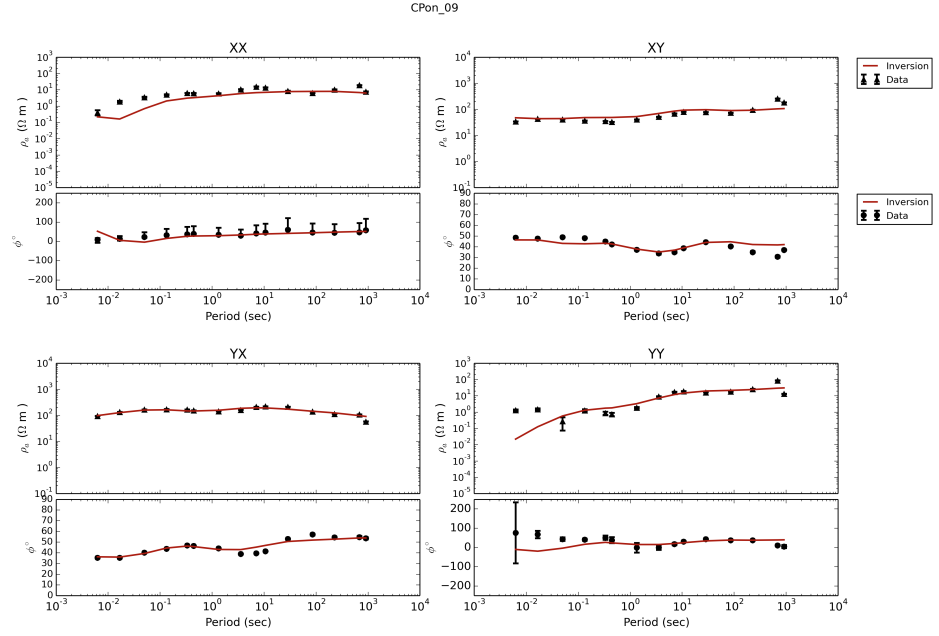


Figure 7.12. Fitting curves of station 9 for the final resistivity model.

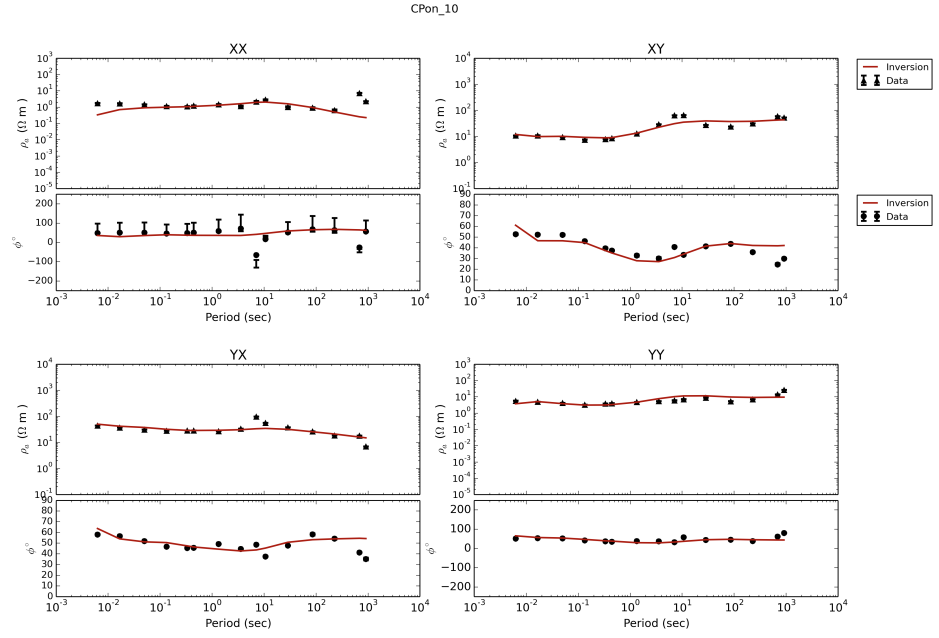


Figure 7.13. Fitting curves of station 10 for the final resistivity model.

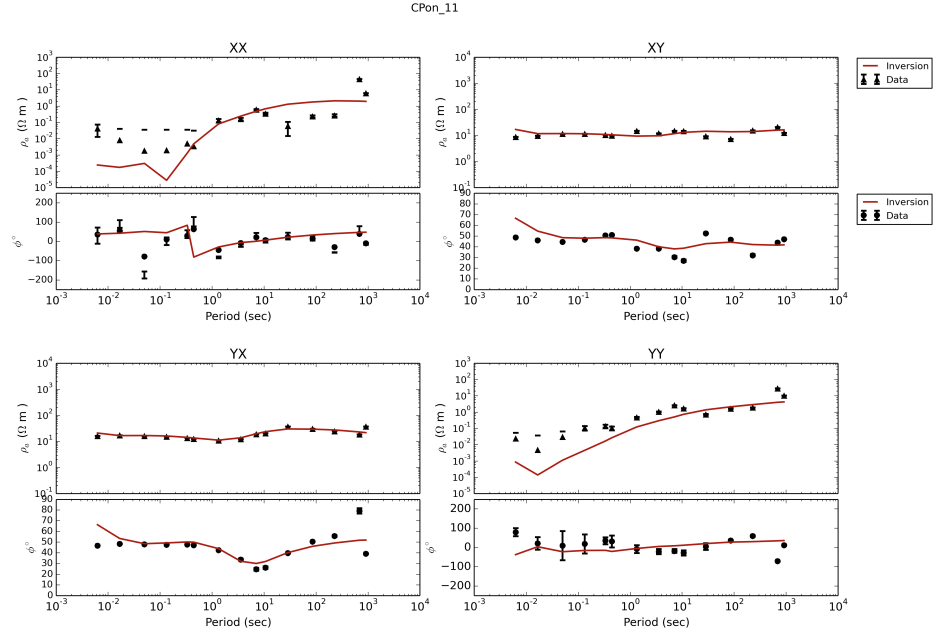


Figure 7.14. Fitting curves of station 11 for the final resistivity model.

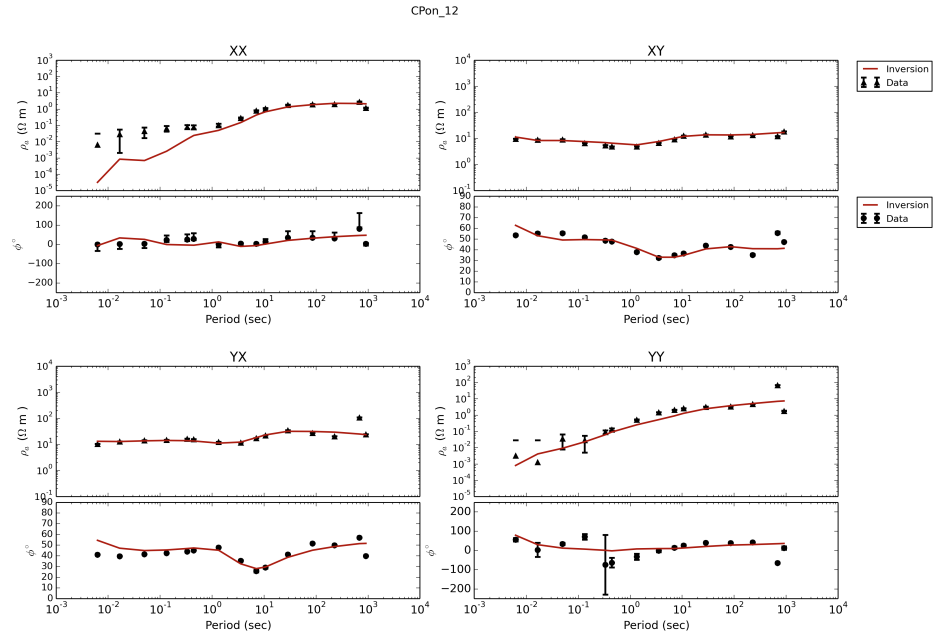


Figure 7.15. Fitting curves of station 12 for the final resistivity model.

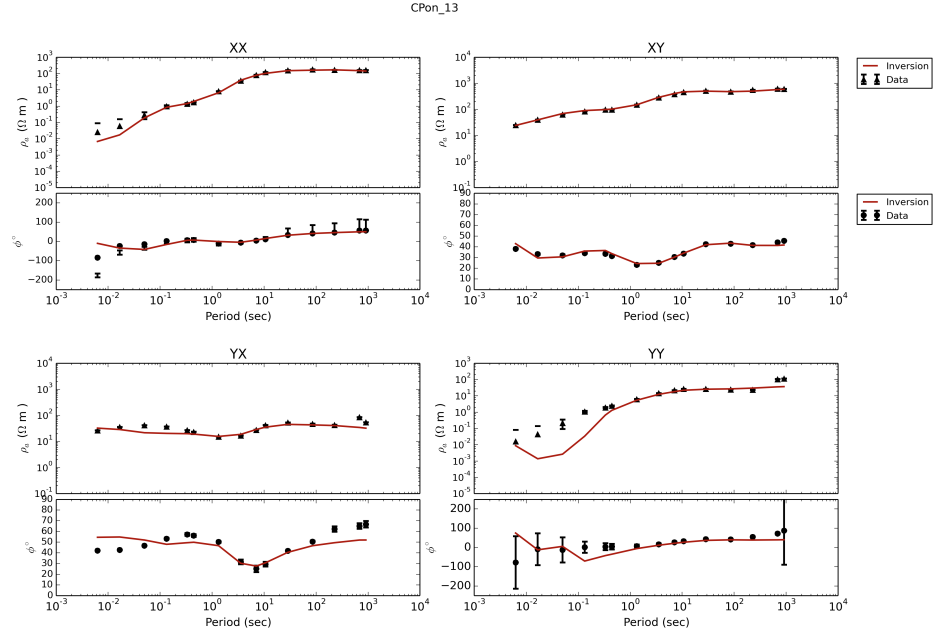


Figure 7.16. Fitting curves of station 13 for the final resistivity model.

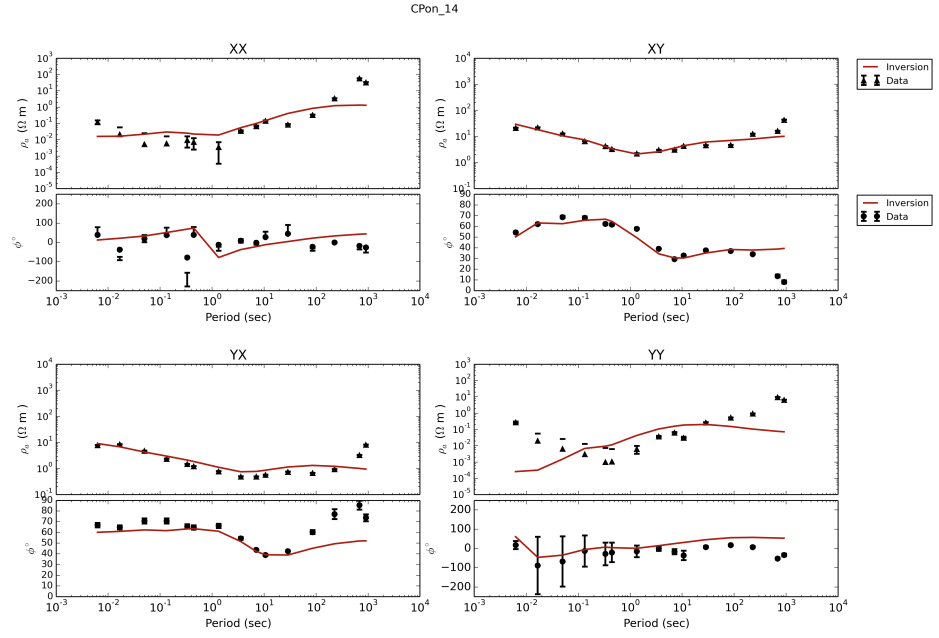


Figure 7.17. Fitting curves of station 14 for the final resistivity model.

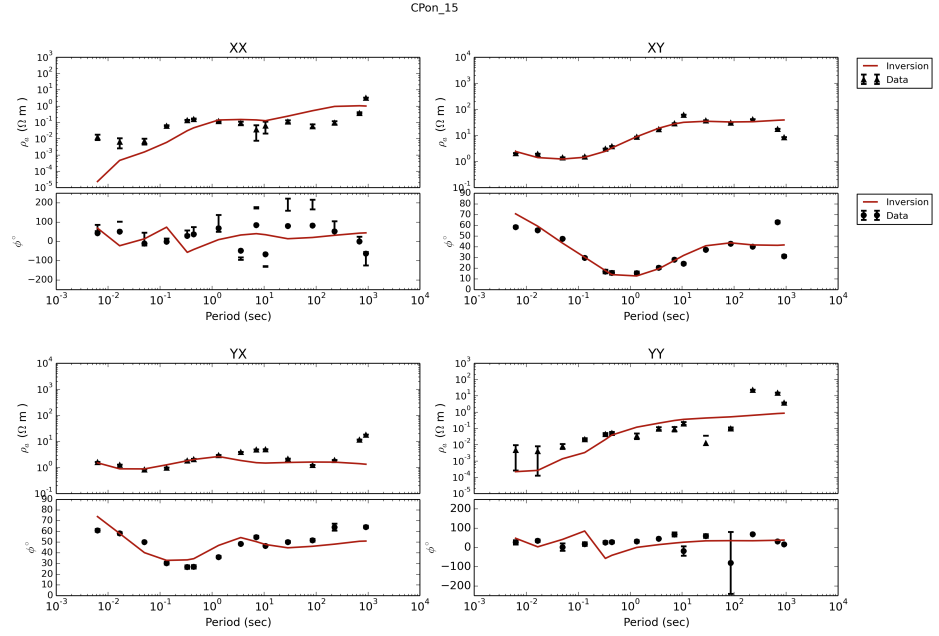


Figure 7.18. Fitting curves of station 15 for the final resistivity model.

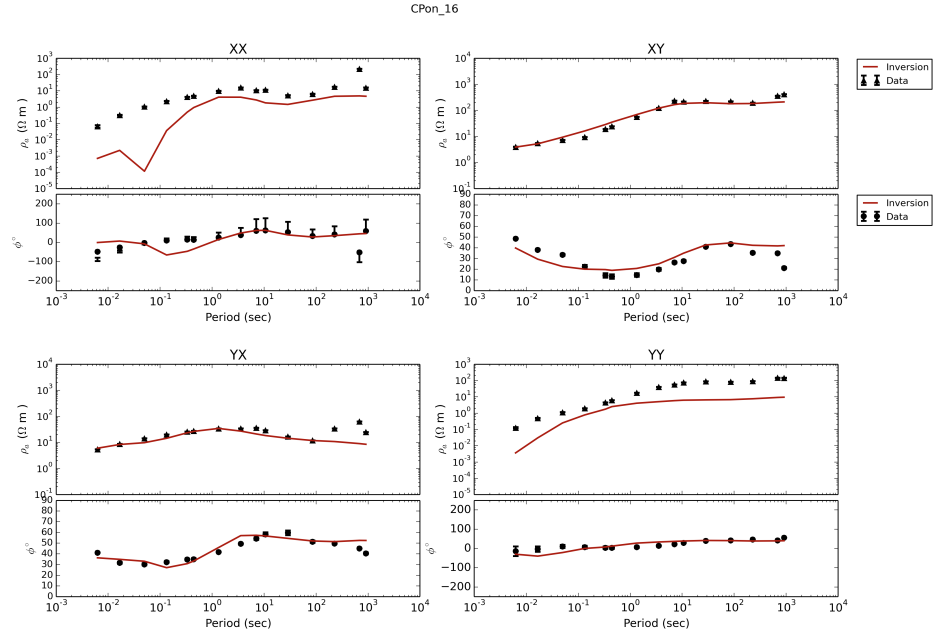


Figure 7.19. Fitting curves of station 16 for the final resistivity model.

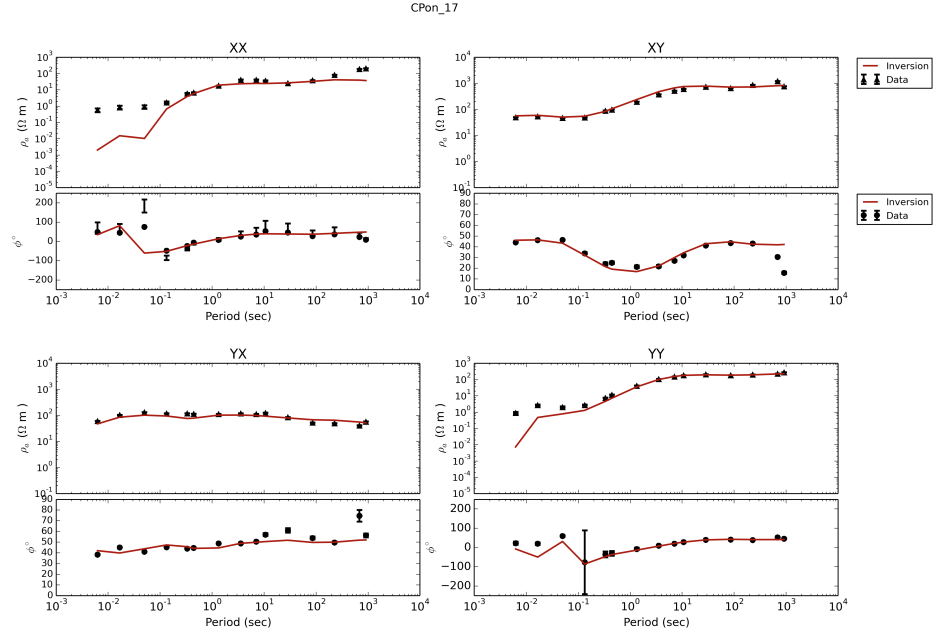


Figure 7.20. Fitting curves of station 17 for the final resistivity model.

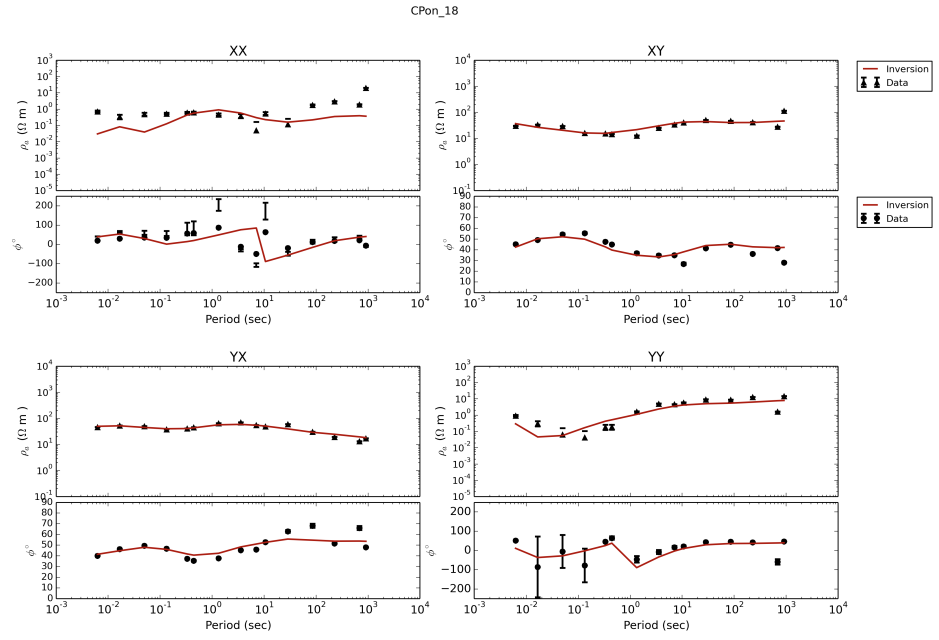


Figure 7.21. Fitting curves of station 18 for the final resistivity model.

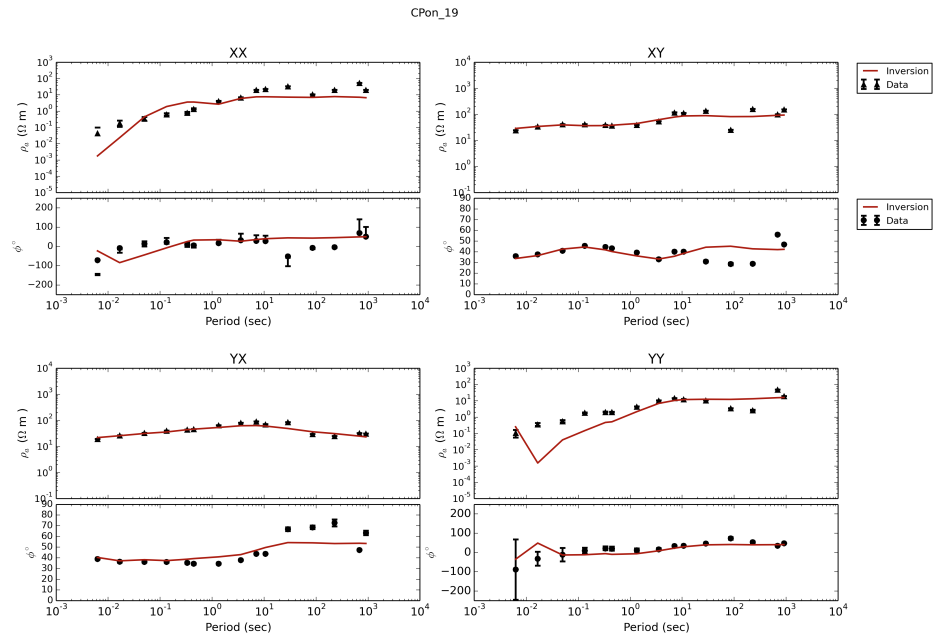


Figure 7.22. Fitting curves of station 19 for the final resistivity model.

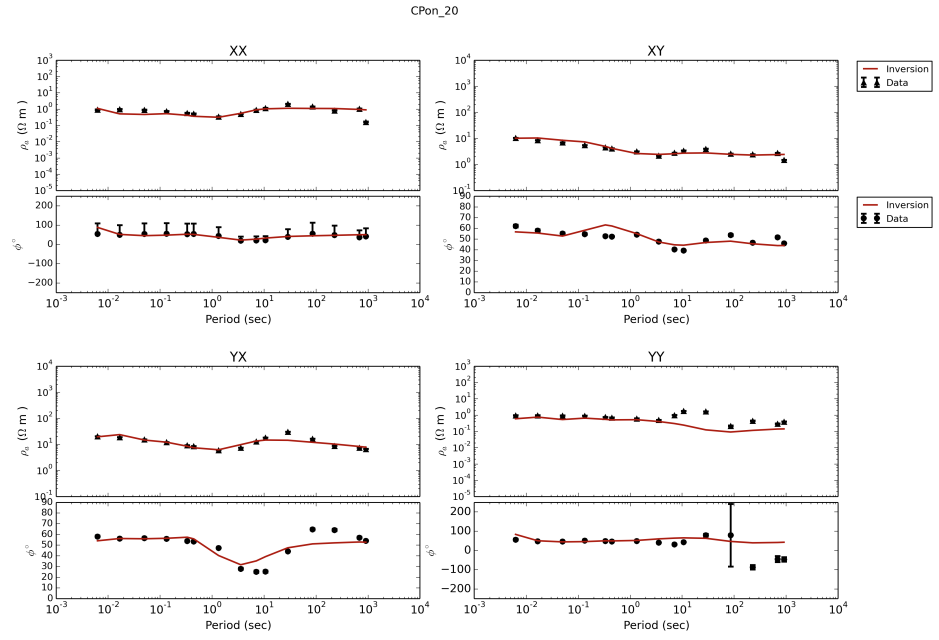


Figure 7.23. Fitting curves of station 20 for the final resistivity model.

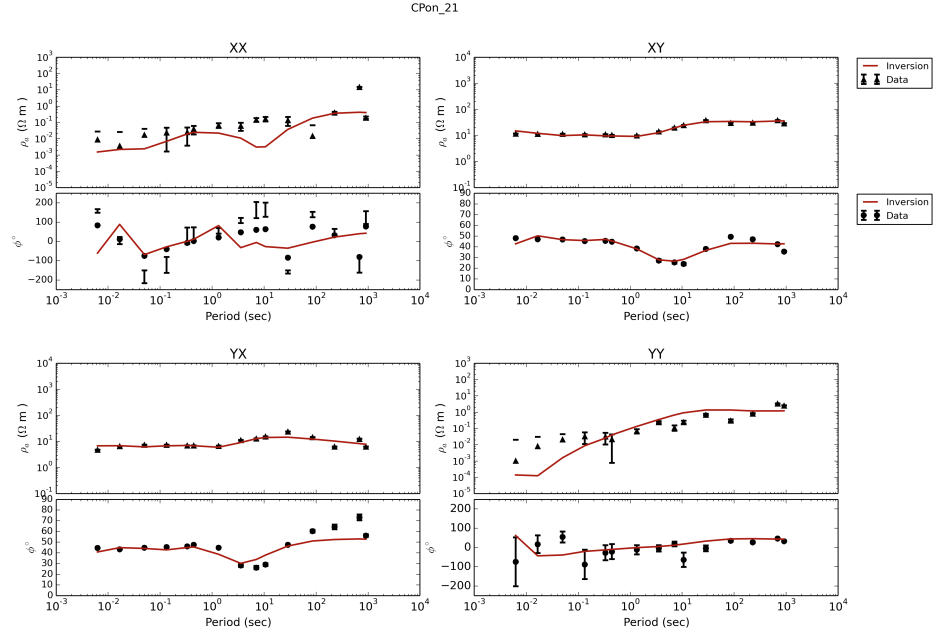


Figure 7.24. Fitting curves of station 21 for the final resistivity model.

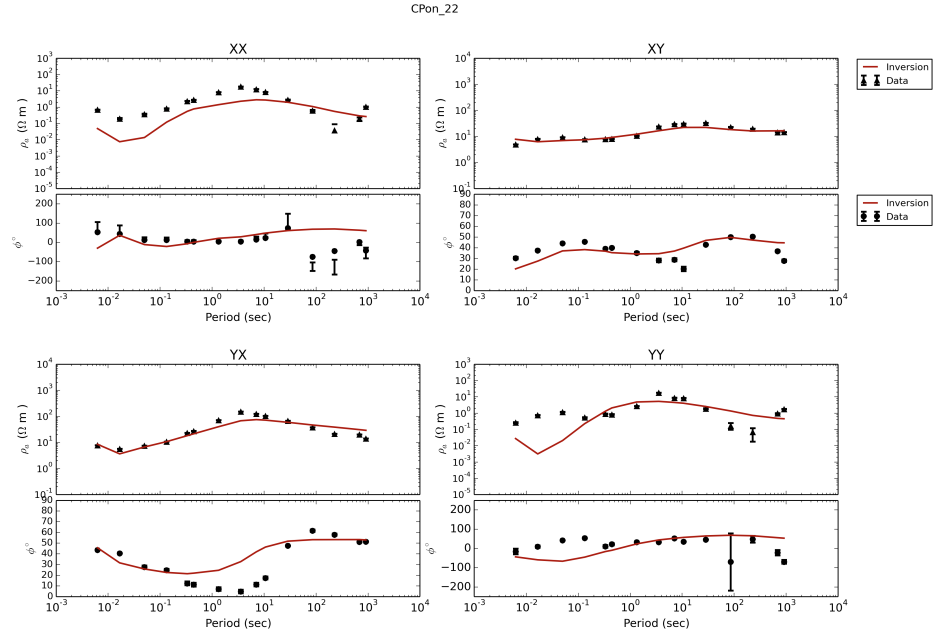


Figure 7.25. Fitting curves of station 22 for the final resistivity model.

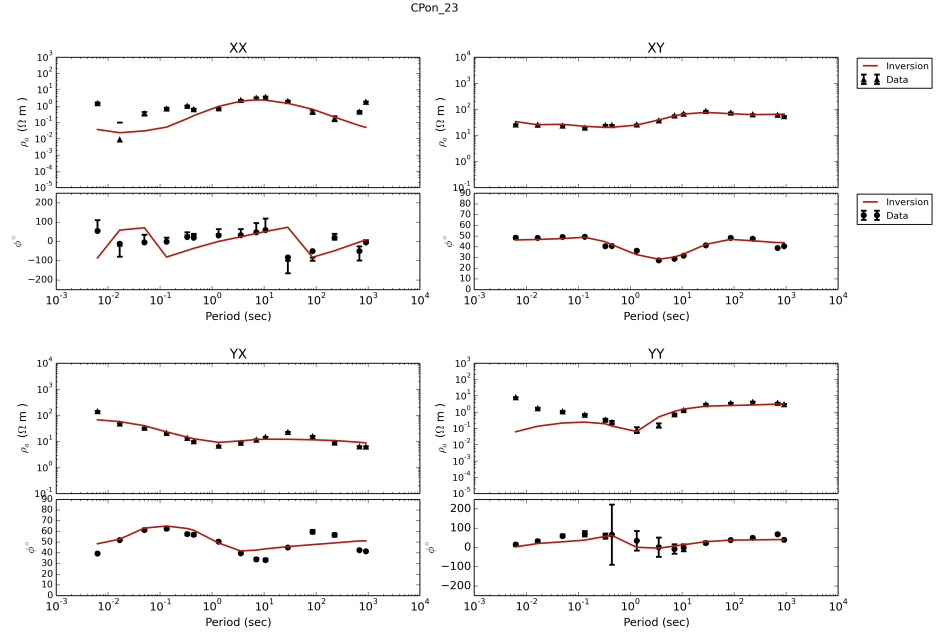


Figure 7.26. Fitting curves of station 23 for the final resistivity model.

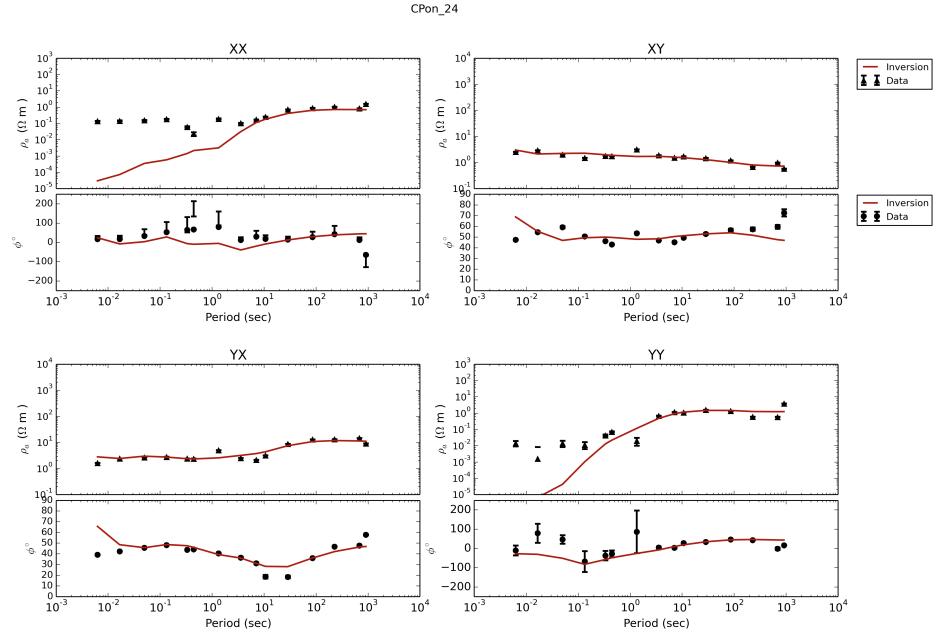


Figure 7.27. Fitting curves of station 24 for the final resistivity model.

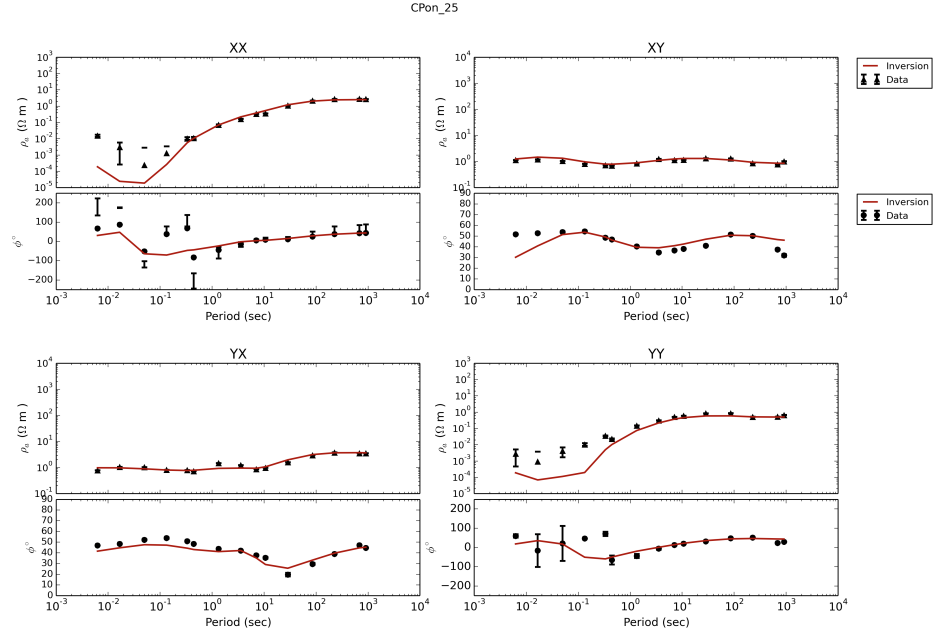


Figure 7.28. Fitting curves of station 25 for the final resistivity model.

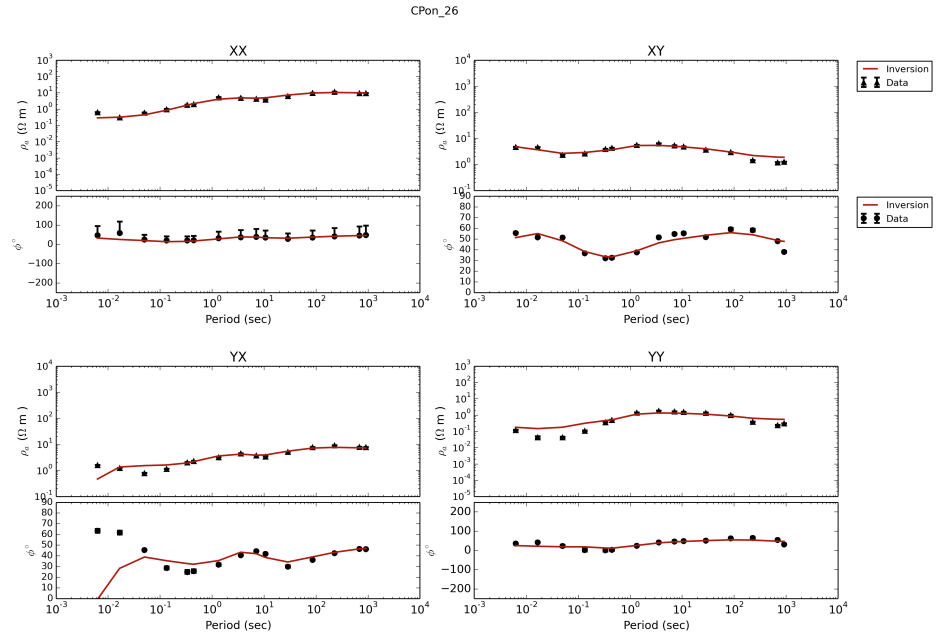


Figure 7.29. Fitting curves of station 26 for the final resistivity model.

APPENDIX C: FITTING CURVES OF LOCAL MODEL

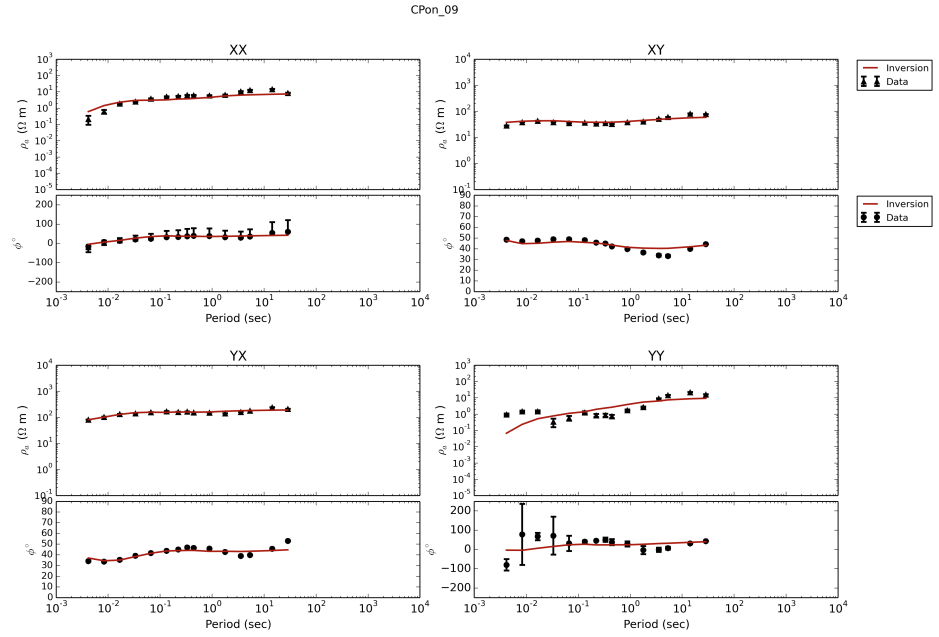


Figure 7.30. Fitting curves of station 9 for the NAF model.

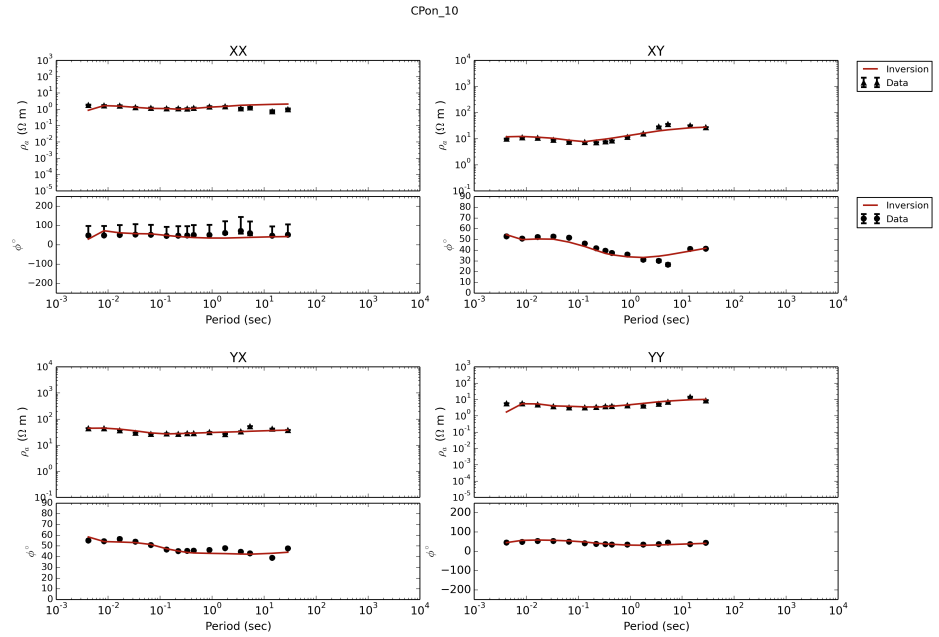


Figure 7.31. Fitting curves of station 10 for the NAF model.

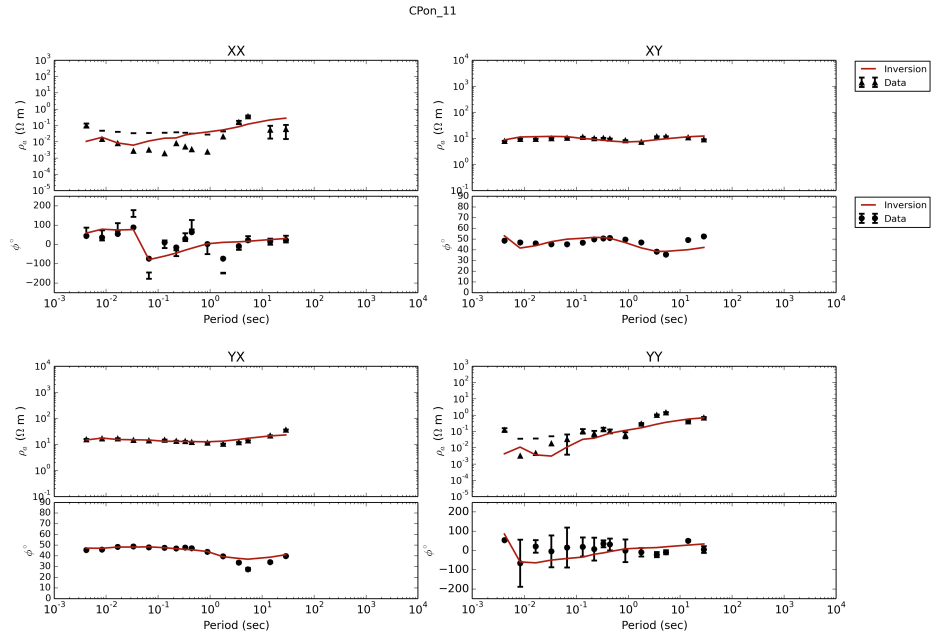


Figure 7.32. Fitting curves of station 11 for the NAF model.

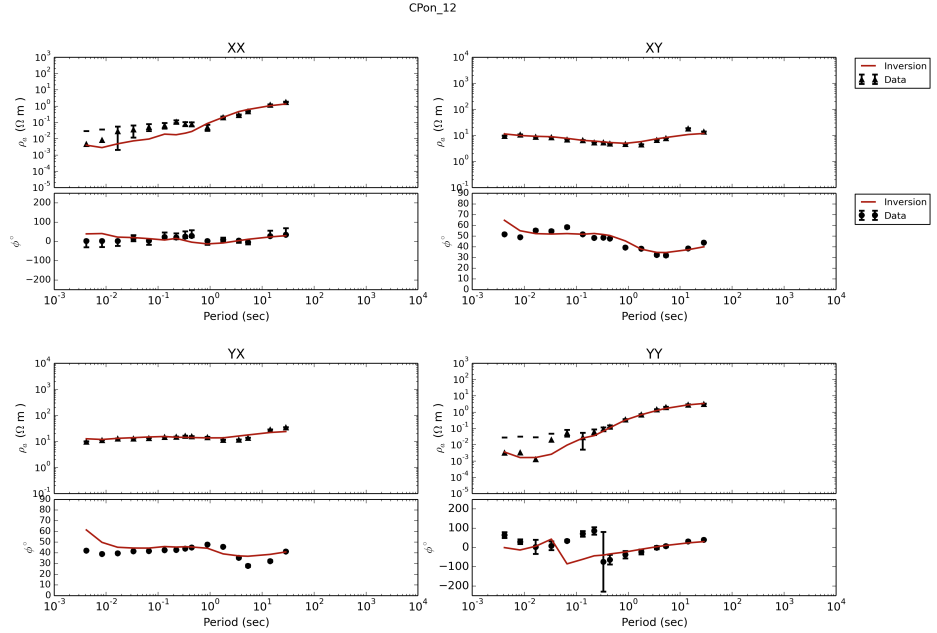


Figure 7.33. Fitting curves of station 12 for the NAF model.

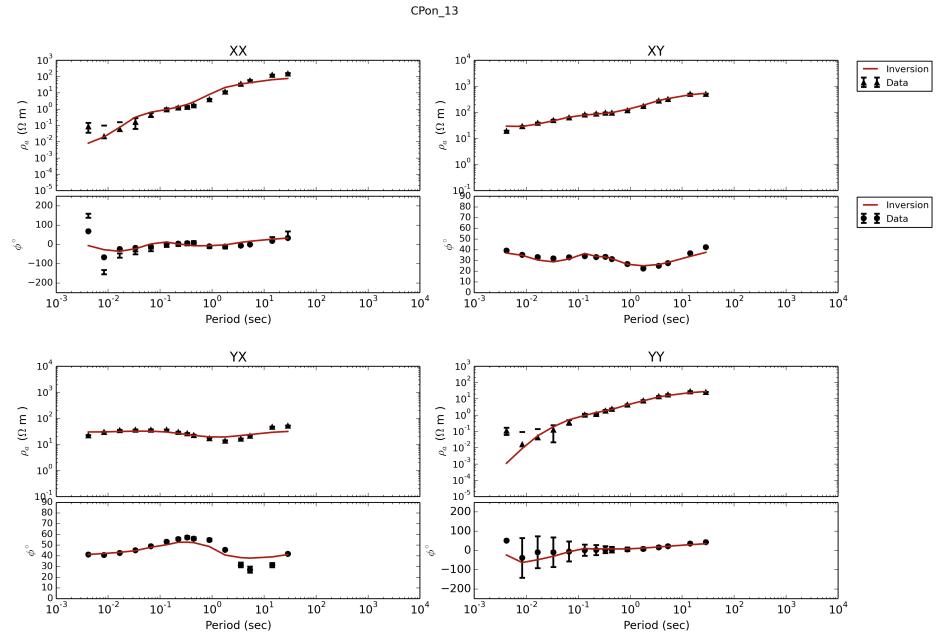


Figure 7.34. Fitting curves of station 13 for the NAF model.

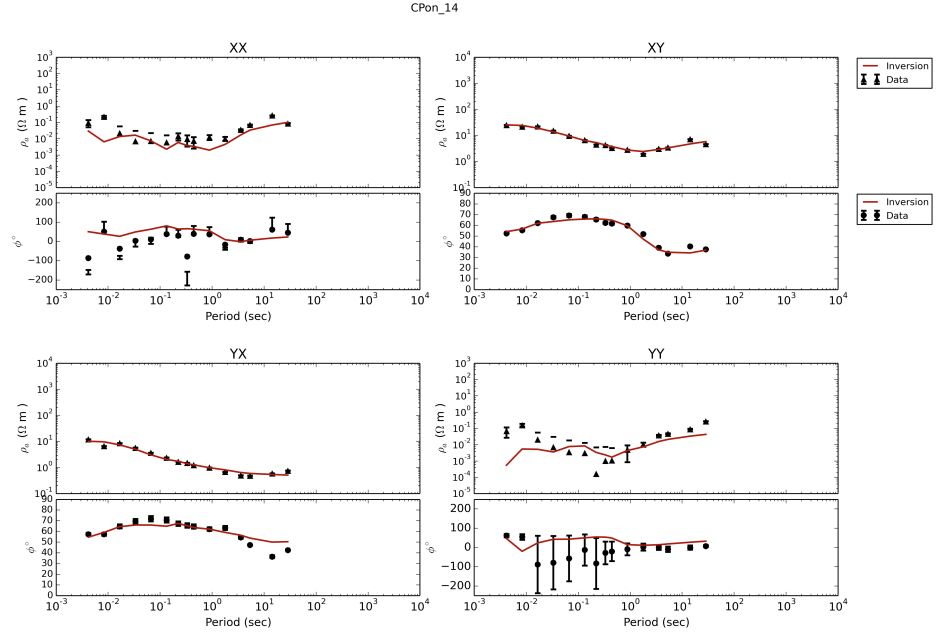


Figure 7.35. Fitting curves of station 14 for the NAF model.

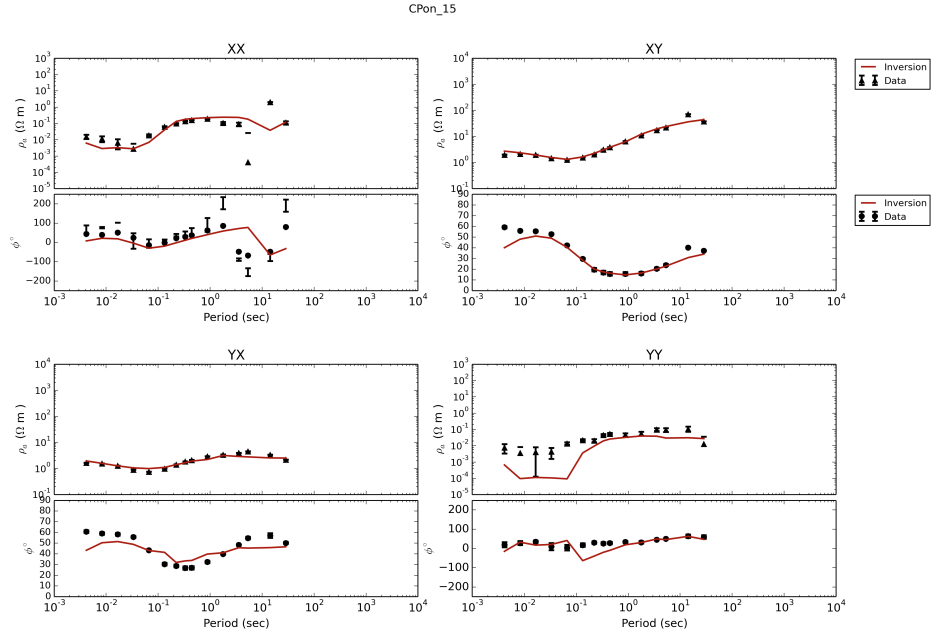


Figure 7.36. Fitting curves of station 15 for the NAF model.

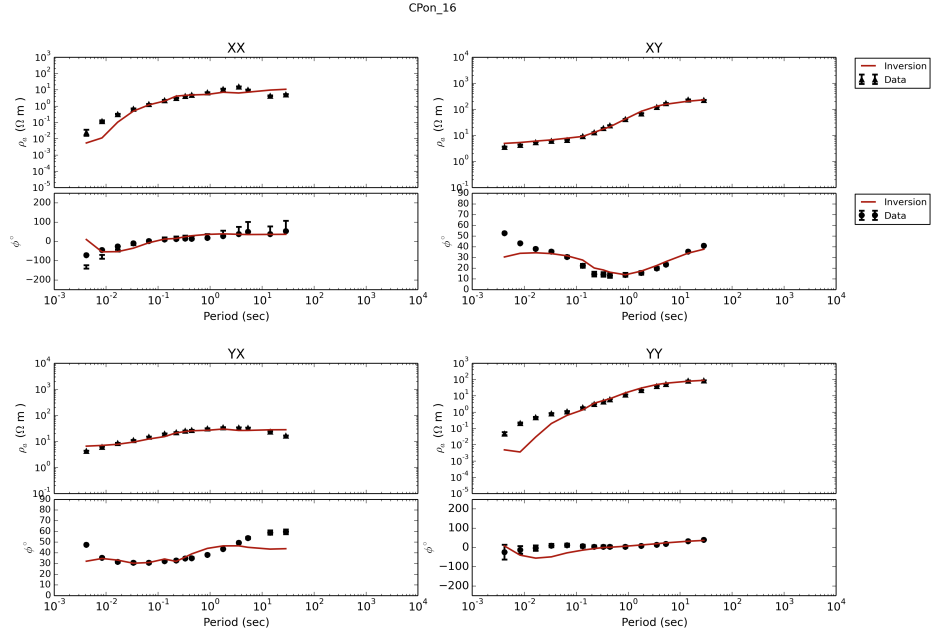


Figure 7.37. Fitting curves of station 16 for the NAF model.

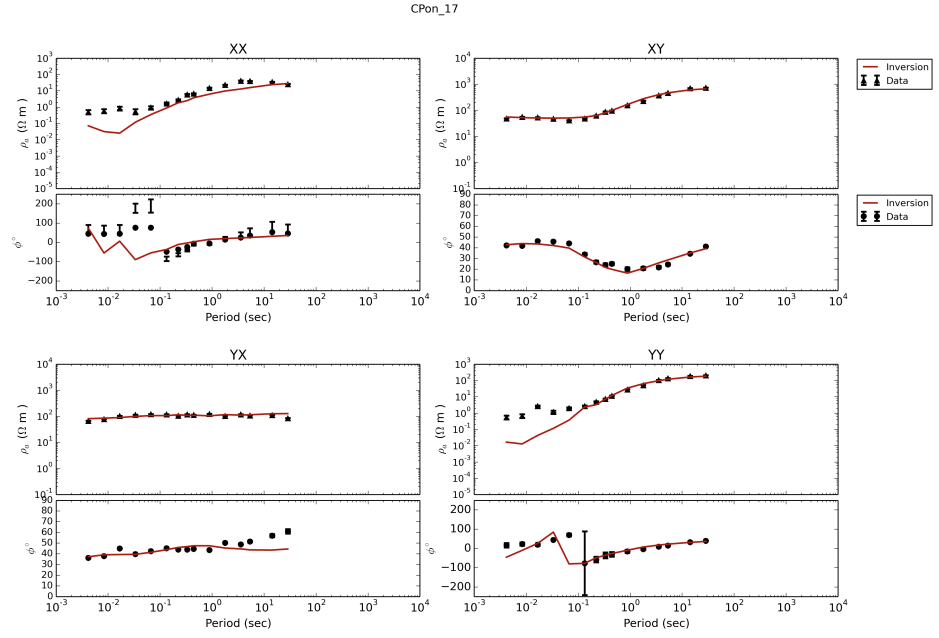


Figure 7.38. Fitting curves of station 17 for the NAF model.

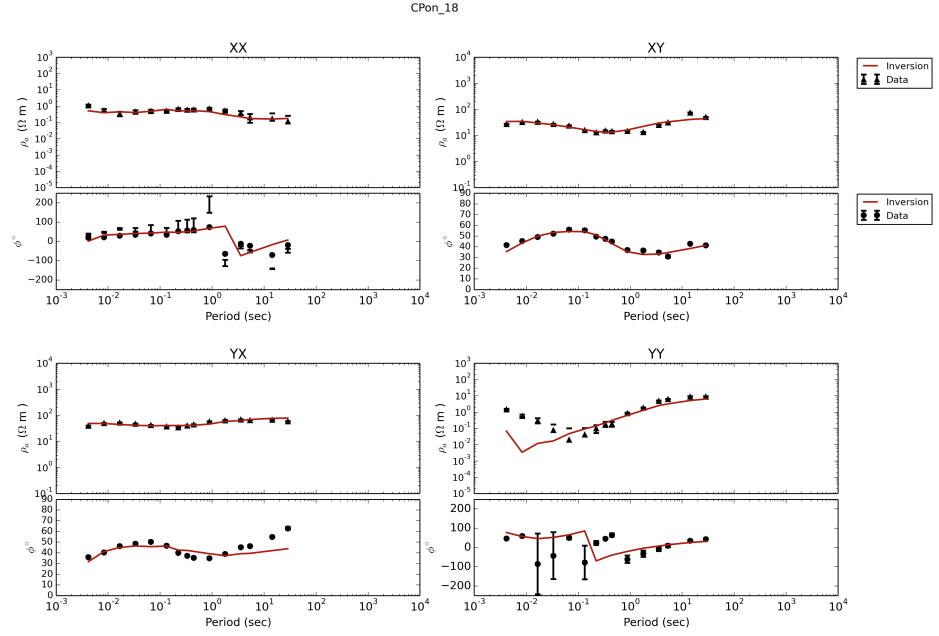


Figure 7.39. Fitting curves of station 18 for the NAF model.

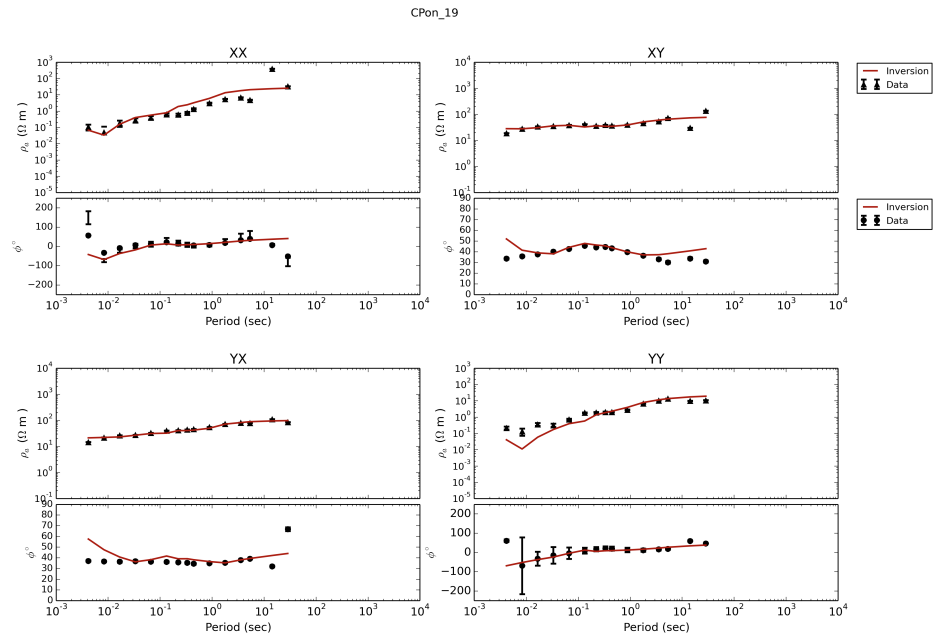


Figure 7.40. Fitting curves of station 19 for the NAF model.